ISSN: 3082-849X (Online)
Volume 1 · Issue 4
December 2025

Engineering Science in ADDITIVE MANUFACTURING

Engineering Science in Additive Manufacturing (ESAM) aims to collate the cutting-edge research and review articles in additive manufacturing that highlight the engineering science

ACCSCIENCE PUBLISHING

Engineering Science in Additive Manufacturing

Online ISSN: 3082-849X

Engineering Science in Additive Manufacturing (ESAM) aims to collate the cutting-edge research and review articles in additive manufacturing that highlight the engineering science. The journal covers all fundamentals of additive manufacturing, including its principles and applications. The journal publishes articles that acknowledge the significant development in the field and its disruptive nature in the industry. ESAM provides a platform for publishing articles that advance the in-depth understanding of additive manufacturing. The journal also welcomes papers that employ theories, numerical methods and/or simulations that demonstrate relevance to the additive manufacturing community.

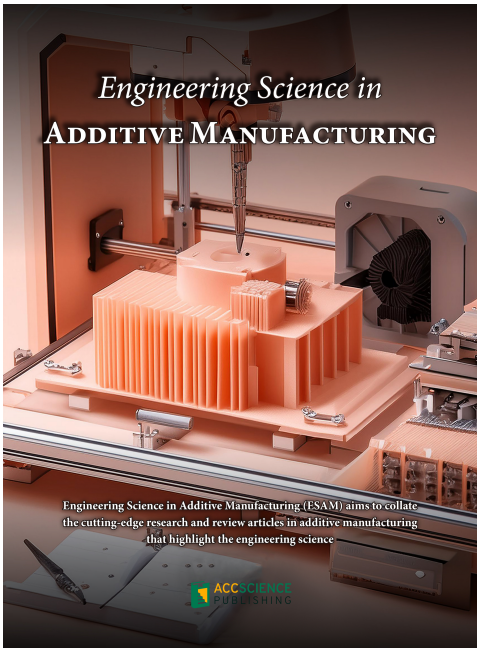

About the Publisher

AccScience Publishing is a publishing company based in Singapore. We publish a range of high-quality, open-access, peer-reviewed journals and books from a broad spectrum of disciplines.

Contact Us

Managing Editor
esam.office@accscience.sg

AccScience Publishing
9 Raffles Place, Republic Plaza 1 #06-00 Singapore 048619.

Volume 1 • Issue 4 • December 2025
ISSN 3082-849X (online)

ENGINEERING SCIENCE IN ADDITIVE MANUFACTURING

Editor-in-Chief
Swee Leong Sing
National University of Singapore, Singapore

ACCSCIENCE PUBLISHING
Access Science Without Barriers

ENGINEERING SCIENCE IN ADDITIVE MANUFACTURING

ISSN: 3082-849X (online)

Editorial and Production Credits

Publisher: AccScience Publishing
Managing Editor: Shirley Lu
Production Editor: Sharmila Velapasamy
Article Layout and Typeset: Sinjore Technologies (India)

For all advertising queries, contact esam.office@accscience.sg.

Supplementary file

Supplementary files of articles can be obtained at https://accscience.com/journal/ESAM/1/4.

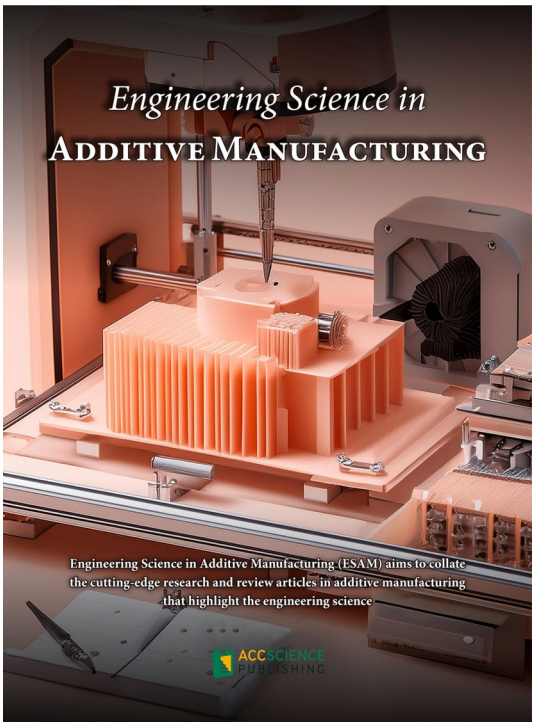

Disclaimer

AccScience Publishing is not liable to the statements, perspectives, and opinions contained in the publications. The appearance of advertisements in the journal shall not be construed as a warranty, endorsement, or approval of the products or services advertised and/or the safety thereof. AccScience Publishing disclaims responsibility for any injury to persons or property resulting from any ideas or products referred to in the publications or advertisements. AccScience Publishing remains neutral with regard to jurisdictional claims in published maps and institutional affiliations.

Engineering Science in Additive Manufacturing

Editorial Board

ACCSCIENCE PUBLISHING

Volume 1 | Issue 4 | December 2025

Engineering Science in Additive Manufacturing

https://accscience.com/journal/ESAM

CONTENTS

ACCSCIENCE PUBLISHING

Engineering Science in Additive Manufacturing

REVIEW ARTICLE

Guidelines for the use and reporting of experimental statistics in additive manufacturing: An assessment of current practices

Colin M. Lynch[1]*, Ryan B. Wicker[2,3], Jorge Mireles[3], and Rene Villalobos[1]

[1]Terra Integrated Solutions, Mesa, Arizona, United States of America

[2]W.M. Keck Center for 3D Innovation, The University of Texas at El Paso, El Paso, Texas, United States of America

[3]Department of Mechanical and Aerospace Engineering, The University of Texas at El Paso, El Paso, Texas, United States of America

Abstract

Additive manufacturing (AM) creates three-dimensional objects using various approaches, typically layer-by-layer. One emerging method is laser-based powder bed fusion of metals (PBF-LB/M), which uses high-energy lasers to melt metallic powder into shape. AM processes are influenced by many factors, yet there is no standardized framework for quantifying their effects on final products. This guide introduces key principles of experimental design and statistics, outlining a roadmap for conducting rigorous experiments. We review the literature on AM generally and PBF-LB/M specifically to assess how well current practices align with standardized methodologies. In addition, we compare the evolution of experimental techniques in PBF-LB/M to those in a more regulated industry to explore potential cross-pollination. Our analysis reveals that most studies do not adhere to best practices in experimental design and statistical analysis. For example, randomization of run order is rarely mentioned, and statistical model assumptions are often unchecked. Even in tightly regulated fields, experimental designs and statistical methods remain basic and lack sophistication. To improve research quality, we provide recommendations for establishing standardized experimental and reporting practices in AM.

Keywords: Design of experiments; Response surface methodology; Additive manufacturing and 3D printing; Laser-based powder bed fusion of metals; Experimental statistics

***Corresponding author:**
Colin M. Lynch
(cmlynch2@asu.edu)

Citation: Lynch CM, Wicker RB, Mireles J, Villalobos R. Guidelines for the use and reporting of experimental statistics in additive manufacturing: An assessment of current practices. *Eng Sci Add Manuf*. 2025;1(4):025340021. doi: 10.36922/ESAM025340021

Received: August 19, 2025

1st revised: September 18, 2025

2nd revised: September 22, 2025

Accepted: September 24, 2025

Published online: November 14, 2025

1. Introduction

Over the past few decades, additive manufacturing (AM) has undergone tremendous evolution, transitioning from research laboratories to widespread industrial adoption.[1] This evolution depends strongly on the vast experimental effort to discover new technologies, materials, and processes.[2] Despite these advancements, AM can still be considered to be in its infancy, as further work needs to be done to ensure that manufactured parts have performance characteristics equivalent to—or better than—parts manufactured

with traditional methods, particularly in the fabrication of high-value parts with metal alloys using laser-based powder bed fusion of metals (PBF-LB/M). Some of these characteristics include strength, reliability, geometric tolerances, cosmetic aspects, and cost.[3] Experiments will play a fundamental role in the achievement of these goals. Thus, it is important that the right tools and procedures are used to properly design these experiments, analyze their results, and report critical findings.

To begin, we provide a brief overview of AM generally and PBF-LB/M specifically. AM is defined as a process of joining materials to make objects from three-dimensional (3D) model data, usually in a constructive manner, i.e., layer upon layer, as opposed to subtractive manufacturing methodologies.[4] The goal of AM is to quickly and efficiently fabricate complicated objects that may be inconvenient to produce with traditional machining techniques.[5] While the specifics of every AM technique differ, the complexity of potential builds enforces a sophisticated approach to manufacturing 3D objects. For instance, one form of PBF requires raking a metallic powder onto a build plate, using a laser beam as an energy source to melt the powder into a desired shape, lowering the build plate, and then repeating the process until a 3D structure is formed,[6] referred to as PBF-LB/M.[3] However, the field also employs dozens of other AM techniques as well, utilizing a wide diversity of materials such as polymers, metals, and ceramics[7]; the American Society for Testing and Materials (ASTM) has classified the myriad AM technologies into seven overarching process categories.[8] AM is used within fields such as aerospace engineering,[9] construction,[10] robotics,[11] and medicine.[12] The end application of the fabricated objects can also be very different, from rough plastic prototyping to operations that require higher performance and reliability.[13,14]

Regardless of the end goal of the process and the type of AM used, the complexity of manufacturing allows for error at many different processing steps.[15] In addition, each manufacturing process is highly sensitive to the parameter settings of the machine, causing uncertainty in the quality of the final products.[16] In the case of PBF-LB/M, these factors include the type of feedstock used, the type of commercial AM system, laser power, scan speed, and more than a hundred additional factors.[17,18] It is difficult to know *a priori* which factors will have an effect and what that effect will be, especially within PBF-LB/M where the relevant factors are very often not known and are not controlled. Simulating the process with tools such as finite element modeling can help in the absence of real data,[19] but accurate models can be challenging to design, computationally expensive, part-specific, and require validation experiments to ensure the models represent the physical reality with appropriate fidelity. Therefore, a rigorous statistical analysis on data collected from a well-designed experiment is the best way to find out what parameters affect the AM process, set these parameters to obtain the best output sought, and determine if the resulting process can meet the required specifications.

Thus, given the pervasiveness of AM as well as the uncertainty about the quality of the fabricated objects, experiments and statistics should be used in tandem to assess potential sources of variability and to ensure consistency of the final product. This issue is particularly salient within PBF-LB/M, which is considered one of the most promising processes for fabricating critical structural components in high-end applications such as aerospace and medicine.[20] In this paper, we assess the current state-of-the-art practices of experimental statistics, focusing on the design of experiments (DOE[21-23]) and response surface methodologies (RSM[24,25]). To do this, we evaluate the frequency at which statistical techniques and different experimental design types are used within AM generally and PBF-LB/M specifically, and evaluate how these practices have been changing over time. We also compare the evolution of the use of these methods within PBF-LB/M and a highly regulated medical field (orthopedics), and summarize the use of these methods in the best of the sampled papers. We then compare current practices to ideal practices to provide recommendations on how the field can improve experimentally, offering a roadmap that engineers can follow to maximize the efficacy of their experiments.

2. State-of-the-art practices for statistics and DOE

Although AM has been around for the last 30+ years, it has mostly remained in the areas of prototyping and, in a few cases, in small production of parts. However, it is widely believed that the field should aim to develop systems and processes that result in the manufacturing of parts that are ready for use in industrial applications. A primary challenge in AM, particularly for metal components, is ensuring that printed parts achieve reliability comparable to those manufactured through conventional methods. Demonstrating this equivalence necessitates rigorous testing, thorough experimentation, and robust methods for assessing quality and consistency. Experimental statistics offers valuable tools to address these needs by quantifying variability, optimizing process parameters, and validating material properties and mechanical performance. Moreover, statistical methods can accelerate the development and certification stages by efficiently

identifying key factors influencing product reliability and enabling informed decision-making based on data-driven insights. This paper aims to highlight essential statistical techniques beneficial to the AM community, facilitating the adoption of best practices and improving confidence in AM-produced parts (for detailed discussions of specific techniques).[26]

Statistics is a larger field than can possibly be covered here, but this broad overview highlights some of the minimum standards that should be applied to any experimental field. In this section, we introduce various experimental designs which can be used in different contexts. We then present some of the good statistical practices that, in our opinion, are most relevant in AM. The set of basic designs we will cover are presented in Table 1, which includes a brief description of each design, the conditions necessary for their proper implementation (whether or not a power analysis is needed to determine sample size, whether randomization is necessary, whether the underlying distribution needs to be checked, and whether an experimental design matrix needs to be evaluated), and the section of the companion to this manuscript[26] in which they are discussed more thoroughly. Distribution checks are necessary to ensure that the data follow the assumptions of the model (i.e., analysis of variance [ANOVA] assumes a normal distribution). These checks can be done using different methodologies, but the most common is to check the residuals of a fitted model, where residuals are the difference between the model prediction of a data point and its true value. These tables and companion manuscript are the result of an extensive literature search of statistical manuscripts and were produced in conversations with different AM experts. The designs are presented from the simplest to the most complex. Our underlying expectation is that as the statistical sophistication of AM advances, more complex designs will be used.

While there is no unique recipe for conducting experimentation, the steps depicted in Figure 1 provide a good blueprint for the proper application of experimental statistics, regardless of the chosen experimental design. Most steps of this figure require further comment, and reference[26] should be consulted for further discussions of these topics. It should be noted that there are many other approaches, and other statisticians may change the order of these steps or include other steps. In general, the steps consist of the following: (1) Defining the problem, the population, and/or response variable of interest, and state hypotheses at the onset to avoid introducing bias to the model selection process. (2) Defining a statistical model (or set of models) based on the stated hypotheses. (3) Conducting pre-experimental procedures to ensure experimental efficiency and trustworthiness of results. (4) Designing a sampling strategy. Determine the number of samples needed, what types of measurements need to be made, and how bias can be avoided by performing appropriate sampling. (5)

Table 1. Overview of experimental techniques, associated statistical tests, and minimum reporting requirements

Technique	Statistical test	Minimum conditions				Section number in ref. [26a]
		Sample size determination	Random-ization	Distribution check	Design matrix	
Simple hypothesis testing	*t*-test	✓	✓	✓		2.3, 3.2
One-way design	*F*-test	✓	✓	✓		2.4, 3.3
One-way design with blocking	*F*-test	✓	✓	✓		2.5
Split-plot one-way design	*F*-test	✓	✓	✓		2.6
One-way nested design	*F*-test	✓	✓	✓		2.7
Full factorial	*F*-test combined with a first-order regression model		✓	✓	✓	2.8
Fractional factorial	*F*-test combined with a first-order regression model		✓	✓	✓	2.9
Response surface methodology (RSM)	*F*-test combined with a second-order regression model		✓	✓	✓	2.10
Sequential experiments	*F*-test combined with the first- and second-order regression model		✓	✓	✓	2.11

Notes: [a]Section number in reference[26] which discusses each technique.

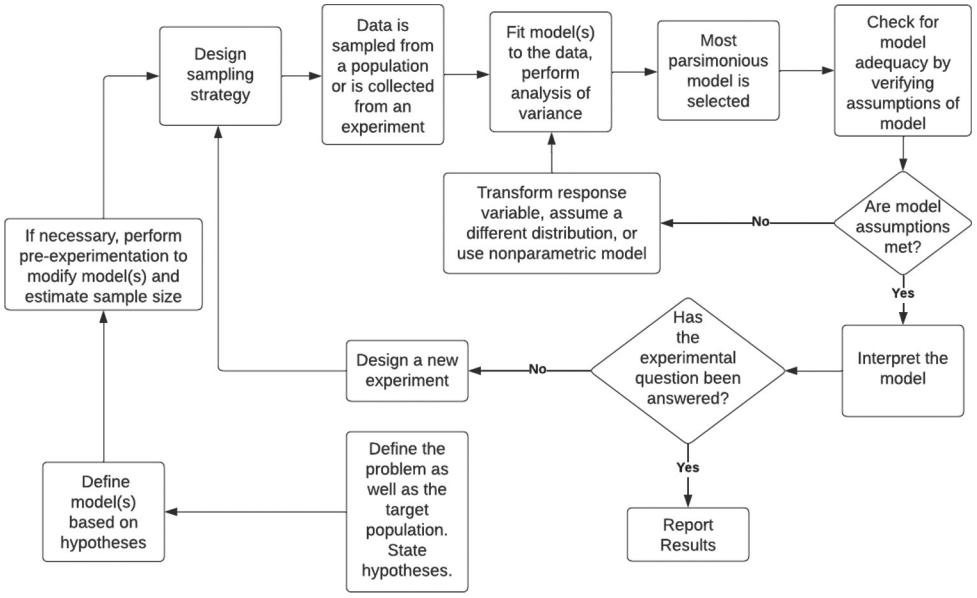

Figure 1. Flow diagram of experimentation and data analysis. Image created by the authors.

Sampling data from a targeted established population or from an experiment. (6) Fitting the data to the model so that its parameters allow the predictions of the model to match as closely as possible to the real data. (7) Checking the set of candidate models against one another to see which one provides the most explanatory power with the fewest assumptions. (8) Checking the most parsimonious model for adequacy. Assumptions of the model, such as the normal distribution of residuals, may or may not be met. (9) Transforming the variable if necessary, using an alternative method to fit the data, or assuming a different class of model until the final model(s) fit the data well. (10) Interpreting the model. The significance of different factors is checked by calculating the probability of observing these data given that there is no true effect of that factor. (11) Reporting the results, if the experimental question has been answered; otherwise, performing an additional experiment and repeating steps (4) to (10) until the research goal is met.

3. Progression of the usage of statistics and DOE in AM and PBF-LB/M

In this section, we quantify whether the standards summarized in Section 2 are currently being followed within AM and PBF-LB/M and determine where the field should be shifting its focus in terms of quality control and hypothesis testing. We do this by performing a literature review of randomly selected papers from AM and categorizing the types of designs and analyses they used. We then determine whether the use of different practices is becoming increasingly sophisticated to match the techniques described in Section 2. We also look for other, perhaps more subtle changes in the way experiments are designed and analyzed by performing a cluster analysis on this data while observing how participation in these clusters changes over time. Next, we compare the relatively unconstrained practices of PBF-LB/M to those of a more tightly regulated field—AM in orthopedic medicine. We conclude by discussing the best papers of those sampled, showing how these can act as models of improvement while still highlighting areas of improvement.

3.1. Description of review methods

To unveil the current standards of statistics and DOE in AM and PBF-LB/M, we performed a literature survey of manuscripts in these fields, which were selected with a stratified random sampling technique. Each study was manually reviewed to identify its experimental design, the statistical methods used to analyze experimental outcomes, and any additional best practices in experimental design. We then quantified the number of studies within each category and examined how these counts varied over time.

First, we created a list of candidate papers for AM in the search engine Scopus. Scopus was selected due to its extensive interdisciplinary coverage, particularly of engineering and technical disciplines, and its intuitive, user-friendly interface, facilitating efficient literature searches and citation analysis. The search term we used was "Additive Manufacturing" AND "Experiment," resulting in 5549 papers. A random set of these papers was quickly assessed for relevance. As all of these papers were engineering papers focused on developing methods for AM, there was no need for further trimming. Another

candidate list of papers was created for PBF using the search terms "Powder Bed Fusion" AND "Experiment" OR "Machine-Learning" AND "Selective Laser Melting" OR "Selective Laser Sintering," and its relevance was checked as well. We included a search term for "machine learning" to capture cases where machine learning models were used to evaluate experimental results instead of or in addition to traditional linear models.

Next, we randomly sampled up to a minimum of 12 papers from each year from 2016 to 2024 in Scopus for both AM and PBF-LB/M, increasing the number of samples every year to reflect the acceleration in publication rates in the field (Table 2). We restricted our analysis to papers published between 2016 and 2024 because this period captures the rapid expansion of AM research following the release of key standards, such as ISO/ASTM 52901 on requirements for purchased AM parts and ISO/ASTM 52915 on standardized AMF file formats,[27,28] ensuring that temporal trends reflect practices developed under a modernized and increasingly standardized framework. Before 2016, papers on this topic were relatively scarce. Each randomly selected paper was vetted to make sure it was an experimental paper (as opposed to a review or theoretical paper). If a paper did not meet this requirement, it was excluded and replaced with a new random paper from that year.

Each paper was assessed on the type of data analysis, the type of experimental design, whether blocking was present, whether the run order was randomized, whether model adequacy checks were performed, whether model selection took place, and whether there was some justification for the sample size, and finally, the sample size itself was recorded. If aspects of the design were not explicitly stated, attempts were made to estimate values such as sample size from figures or attached datasets. If the sample size, design, or analysis could not be determined from the text alone, the paper was abandoned and replaced with a new randomly selected paper. If other aspects of the design were not stated (such as whether the experiment was performed in random order), it was assumed that this aspect of the design was absent from the study. If there were multiple experiments performed, then data would only be collected on the first experiment mentioned in the text. Figure 2 shows the workflow of the review, and Table 3 gives a brief overview of each of the topics we covered in the review. Each of these topics is discussed in more depth in the companion manuscript.[26]

Table 2. Counts of manuscripts sampled per year across the different manuscript types

Year	All AM	Powder bed fusion	Orthopedic engineering
2016	12	15	10
2017	13	16	0
2018	14	17	0
2019	15	18	0
2020	16	19	0
2021	17	20	0
2022	18	21	0
2023	19	22	0
2024	18	21	10

3.2. Summary results of literature review

Overall, the data reveal no significant temporal trends in the use of design types or analytical methods for either AM or PBF-LB/M. However, the two approaches exhibit differences in the specific designs and analyses they employ. First, we find the proportion of papers each year that utilize different aspects of DOE and ANOVAs for all AM (Figure 3, left panel) and PBF-LB/M (Figure 3, right panel). We then find the proportion of papers each year that perform different data analysis (Figure 4) and use different design types (Figure 5). We then fit a LOESS regression[29] to each category to measure trends over time. In each case, these regressions tend to either remain flat over time or fluctuate wildly, so no significant trends can be predicted from this analysis. Finally, we categorize some designs (full factorial, fractional factorial, Taguchi, central composite, and randomly distributed factor levels) as being more sophisticated than alternative designs and plot the proportion of this group of designs over time. We then performed a linear regression, which includes this proportion as its response variable, while year and field type are predictor variables (Figure 5; linear model: p-values for all effects >0.05, p-value for the model = 0.5866, multiple $R^2 = 0.1249$). Neither their main effects nor interactions are significant, despite that the fit was adequate (residual plots were checked). This means that designs are not becoming increasingly sophisticated over time.

We also investigated differences in experimental practices between AM and PBF-LB/M in aggregate. First, there are no differences in the proportion of good practices used by AM or PBF-LB/M papers (Figure 6A; all sample-size corrected proportion tests have $p>0.05$), nor are there differences in sample sizes (Figure 6B; Wilcoxon test $p>0.05$). In addition, there is no difference in the proportion of analyses or experiments present in AM manuscripts than in PBF-LB/M manuscripts. To test this, we performed a binomial generalized linear model (GLM) with the main effects of analysis type and manuscript type, as well as an interaction between these two factors. This interaction between PBF-LB/M and the type of analysis has a $p>0.05$

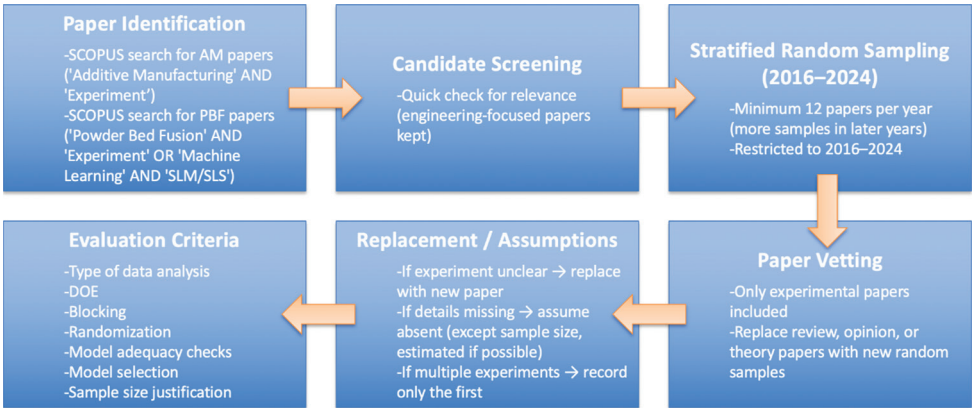

Figure 2. Flow diagram of the process of conducting a literature review on statistical and experimental practices within AM. Image created by the authors.
Abbreviations: AM: Additive manufacturing; DOE: Design of experiments; PBF: Powder bed fusion; SLM: Selective laser melting; SLS: Selective laser sintering.

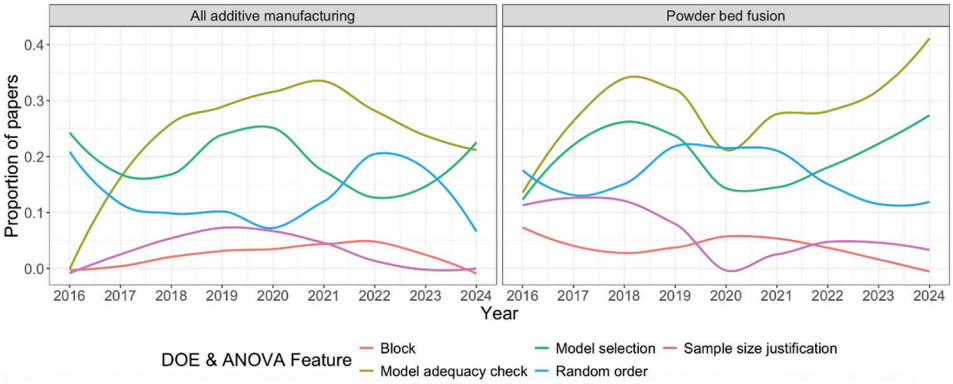

Figure 3. LOESS regression of the proportion of papers that use a DOE practice (color) for additive manufacturing overall (first panel) and PBF-LB/M specifically (second panel). Image created by the authors.
Abbreviations: ANOVA: Analysis of variance; DOE: Design of experiments; PBF-LB/M: Laser-based powder bed fusion of metals.

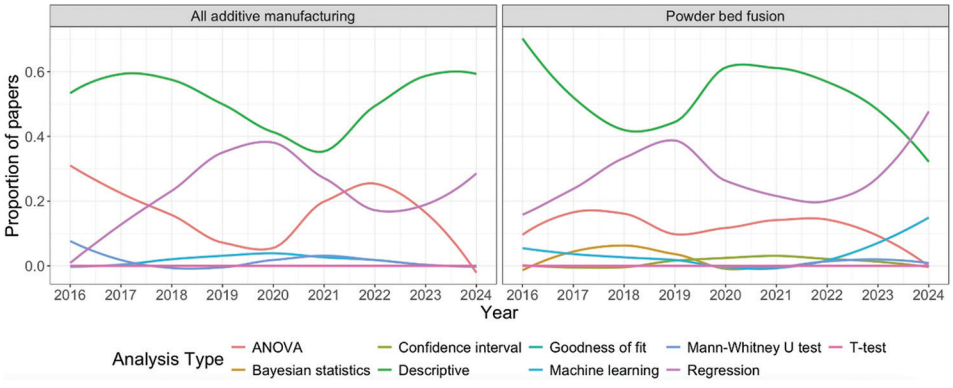

Figure 4. LOESS regression of the proportion of papers that use a statistical analysis (color) for additive manufacturing overall (first panel) and PBF-LB/M specifically (second panel). Image created by the authors.
Abbreviations: ANOVA: Analysis of variance; DOE: Design of experiments; PBF-LB/M: Laser-based powder bed fusion of metals.

for both the proportion of analyses used (Figure 6C) as well as the types of designs used (Figure 6D). This p-value was calculated from a Chi-square test on deviance, and it has been corrected for unequal sample sizes.

3.3. Cluster analysis

Table 3. Overview of key concepts in statistics and experimental design relevant to AM research

Category	Topic	Description/goal	Examples
DOE and ANOVA feature	Blocks	Reduce variability by grouping similar experimental units	Blocking by machine, operator, day
DOE and ANOVA feature	Model adequacy checks	Ensure model assumptions are met	Residual plots, normality checks, and homoscedasticity
DOE and ANOVA feature	Random order	Avoid confounding with time-related effects	Randomized run order in DOE
DOE and ANOVA feature	Model selection	Choose the best-fitting and parsimonious model	AIC, BIC, stepwise selection
DOE and ANOVA feature	Sample size justification	Ensure sufficient power for detecting effects	Power analysis, economic justification for sample size
Statistical analysis	ANOVA	Test differences among group means	One-way ANOVA, two-way ANOVA, repeated measures ANOVA
Statistical analysis	Confidence intervals	Estimate the range of parameter values	95% CI for mean or regression coefficients
Statistical analysis	KS-Test	Compare the distribution of data with the reference distribution	Kolmogorov–Smirnov test for normality, a subset of goodness of fit tests
Statistical analysis	Mann–Whitney *U* test	Compare medians of two independent groups	Example of non-parametric statistics such as the Kruskal–Wallis test
Statistical analysis	*t*-tests	Compare the means of groups	One-sample, two-sample, and paired *t*-test
Statistical analysis	Bayesian statistics	Update beliefs with data	Bayesian inference, priors, and posteriors
Statistical analysis	Descriptive statistics	Summarize data	Mean, median, variance, and kurtosis
Statistical analysis	Machine learning	Model complex relationships or classifications	Decision trees, random forests, and neural networks
Statistical analysis	Regression	Model the relationship between variables	Linear regression, logistic regression, and polynomial regression
Experimental design types	Box–Behnken	Optimize the response surface with fewer runs	3-level design excluding extremes
Experimental design types	Fractional factorial	Reduce runs using a subset of factorial combinations	Half fraction of 2^k design
Experimental design types	One factor at a time	Vary one factor while holding others constant	Simple screening method
Experimental design types	Repeated trials	Estimate variability and improve reliability	Performing the same experiment multiple times
Experimental design types	Taguchi	Robust design emphasizing signal-to-noise ratios	Orthogonal arrays for process optimization
Experimental design types	Central composite	Fit quadratic models in response surface methodology	Axial points+factorial design
Experimental design types	Full factorial	Study all combinations of factors	2^k full factorial design
Experimental design types	Single factor	Investigate one factor in detail	Compare multiple levels of a single factor
Experimental design types	Randomly distributed factor levels	Capture variability across random settings	Random selection of design points

Abbreviations: AIC: Akaike information criterion; AM: Additive manufacturing; ANOVA: Analysis of variance; BIC: Bayesian information criterion; CI: Confidence interval; DOE: Design of experiments.

To better understand trends in experimental design over time, we performed a cluster analysis to automatically categorize different papers and then see how frequencies in these groups change over time. The variables that were used in the cluster analysis were whether a paper used blocking, randomization, checked for model adequacy, performed model selection, and used a power analysis. Each of these variables is binary. In addition, we also input the type of experimental design and the type of data analysis used. Finally, we incorporated the sample size. While this is a continuous variable, all other factors are categorical. As we used Gower distance to calculate the dissimilarity matrix,[30] which is only valid for categorical variables, we converted the sample size

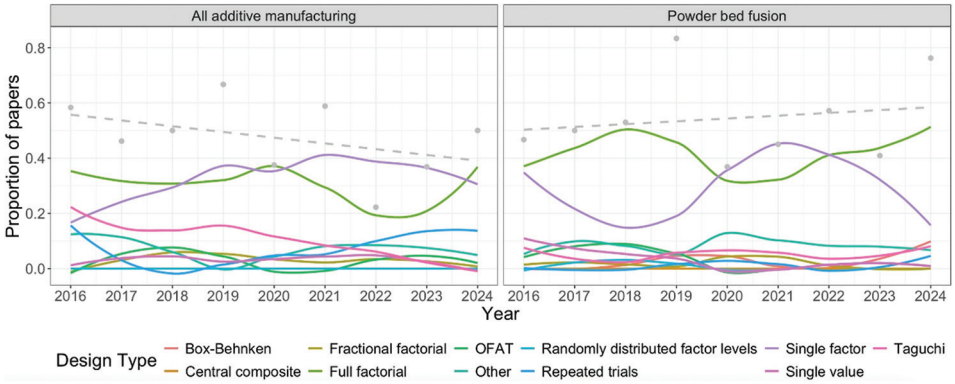

Figure 5. LOESS regression of the proportion of papers that use different experimental designs (color) for additive manufacturing overall (first panel) and PBF-LB/M specifically (second panel). Gray points represent the sum of sophisticated designs (Box-Behnken, fractional factorial, full factorial, central composite, Taguchi), while the gray dashed line shows the linear regression between time and these sophisticated designs. Image created by the authors.
Abbreviations: ANOVA: Analysis of variance; OFAT: One factor at a time; PBF-LB/M: Laser-based powder bed fusion of metals.

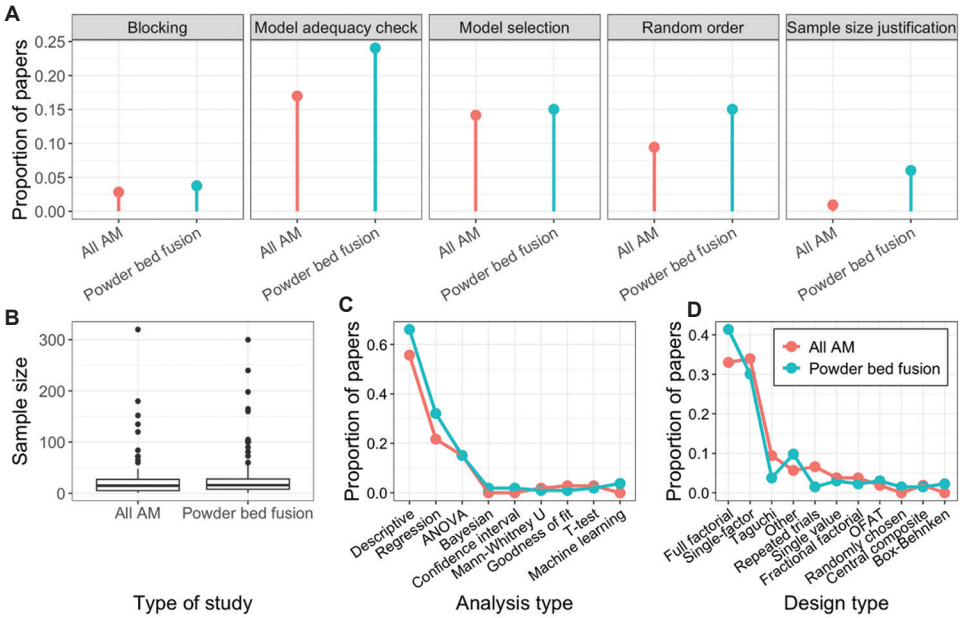

Figure 6. Lack of statistically significant differences in the practice of experimental statistics between all AM and PBF-LB/M categories. (A) The proportion of papers which utilize a particular experimental method (panels) between AM (red) and PBF-LB/M (blue). (B) The sample sizes across manuscripts pertaining to AM and PBF-LB/M. (C) The proportion of papers which utilize a particular type of analysis. (D) The proportion of papers which utilize a particular experimental design. Image created by the authors.
Abbreviations: AM: Additive manufacturing; ANOVA: Analysis of variance; OFAT: One factor at a time; PBF-LB/M: Laser-based powder bed fusion of metals.

to either being large or small, depending on whether a paper's sample size was higher or lower than the mean sample size. We performed the cluster analysis for AM and PBF separately.

After calculating the dissimilarity matrix with Gower distance, we evaluated the silhouette width of two clustering algorithms (AGNES, DIANA[31]) across 2–15 clusters, finding the algorithm and cluster number which maximizes the silhouette width. For both AM and PBF, two clusters using the DIANA algorithm maximized the width. To characterize the cluster, we then calculated the percentage of observations of each factor level within each cluster (Figure 7A and B). Finally, we tracked the percentage of papers within a year that were in the second cluster, plotting the results of a LOESS regression to ease the interpretation of the time-series (Figure 7C).[32]

In general, the second cluster of AM and PBF uses fewer experimental designs, focusing on response surface

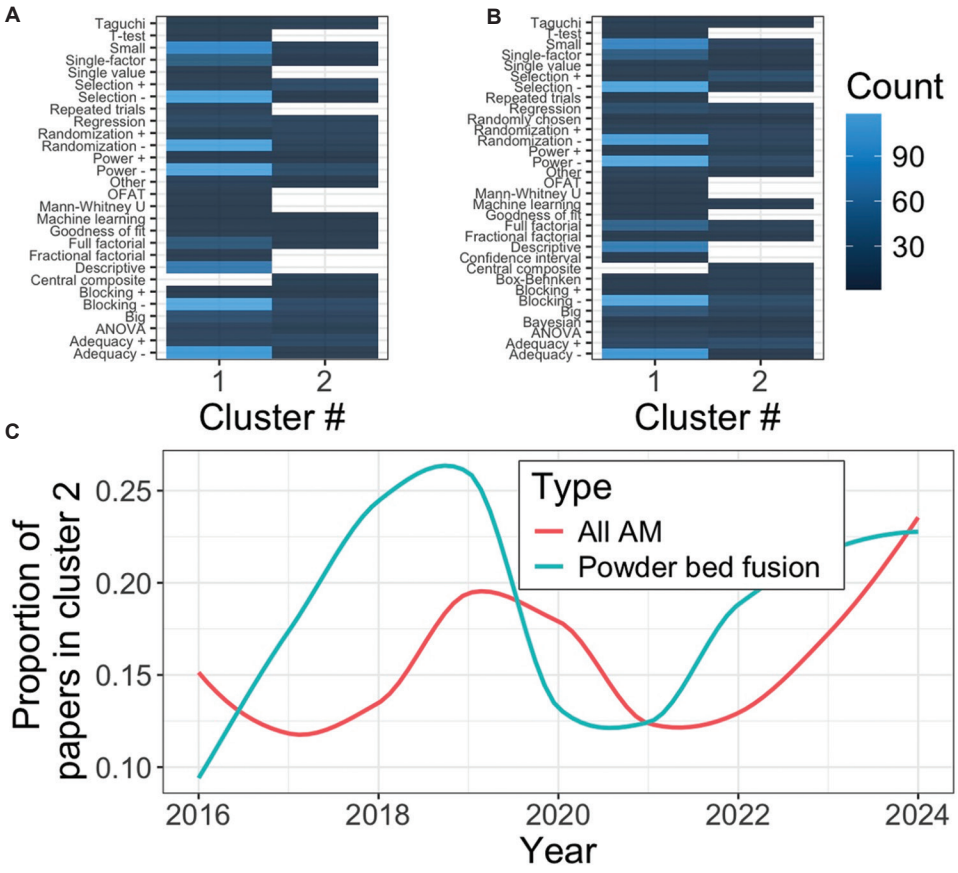

Figure 7. Lack of a consistent trend in how the sophistication of experiments and statistics changes in all AM and PBF-specific categories. Distribution of all (A) AM datasets, and (B) PBF datasets. The x-axis represents the clusters to which different papers belong, and the y-axis gives different features of the dataset. A "+" indicates that a particular technique was used, such as blocking. "-" means that this technique was not used. (C) Percent of papers in cluster 2 across years for AM (red) and PBF (blue). "Big" and "small" refer to the sample size. Image created by the authors.
Abbreviations: AM: Additive manufacturing; PBF: Powder bed fusion.

designs such as central composite, Box–Behnken, and Taguchi designs. In addition, the second cluster uses fewer types of analyses, using regression or ANOVA. These papers also tended to use proper experimental techniques such as randomization and blocking. Papers in this second cluster, then, used the DOE in their studies. The proportion of papers in cluster 2 do not show a consistent trend over time, instead following a sine-wave pattern with an extremely small magnitude (roughly 0.075). This pattern is roughly matched by PBF, although it may be offset by a couple of years. This could indicate that, in the past, there may have been some improvements in the use of the field, but any progress made was lost. The reason for that is currently unknown, but a potential explanation is the entrance of new researchers and new peer reviewers, publications that are not as strict in experimental statistical application as more senior researchers. Even if this upswing is real, the proportion of papers using proper designs and analyses is still small, and thus, further improvements need to be made. Still, the presence of this sine wave-like cycle makes it unclear whether there is a general trend toward more sophisticated designs.

3.4. AM in orthopedic research versus PBF-LB/M

One potential reason for the vast diversity of experimental designs and statistical analyses in AM is the lack of a generally accepted standard. However, research in medical fields requires human or animal subjects and thus requires the approval of institutional review boards[33] as well as regulatory agencies such as the Food and Drug Administration (FDA) or the European Medicines Agency[34]; therefore, there is higher pressure for standardization. Mechanical testing of additively manufactured orthopedic implants must demonstrate that the device can withstand clinically relevant loading conditions and that the manufacturing process produces consistent properties across builds. Standards such as ASTM F3001 and F2924 specify chemical composition, microstructure, and minimum mechanical property requirements for titanium alloys produced via PBF, while

device-specific protocols (e.g., ASTM F382 for bone plates, ASTM F2077 for intervertebral fusion devices, and ISO 7206 series for hip joint prostheses) define test methods for static and dynamic loading, fatigue life, and wear performance.[35,36] These standardized methods provide clear procedures for specimen preparation, loading regimes, and acceptance criteria, ensuring reproducibility and comparability across laboratories.

Biological safety is addressed through the ISO 10993 series, which provides detailed protocols for evaluating cytotoxicity, sensitization, irritation, systemic toxicity, and long-term effects of implantable materials.[37] These tests are essential for verifying that residual powders, post-processing treatments, or unique surface morphologies generated during AM do not introduce biocompatibility risks. Alongside mechanical and biological testing, robust statistical analysis is required to substantiate compliance claims. Standards such as ISO 16269 (statistical interpretation of data) and ASTM E2709/E2810 (statistical methods for demonstrating conformance with specification limits) offer frameworks for determining sample sizes, confidence intervals, and equivalence margins.[38,39] Regulatory guidance, including the FDA's *Technical Considerations for Additive Manufactured Medical Devices*, further emphasizes the importance of justifying statistical methodologies when validating process control and demonstrating equivalence to predicate devices.[40] Together, these frameworks establish a comprehensive basis for experimental verification of safety and performance in AM-produced orthopedic implants. Therefore, 3D printing in medicine—particularly in orthopedics—serves as a valuable point of comparison for highlighting the lack of standardized experimental and statistical practices in PBF-LB/M.

To compare the two fields, we sampled an additional 20 papers from orthopedic research where AM was used to build various anatomical structures with the end goal of patient implantation (which we shall refer to as "orthopedic engineering"). As we did before, we created a list of candidate papers for AM in Scopus. The search term we used was "Orthopedics" AND "3D Printing." A random set of these papers was quickly assessed for relevance. Half of these papers were from 2016, and the rest were drawn from 2024, so that we could compare temporal trends as well as fields. We also analyzed these papers as we did before, noting what types of experimental designs were used in each study, the type of analysis, etc. We compare the proportion of papers using each design to PBF in the same years.

We find that nearly all studies in orthopedic engineering perform either single-factor experiments or full factorial ones (Figure 8A), compared to the more diverse options used in PBF. While they do not use any problematic designs, such as one factor at a time or single-value experiments, they also do not utilize any RSM designs, such as central composite designs (CCD). A similar pattern holds for statistical analyses (Figure 8B). Most orthopedic studies use either an ANOVA or *t*-test and are much less likely to just report descriptive statistics; they also do not use more advanced models, such as a regression. Finally, the proportion of papers that utilized at least one useful DOE feature is higher in orthopedic studies and PBF. This is primarily the case because most studies mentioned that experimenters randomly assigned subjects to different treatment groups. Generally speaking, these patterns have not changed between 2016 and 2024, although the proportion of PBF papers using good experimental strategies does increase (Figure 8C).

3.5. Best of the sampled papers

The use of statistics and DOE is not new to the field of PBF-LB/M. Several manuscripts have successfully used many of the techniques described in this review to address empirical questions. Here, we highlight the best papers we sampled that are focused on PBF-LB/M. These papers were selected based on the number of good experimental practices they used, as well as the clarity in which these practices were explained (Summarized in Table 4).

Vilanova *et al.*[41] used DOE for the classical problem of finding the right parameter combinations that maximize a response variable. It highlights and utilizes the general guidelines for DOE (replication, randomization, etc.), it uses a design which is appropriate for the fitted model (CCD fitted to a second-order regression model), it has a reasonably high sample size, and the response function is well defined. Specifically, they used this design to solve a multi-objective problem where the response variable is a function of the desirability of several process outputs. They reported regression results, the relevant statistics, and the design matrix along with the raw results of the experiment. Overall, they used the highest proportion of proper experimental techniques of those papers we have checked.

The goal of the work of Zhang *et al.*[18] is to use a combination of simulations and experimental designs to find regions of the process parameter space which result in stable prints. They developed printability maps via theoretical simulations, which showed the combinations of parameters that result in different types of defects (if any). They then chose points within each of these regions to determine whether they achieve the predicted, categorical result. The authors used a Latin hypercube design and reported the design matrix along with the raw results. Figure 2 shows an example of how to illustrate an experimental method.

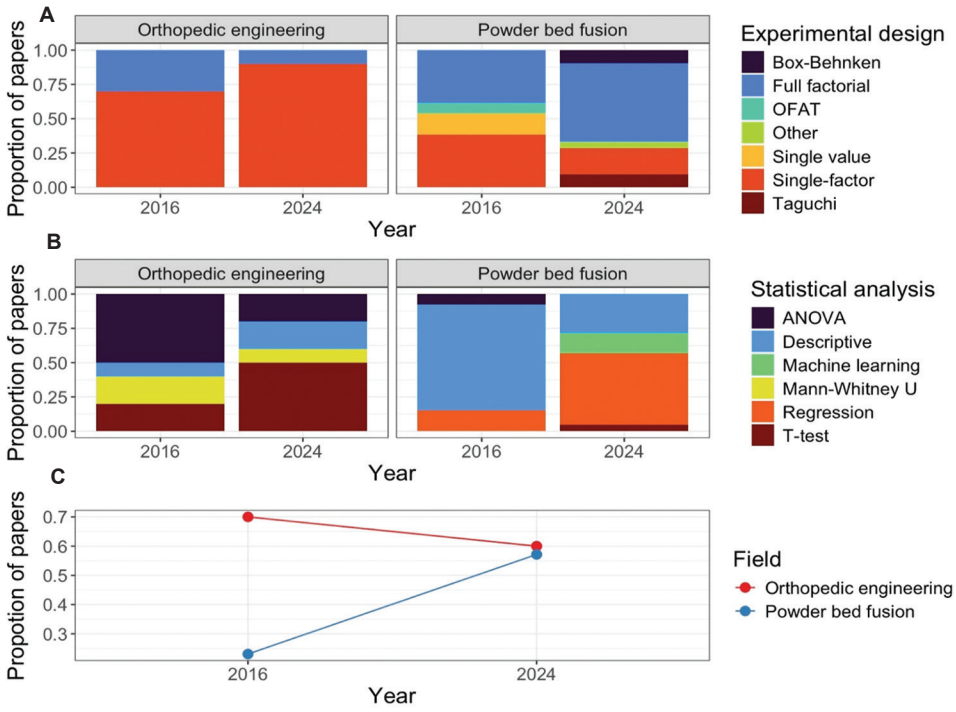

Figure 8. The variety of the statistical and experimental practices used, as well as the level of sophistication across papers pertaining to orthopedic engineering and PBF. (A) The total proportion of papers using various experimental designs per year in each field. (B) The total proportion of papers using various statistical methods per year in each field. (C) The proportion of papers using at least one standardized experimental practice for each field. Image created by the authors.
Abbreviations: ANOVA: Analysis of variance; OFAT: One factor at a time; PBF: Powder bed fusion.

Table 4. Features used in experimental designs and statistical analyses of the highest-quality sampled papers

Manuscript	Experimental design recommendations					Statistical recommendations			
	Sample size justification	Randomization	Blocking	Standard design	Design matrix given	Statistical test	Model selection	Model adequacy	Plot results
Vilanova *et al.*[41]	✓	✓		✓	✓	✓	✓	✓	✓
Zhang *et al.*[18]	✓			✓	✓			✓	✓
Pfaff *et al.* [42]		✓		✓		✓	✓	✓	✓
Flores Ituarte *et al.*[43]				✓		✓		✓	✓
Tyagi *et al.*[44]				✓	✓	✓		✓	✓

Note: Each of the papers, except for Flores Ituarte *et al.*,[43] adopted a response surface methodology design, which used a full factorial design [Table 1].

Pfaff *et al.*[42] designed a general method of finding the process parameters necessary to maximize print quality. They pointed out the benefits of using a CCD, fitting a second-order model, made suggestions for the most important predictor variables for PBF-LB/M while showing the importance of setting parameter ranges, and also discussed the advantages of aspects of DOE such as randomization and using contour plots to find operating conditions. They also covered some topics that we do not include in this paper, such as calibrating empirical results to an underlying theoretical model. Figures 1, 2, 7, and 8 show examples of how to demonstrate experimental designs and visually show response surfaces.

The paper by Flores Ituarte *et al.*[43] is perhaps the most straightforward paper yet: it focuses on only identifying the process parameters that influence the quality of prints (tensile strength, porosity, etc.). They performed a screening experiment but used a full factorial design, which is inefficient. However, without reporting the design matrix, it is not entirely clear what exact type of design was used, or if they randomized the run order. They used an ANOVA to determine the significance of factor effects and

then fit single-factor polynomial trends to each factor and effect after the ANOVA, and they utilized contour plots across different response variables to find samples which minimize all defects. Tables 1 and 2 depict how one can efficiently report an experimental design and how to report the results of an ANOVA, respectively.

Tyagi *et al.*,[44] like Flores Ituarte *et al.*,[43] are interested in determining factors that significantly influence features of tensile bars, such as tensile and compressive strength. This work used Taguchi's L27 design and performed an ANOVA on the results.[44] Interestingly, they only investigated the main effects of the model, even though they could have used a second-order model, but their analysis seems appropriate for their research questions. The authors also presented the appropriate ANOVA table and reported their design matrix along with raw results. One major issue is that some of their analyses were conducted using signal-to-noise ratios, but without elaboration on why they were utilized. In his work, Taguchi defined several signal-to-noise ratios,[45] but it is not clear which of these (if any) the authors used in the study.

While each of these papers generally used DOE effectively, there is still an opportunity for growth. Specifically, authors should report whether they checked assumptions of their models, and why a specific statistical model was selected. In addition, sequential experiments can be performed, and a diverse range of models and designs not used in these papers are available. By elucidating the relevant literature, we aim to simplify the selection process of appropriate models and designs for use in PBF-LB/M experiments.

4. Concluding remarks

4.1. Current practices and limitations

AM is a complex technical field, where the variance in the response of an experiment may be introduced in many steps of the process. This variance should be minimized by the experimental design and/or accounted for in the statistical model. While a few studies in the field demonstrate good practice in this area, most of the sampled manuscripts did not explicitly justify their choice of experimental design in terms of minimizing the effect of inherent variance on the results. Unfortunately, based on the papers reviewed, this situation is not improving with time, or at least not improving significantly. We also conclude that the experimental practices of PBF-LB/M do not differ from AM at large. However, neither field in general utilizes the most accepted standard best practices of DOE. About half of the sampled papers do not perform any statistics beyond just summarizing aspects of their data, such as the mean response (descriptive statistics). Most of the remaining papers perform either a regression analysis, an ANOVA or both. Rarely are more advanced analyses performed, such as Bayesian statistics and GLM. This means that only half of the sampled papers use analyses that would quantify the confidence that they had in their results. It is also not clear if the other half of the papers even used appropriate statistics. Very few papers performed model adequacy checks or used model selection techniques to find the best model. More worrisome, the sample points drawn in an experiment may also not be independent of one another due to the lack of randomization. This can have severe consequences, as an improperly randomized experiment can conflate lurking variables with treatment effects and can introduce bias.[46,47] Furthermore, extraneous sources of variation are often not accounted for with experimental blocking, and the sample sizes used may not have been properly determined considering the appropriate signal-to-noise ratio. This is not to suggest that these practices were not performed, but rather that, at best, they were not reported. Therefore, our estimate for the frequency of these practices is likely an underestimate. However, this still represents a problem, as the important aspects of the design need to be reported so that the audience has the tools to replicate the reported results. Another potential source of bias stems from the fact that all of the studies reviewed originate from academia; private companies rarely disclose their experimental practices, even in patent filings, meaning that our analysis cannot capture the design and statistical approaches being used in industrial settings.

In addition, the field appears to be stagnant with regard to the use of more sophisticated experimental techniques, as the usage of useful RSM and screening designs has not changed over recent years. This finding was validated by our cluster analysis, where we found that for both AM and PBF-LB/M, all the manuscripts tend to cluster into two broad categories: Those that use RSM as well as other standard experimental practices, such as randomization, and those that utilize some of these practices but tend to perform experiments poorly. We found that participation in these clusters did not change over time for PBF-LB/M, and in fact, in all AM, participation in the latter cluster is increasing with time, highlighting an urgent need to improve the nature of the experiments in the field.

4.2. Recommendations and future directions

Unlike traditional methods that generally shape pre-existing materials, AM builds both the material and geometry simultaneously. This "material creation *in situ*" greatly increases the likelihood that a part can be used immediately after the build, which, in turn, elevates the importance of rigorous statistical processes to guarantee consistency, reliability, and performance in end-use

applications. We therefore recommend the development of a list of standard experimental statistics practices to be used in AM. What is outlined in this paper is a proposed first step in this direction. For instance, the researcher reporting the results of experiments would mention the type of design used, the purpose, and a justification for the sample size used. The steps for selecting the statistical model, as well steps to evaluate the adequacy of that model, should be given. Finally, the results of the final regression and ANOVA should be shown (*t*-value, the number of degrees of freedom, R^2, *p*-value, regression coefficients, etc.).

Standardization, though, does not necessarily entail the use of more rigorous analyses and designs. Studies using 3D printing to replace orthopedic tissue use standard designs (mostly single-factor) and analyses (ANOVA and *t*-test), which are sufficient for simple hypothesis testing; they are not efficient insofar as they only test one hypothesis at a time, and they may ignore nonlinear effects such as those modeled by interactions and quadratic terms. Given that any experimental result is likely the product of multiple interacting variables, multiple hypotheses should be tested simultaneously using RSM designs to ensure the economic viability and the robustness of the final result.[48] In addition, the use of proper experimental techniques did not change much between 2016 and 2024. Standardization, then, should also include higher standards for experimental statistics.

Still, the use of even these basic designs and analyses likely helps buffer the medical field against the crisis of replication, as improper designs can artificially inflate false positive rates.[49] In medicine, unreproducible results are unacceptable given the potential cost of human life, but they should also not be tolerated in any scientific field. Despite this, multiple engineering fields have been slow to adopt DOE methods,[50,51] potentially contributing to a replicability crisis in the engineering field akin to that seen in psychology.[52] Steps should also be taken to ensure the validity of the statistical model, as model misspecification can result in incorrect inferences, further fueling issues with reproducibility.[53,54] In addition, model misspecification caused by multicollinearity can also reduce the precision of these models and inflate type I error rates.[54] At the very least, we encourage AM practitioners to adopt the practices used in orthopedic engineering to avoid these problematic outcomes.

That said, we still advocate for stronger experimental designs, which can reduce the cost of experimentation in numerous ways.[23,25,48] The most common design choice in AM studies was the generalized full factorial design. While suitable in many cases, it is often information-inefficient compared to fractional factorial and other related designs. However, this only represents about 35% of all sampled papers, while most others use poor experimental designs such as one factor at a time and single-factor experiments. The first design necessarily excludes interactions from statistical models, and the latter design only explores a single source of variation. Other papers also may not run a formal design at all and only report the results of a single run or repeated runs of the same design point. Very few experiments used standard RSM designs, such as a CCD. One design which has been confused for a standard RSM design is the group of Taguchi designs, which were designed for the field of robust parameter design.[55,56] These designs are meant to minimize the effect of noise factors on a response variable by adjusting the values of control factors. Despite requiring an excessive number of runs compared to a similarly sized fractional factorial design, the approach does not accommodate potentially important control factor interactions.[57] When all factors are controlled, but some are inadvertently treated as noise factors, important low-level interactions can be missed or misinterpreted. In addition, if the split-plot nature of the design is not accounted for in the fitted models, the power of the test can be lowered. If Taguchi designs are to be used outside of their intended context, they should be combined with traditional response surface methods to control for these shortcomings.[58] However, in our literature review, we found that Taguchi designs were used in place of other designs, which is problematic. Instead, practitioners could be using CCDs, Box–Behnken designs, and computer-generated designs, which optimize various selection criteria such as D-efficiency, when evaluating a response surface. Full factorial and fractional factorial designs should be used for screening factors.

Given that trends in the use of these analyses and designs appear to remain unchanged over time, there is a need to re-evaluate their application in AM broadly and in PBF-LB/M specifically. In section 2 and in the companion manuscript to this guide,[26] we present a standardized method of applying DOE methods to AM and PBF-LB/M problems, and discuss the minimum requirements for reporting these methods in a manuscript or report. If these recommendations are implemented, they have the potential to accelerate progress in the field by reducing sample sizes,[48] removing communication barriers imposed by imprecise experimental descriptions, and enhancing the reproducibility of research.[59] These recommendations could also be used in the context of a round-robin study to distribute the costs of the experiments across laboratories.[60] This guide is useful for both practitioners and editors. Peer-reviewed journals, especially those specialized in AM, can request proper use and reporting of experimental statistics, but they can also advocate for better designs. Adoption of

these practices within AM can be tracked over time by a journal or a scientific body by measuring an index of statistical sophistication. Ensuring statistical precision is highly critical for AM since it is used to produce parts for highly regulated industry segments such as aerospace, medicine, and similar fields.

Acknowledgments

None.

Funding

The review described here was performed at The University of Texas at El Paso (UTEP) within the W.M. Keck Center for 3D Innovation (Keck Center). This material is based on research sponsored by Air Force Research Laboratory under Agreement Number FA8650-20-2-5700. The U.S. Government is authorized to reproduce and distribute reprints for Governmental purposes, notwithstanding any copyright notation thereon. Additional support was provided by strategic investments via discretionary UTEP Keck Center funds and the Mr. and Mrs. MacIntosh Murchison Chair I in Engineering Endowment at UTEP. The views and conclusions contained herein are those of the authors and should not be interpreted as necessarily representing the official policies or endorsements, either expressed or implied, of Air Force Research Laboratory or the U.S. Government.

Conflict of interest

The authors declare they have no competing interests.

Author contributions

Conceptualization: Colin Lynch, Ryan Wicker, Rene Villalobos
Visualization: Colin Lynch, Rene Villalobos
Writing–original draft: Colin Lynch, Rene Villalobos
Writing–review & editing: All authors

Ethics approval and consent to participate

Not applicable.

Consent for publication

Not applicable.

Availability of data

The dataset supporting this study is openly available on Zenodo at https://zenodo.org/records/17137612. The file statsAndDOEinAM.csv contains metadata from a systematic review of experimental designs and statistical analyses in AM, including fields for publication details, design type, analysis type, sample size, justification of sample size, model adequacy, model selection, randomization, and blocking. The repository also includes the R script, which will reproduce the figures and analyses in this manuscript.

References

1. Wohlers T. *History of Additive Manufacturing*. Report; 2023.
2. Beaman JJ, Bourell DL, Seepersad CC, Kovar D. Additive manufacturing review: Early past to current practice. *J Manuf Sci Eng*. 2020;142(11):110812.

   doi: 10.1115/1.4048193
3. Gu D, Shi X, Poprawe R, Bourell DL, Setchi R, Zhu J. Material-structure-performance integrated laser-metal additive manufacturing. *Science*. 2021;372(6545):eabg1487.

   doi: 10.1126/science.abg1487
4. ASTM. Standard F2792-09: *Standard Terminology for Additive Manufacturing Technologies*. *Superseded*. United States: ASTM; 2021.
5. Srivatsan TS, Sudarshan TS. *Additive Manufacturing: Innovations, Advances, and Applications*. Boca Raton; CRC Press; 2015.
6. Frazier WE. Metal additive manufacturing: A review. *J Mater Eng Perform*. 2014;23:1917-1928.

   doi: 10.1007/s11665-014-0958-z
7. Hasanov S, Suhas A, Mithila R, *et al*. Review on additive manufacturing of multi-material parts: Progress and challenges. *J Manuf Mater Process*. 2021;6(1):4.

   doi: 10.3390/jmmp6010004
8. ISO/ASTM 52900. *Additive Manufacturing-General Principles-Fundamentals and Vocabulary*. Switzerland: ISO/ASTM; 2021.
9. Blakey-Milner B, Gradl P, Snedden G, *et al*. Metal additive manufacturing in aerospace: A review. *Mater Des*. 2021;209:110008.

   doi: 10.1016/j.matdes.2021.110008
10. Paolini A, Kollmannsberger S, Rank E. Additive manufacturing in construction: A review on processes, applications, and digital planning methods. *Addit Manuf*. 2019;30:100894.

    doi: 10.1016/j.addma.2019.100894
11. Dilberoglu UM, Gharehpapagh B, Yaman U, Dolen M. The role of additive manufacturing in the era of industry 4.0. *Procedia Manuf*. 2017;11:545-554.

    doi: 10.1016/j.promfg.2017.07.148
12. Javaid M, Haleem A. Additive manufacturing applications in medical cases: A literature based review. *Alexandria J Med*. 2018;54(4):411-422.

    doi: 10.1016/j.ajme.2017.09.003

13. Prakash KS, Nancharaih T, Rao VS. Additive manufacturing techniques in manufacturing-an overview. *Mater Today Proc*. 2018;5(2):3873-3882.

doi: 10.1016/j.matpr.2017.11.642

14. Wiese M, Kwauka A, Thiede S, Herrmann C. Economic assessment for additive manufacturing of automotive end-use parts through digital light processing (DLP). *CIRP J Manuf Sci Technol.* 2021;35:268-280.

doi: 10.1016/j.cirpj.2021.06.020

15. Wong KV, Hernandez A. A review of additive manufacturing. *ISRN Mechan Eng*. 2012;2012:208760.

doi: 10.5402/2012/208760

16. Pinto JM, Cristobal A, Marcelo EA, *et al*. Sensitivity analysis of geometric errors in additive manufacturing medical models. *Med Eng Phys.* 2015;37(3):328-334.

doi: 10.1016/j.medengphy.2015.01.009

17. Petruse RE, Puşcaşu S, Pascu A, Bondrea I. Key factors towards a high-quality additive manufacturing process with ABS material. *Mater Today Proc.* 2019;12:358-366.

doi: 10.1016/j.matpr.2019.03.136

18. Zhang B, Raiyan S, Lei X, *et al*. An efficient framework for printability assessment in laser powder bed fusion metal additive manufacturing. *Addit Manuf.* 2021;46:102018.

doi: 10.1016/j.addma.2021.102018

19. Johnson L, Mohamad M, Bing Z, *et al*. Assessing printability maps in additive manufacturing of metal alloys. *Acta Mater.* 2019;176:199-210.

doi: 10.1016/j.actamat.2019.07.005

20. Sun S, Brandt M, Easton MJLAM. Powder bed fusion processes: An overview. In: *Laser Additive Manufacturing*. Netherlands: Elsevier; 2017. p. 55-77.

doi: 10.1016/B978-0-08-100433-3.00002-6

21. Fisher RA. Design of experiments. *BMJ*. 1936;1(3923):554.

22. Hicks CR. *Fundamental Concepts in the Design of Experiments.* New York: Holt, Rinehart and Winston; 1964.

23. Montgomery DC. *Design and Analysis of Experiments.* United States: John Wiley & Sons; 2017.

24. Khuri AI, Mukhopadhyay S. Response surface methodology. *Wiley Interdiscip Rev Comput Stat.* 2010;2(2):128-149.

doi: 10.1002/wics.73

25. Myers RH, Montgomery DC, Anderson-Cook CM. *Response Surface Methodology: Process and Product Optimization Using Designed Experiments*. 4th ed. United States: John Wiley & Sons; 2016.

26. Lynch CM, Wicker RB, Villalobos JR. *An Overview of the Design of Optimal Experiments and Statistical Practices for Scientific and Engineering Applications*. ResearchGate; 2024. Available from: https://www.researchgate.net/publication/383874030_An_overview_of_the_design_of_optimal_experiments_and_statistical_practices_for_scientific_and_engineering_applications [Last accessed on 2025 Sep 27].

27. ISO/ASTM International. *ISO/ASTM 52901:2016 - Additive Manufacturing-General Principles-Requirements for Purchased AM Parts*. United States: ASTM International; 2016.

28. ISO/ASTM International. *ISO/ASTM 52915:2016 - Specification for Additive Manufacturing File Format (AMF), Version 1.2*. United States: ASTM International; 2016.

29. Gijbels I, Prosdocimi I. Loess. *Wiley Interdiscip Rev Comput Stat*. 2010;2(5):590-599.

doi: 10.1002/wics.104

30. Schmitz H, Nadvi K. Clustering and industrialization: Introduction. *World Dev*. 1999;27(9):1503-1514.

31. Wijuniamurti S, Nugroho S, Rachmawati R. Agglomerative nesting (AGNES) method and divisive analysis (DIANA) method for hierarchical clustering on some distance measurement concepts. *J Stat Data Sci*. 2022;1(1):7-11.

doi: 10.33369/jsds.v1i1.21009

32. Rojo J, Rivero R, Romero-Morte J, *et al*. Modeling pollen time series using seasonal-trend decomposition procedure based on LOESS smoothing. *Int J Biometeorol.* 2017;61:335-348.

doi: 10.1007/s00484-016-1215-y

33. Dickersin K, Mayo-Wilson E. Standards for design and measurement would make clinical research reproducible and usable. *Proc Natl Acad Sci* U S A. 2018;115(11):2590-2594.

doi: 10.1073/pnas.1708273114

34. McNair L. Ethical and regulatory oversight of clinical research: The role of the Institutional Review Board. *Exp Biol Med (Maywood)*. 2022;247(7):561-566

doi: 10.1177/15353702221078216

35. ASTM International. *ASTM E2709-12: Standard Practice for Demonstrating Capability to Comply with an Acceptance Procedure*. United States: ASTM International; 2012.

36. ASTM International. *ASTM F2924-14: Standard Specification for Additive Manufacturing Titanium-6 Aluminum-4 Vanadium with Powder Bed Fusion*. United States: ASTM International; 2014.

37. ASTM International. *ASTM F3001-14: Standard Specification for Additive Manufacturing Titanium-6 Aluminum-4 Vanadium ELI (Extra Low Interstitial) with Powder Bed Fusion*. United States: ASTM International; 2015.

38. ASTM International. *ASTM F2077-17: Standard Test Methods for Intervertebral Body Fusion Devices*. United States: ASTM International; 2017.

39. ASTM International. *ASTM F382-19: Standard Specification*

and Test Method for Metallic Bone Plates. United States: ASTM International; 2019.

40. Food and Drug Administration. *Technical Considerations for Additive Manufactured Medical Devices: Guidance for Industry and Food and Drug Administration Staff*. Washington, DC: US Department of Health and Human Services; 2017.

41. Vilanova M, Escribano-García R, Guraya T, San Sebastian M. Optimizing laser powder bed fusion parameters for IN-738LC by response surface method. *Materials (Basel)*. 2020;13(21):4879.

    doi: 10.3390/ma13214879

42. Pfaff A, Jäcklein M, Schlager M, *et al*. An empirical approach for the development of process parameters for laser powder bed fusion. *Materials (Basel)*. 2020;13(23):5400.

    doi: 10.3390/ma13235400

43. Flores Ituarte I, Wiikinkoski O, Jansson A. Additive manufacturing of polypropylene: A screening design of experiment using laser-based powder bed fusion. *Polymers (Basel)*. 2018;10(12):1293.

    doi: 10.3390/polym10121293

44. Tyagi B, Dubey D, Sahai A, Sharma RS. Mechanical properties evaluation of FFF-printed ABS samples based on different process parameters combined with ANOVA and regression analysis. *Proc Inst Mech Eng C J Mech Eng Sci*. 2023;238(7):09544062231151540.

    doi: 10.1177/09544062231151540

45. Roy RK. *A Primer on the Taguchi Method*. Michigan: Society of Manufacturing Engineers; 2010.

46. Vorland CJ, Brown AW, Dawson JA, *et al*. Errors in the implementation, analysis, and reporting of randomization within obesity and nutrition research: A guide to their avoidance. *Int J Obes (Lond)*. 2021;45(11):2335-2346.

    doi: 10.1038/s41366-021-00909-z

47. Kang M, Ragan BG, Park JH. Issues in outcomes research: An overview of randomization techniques for clinical trials. *J Athl Train*. 2008;43(2):215-221.

    doi: 10.4085/1062-6050-43.2.215

48. Lynch CM, Montgomery DC. Optimal experimental designs for hypothesis testing with multiple factors: Maximising power for the biological sciences. *Int J Exp Des Process Optim*. 2024;7(2):105-114.

    doi: 10.1504/IJEDPO.2024.140455

49. Lynch CM, Starkey M, Montgomery D, Pavlic TP, Mizumoto N. More individuals or more groups? Incorporating sampling effort, statistical power, and model accuracy when designing experiments. *Behav Ecol Sociobiol*. 2025;79(106).

    doi: 10.1007/s00265-025-03640-1

50. Tanco M, Viles E, Jesus Álvarez M, Ilzarbe L. Why is not design of experiments widely used by engineers in Europe? *J Appl Stat*. 2010;37(12):1961-1977.

    doi: 10.1080/02664760903207308

51. Hoerl RW, Snee RD. Statistical engineering: An idea whose time has come? *Am Stat*. 2017;71(3):209-219.

    doi: 10.1080/00031305.2016.1247015

52. Shrout PE, Rodgers JL. Psychology, science, and knowledge construction: Broadening perspectives from the replication crisis. *Annu Rev Psychol*. 2018;69:487-510.

    doi: 10.1146/annurev-psych-122216-011845

53. Zhang W, Yan S, Tian B, Fei D. Statistical assumptions and reproducibility in psychology: Data mining based on open science. *Front Psychol*. 2022;13:905977.

    doi: 10.3389/fpsyg.2022.905977

54. Frost J. *Introduction to Statistics*. Statistics by Jim Publishing; 2019. Available from: https://statisticsbyjim.com/basics/correlations [Last accessed on 2025 Sep 27].

55. Taguchi G. *Introduction to Quality Engineering: Designing Quality into Products and Processes*. Tokyo: Asian Productivity Organization; 1986.

56. Taguchi G. *System of Experimental Design: Engineering Methods to Optimize Quality and Minimize Costs*. Vol. 1. Dearborn: UNIPUB/Kraus International Publications; 1987.

57. Borror CM, Montgomery DC. Mixed resolution designs as alternatives to Taguchi inner/outer array designs for robust design problems. *Qual Reliab Eng Int*. 2000;16(2):117-127.

    doi: 10.1002/(SICI)1099-1638(200003/04)16:2<117:AID-QRE309>3.0.CO;2-0

58. Vining GG, Myers RH. Combining Taguchi and response surface philosophies: A dual response approach. *J Qual Technol*. 1990;22(1):38-45.

    doi: 10.1080/00224065.1990.11979204

59. Samuel S, König-Ries B. Understanding experiments and research practices for reproducibility: An exploratory study. *PeerJ*. 2021;9:e11140.

    doi: 10.7717/peerj.11140

60. Moylan S, Brown CU, Slotwinski J. Recommended protocol for round robin studies in additive manufacturing. *J Test Eval*. 2016;44(2):1009.

    doi: 10.1520/JTE20150317

ACCSCIENCE PUBLISHING

Engineering Science in Additive Manufacturing

REVIEW ARTICLE

Machine learning-driven additive manufacturing of biomedical metals: A review of forward prediction, inverse optimization, and quality control

Yi Mao[1], Deyu Jiang[1], Uglov Vladimir[2], Zhou Jing[3]*, and Liqiang Wang[1]*

[1]State Key Laboratory of Metal Matrix Composites, School of Material Science and Engineering, Shanghai Jiao Tong University, Shanghai, China

[2]Laboratory of NanoElectroMagnetics, Institute for Nuclear Problems, Belarusian State University, Minsk, Belarus

[3]Department of Anatomy, Youjiang Medical University for Nationalities, Baise, Guangxi, China

Abstract

Additive manufacturing (AM) for biomedical metals presents revolutionary opportunities for producing personalized, complex structured biomedical components. However, the high nonlinearity and complexity of the manufacturing process pose significant challenges to the performance consistency of biomedical metals. Traditional trial-and-error approaches and experience-based optimization methods are increasingly inadequate for meeting the demands of high-reliability medical applications. In recent years, machine learning (ML) has emerged as a powerful data-driven tool, deeply integrating into every stage of AM for biomedical metals and providing a driving force for its intelligent transformation and upgrading. This review outlines three key applications of ML in biomedical metal AM: at the property prediction stage, ML enables forward prediction of performance characteristics by establishing precise mapping relationships between process parameters and macrostructure quality, microstructure, and mechanical/functional properties; at the process optimization level, ML-driven inverse optimization algorithms efficiently navigate high-dimensional parameter spaces to achieve both single-objective perfection and multi-objective balancing; at the quality monitoring and control level, ML enables real-time diagnosis of manufacturing defects and even closed-loop adaptive control by integrating multiple *in situ* sensor data. This review explores how ML can facilitate the biomedical metals during the AM process and outlines its future development toward fully integrated intelligent design and manufacturing processes.

Keywords: Machine learning; Additive manufacturing; Biomedical metals; Forward prediction; Inverse optimization; Quality control and monitoring

***Corresponding authors:**
Liqiang Wang
(wang_liqiang@sjtu.edu.cn)
Zhou Jing
(zhoujing_goplay@163.com)

Citation: Mao Y, Jiang D, Vladimir U, Jing Z, Wang L. Machine learning-driven additive manufacturing of biomedical metals: A review of forward prediction, inverse optimization, and quality control. *Eng Sci Add Manuf*. 2025;1(4):025440031. doi: 10.36922/ESAM025440031

Received: October 29, 2025

Revised: November 24, 2025

Accepted: November 26, 2025

Published online: December 5, 2025

1. Introduction

Biomedical metals, such as titanium and its alloys,[1] cobalt-chromium alloys,[2] biodegradable magnesium/zinc alloys,[3] and medical-grade stainless steel,[4] are widely

used in implant manufacturing for orthopedics, dentistry, and cardiovascular applications[5] due to their superior mechanical properties, biocompatibility, and corrosion resistance. With the significant trend of global population aging and the widespread increase in health awareness, the market demand for biomedical materials (such as those used in joint replacement, dental restoration, and trauma treatment) has experienced explosive growth.[1] Ideal biomedical metals require personalized geometric shapes that precisely match the patient's individual anatomy. In addition, to promote osseointegration and avoid the stress shielding effect, the internal structure is typically designed as porous and possesses mechanical properties matching those of natural bone tissue.[6-8] However, traditional manufacturing processes such as forging and casting suffer from inherent limitations including extremely low material utilization, difficulty in precisely controlling internal pore structures, and inability to achieve personalized customization, severely restricting their clinical application.[9] In contrast, additive manufacturing (AM), an advanced layer-by-layer fabrication technology, leverages its digital and high-freedom manufacturing characteristics to precisely form personalized biomedical metals that closely match patient anatomy. It can also construct biomimetic bone scaffolds with complex porous structures, effectively promoting bone tissue ingrowth, enhancing osseointegration, and significantly reducing stress shielding risks.[10]

1.1. Introduction to AM technologies for biomedical metals

In the field of medical metal AM, multiple mainstream technologies are applicable to different clinical scenarios due to their unique process characteristics.[11] The most widely applied techniques currently include laser beam powder bed fusion (LB-PBF), electron beam powder bed fusion (EB-PBF), and directed energy deposition (DED) (Figure 1).

LB-PBF employs a high-energy laser beam to selectively melt layers of metal powder, achieving layer-by-layer manufacturing through rapid solidification. This technology is renowned for its exceptional forming precision and capability to produce complex structures, enabling the fabrication of components with high density, fine grain structure, and uniform microstructure.[12] Research indicates that commercially pure titanium and Ti-6Al-4V alloy components formed through LB-PBF exhibit significantly superior microhardness, compressive strength, and tensile strength compared to those produced by conventional processes.[13]

EB-PBF differs from LB-PBF by utilizing a high-energy electron beam as the heat source, typically operating in a vacuum environment, and preheating the powder bed before melting. This approach helps reduce residual stresses and control microstructure.[14,15] EB-PBF technology excels in manufacturing titanium alloy implants with simulated bone stiffness characteristics, effectively mitigating the stress shielding effect.[16]

DED, as one of the most mature industrial AM technologies, fundamentally involves the controlled deposition of metal powder.[17] The DED technique includes laser powder DED and laser wire DED and electron beam DED. DED technique offers advantages such as high printing speeds, the ability to process large-scale components, compatibility with various metals and alloys, and the capability to manufacture parts from heterogeneous materials. Components produced by this technology exhibit fine, uniform microstructures due to rapid melting and solidification under high-energy lasers, resulting in excellent mechanical properties and near-complete density. It is also suitable for complex surface deposition and part repair.

Research data further confirm that biomedical metal AM significantly surpasses traditional processes in key performance metrics (Table 1). Attar *et al.*[18] demonstrated that commercially pure titanium components produced through LB-PBF exhibit markedly higher microhardness, compressive strength, and tensile strength than conventionally fabricated samples, achieving near-full-density microstructures and outstanding comprehensive mechanical properties. Regarding corrosion resistance, Zhao *et al.*[19] noted that Ti-6Al-4V alloy components manufactured through LB-PBF demonstrated outstanding corrosion resistance in tests simulating *in vivo* environments, exhibiting corrosion rates significantly lower than industry standards. Similarly, Bai *et al.*[20] found that Ti-6Al-4V alloy formed using EB-PBF technology exhibited superior corrosion resistance in phosphate-buffered solution compared to conventional forged components. This compelling experimental evidence demonstrates that AM not only overcomes the limitations of traditional processes in producing personalized and complex structures but also achieves substantial breakthroughs in material density, mechanical properties, and service reliability. This establishes a robust technological foundation for developing a new generation of high-performance, customized medical metals.[21]

These technologies are employed to process various biomedical metals; however, each category presents distinct application advantages and manufacturing challenges. Biomedical metals serve as core materials for implants in orthopedics, dentistry, and cardiovascular applications. They can be classified into several major categories:[1]

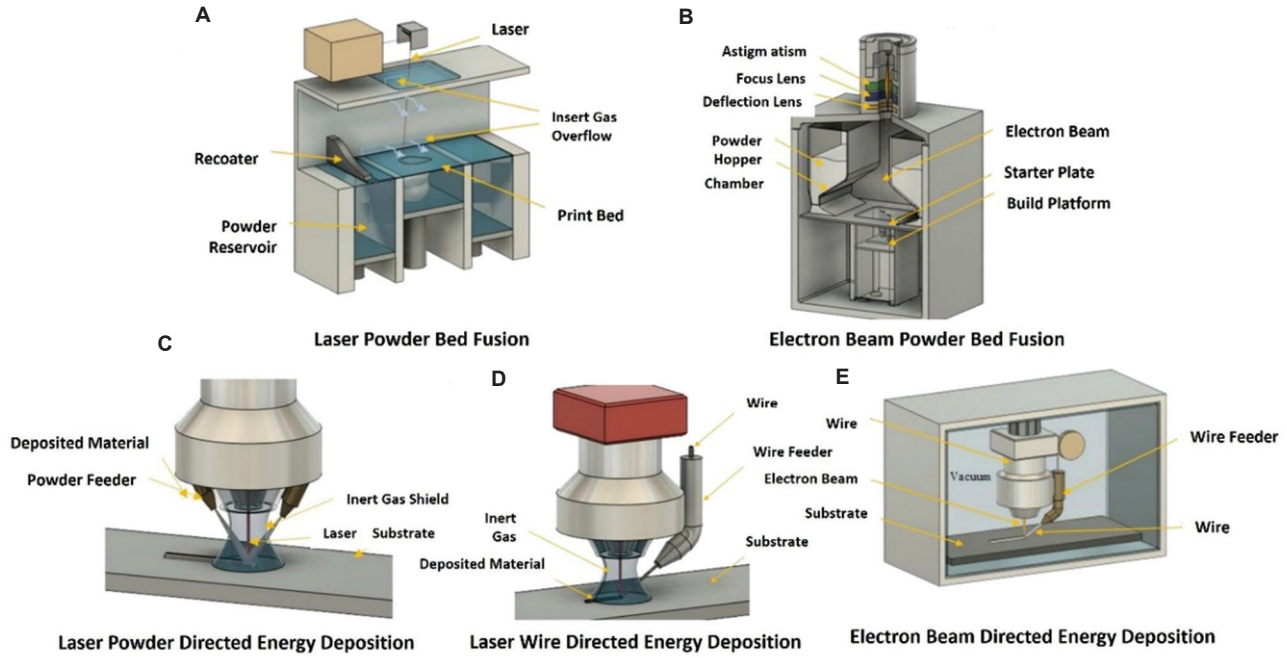

Figure 1. Additive manufacturing techniques used for biomedical metals.[11] (A) LB-PBF; (B) EB-PBF; (C) laser powder DED; (D) laser wire DED; and (E) electron beam DED.
Abbreviations: DED: Directed energy deposition; EB-PBF: Electron beam powder bed fusion; LB-PBF: Laser beam powder bed fusion.

Table 1. Comparison of primary conventional manufacturing processes versus AM for biomedical metals

Feature	Conventional manufacturing processes	AM process	References
Design freedom	Low: constrained by mold and tool accessibility	High: capable of producing complex geometries, lattice structures, and internal channels	6,9
Customization	Challenging and costly	Core advantage: easily achieves implants tailored to patient anatomy	5,10
Material utilization	Low: generates significant waste (subtractive manufacturing)	High: near-net-shape forming, with unmelted powder recyclable	9
Mechanical properties	Isotropic, stable performance	May exhibit anisotropy; properties strongly dependent on process parameters	12,13,18
Microstructure control	Limited by overall heat treatment, restricted control range	Precise and controllable; can be directionally regulated through process parameters and scanning strategies	14
Typical applications	Standard-sized bone plates, screws, and joint stems	Custom acetabular cups, craniofacial implants, porous bone scaffolds	8,10
Primary limitations	Difficulty in manufacturing complex porous structures; high cost of customization	High equipment costs; process monitoring and quality assurance systems still under development	33,35

Abbreviation: AM: Additive manufacturing.

(i) Titanium alloys, particularly Ti-6Al-4V, represent the benchmark material due to their excellent specific strength, corrosion resistance (relying on a surface TiO_2 passivation film), and inherent biocompatibility.[22] β-type titanium alloys (*e.g.*, Ti-Nb-Zr-Ta systems) are especially promising with elastic moduli (~30–60 GPa) closer to human bone (10–30 GPa), effectively mitigating stress shielding. These alloys are widely used in orthopedic implants (e.g., artificial joints and bone scaffolds), dental implants, craniofacial repair components, and cardiovascular stents, especially for load-bearing and long-term implantation scenarios. Researchers further used LB-PBF to fabricate complex porous structures that modulate modulus and promote osseointegration.[23] Therefore, defects need to be suppressed through parameter optimization to enhance relative density and avoid porosity or a lack of fusion, which would degrade fatigue performance.

(ii) Cobalt-chromium alloys possess exceptional wear resistance and high mechanical strength. Ideal for articular prostheses (orthopedics) and dental restorations/implant abutments, where wear resistance and mechanical stability are critical.[24] However, long-term implantation may involve risks of Co/Cr ion release and potential toxicity.[25] AM processes require careful hot cracking control and surface roughness regulation to minimize bacterial adhesion and ion release, combining scanning strategy optimization.

(iii) Medical-grade stainless steels (*e.g.*, 316L) offer cost-effectiveness and good processability.[26] Limitations include relatively inferior corrosion resistance, potential Ni ion-induced allergies, and high elastic modulus. Suitable for short-term orthopedic fixators, prosthetic sockets, and general medical devices, particularly in cost-sensitive, low-load-bearing scenarios. AM focuses on preventing solidification defects by controlling energy density and reducing the evaporation of elements with a high vapor pressure.[27]

(iv) Biodegradable metals represent an emerging frontier in biomaterials research. Magnesium alloys have mechanical properties that match those of human bone and excellent biocompatibility, but they suffer from excessively fast degradation, which makes them prone to premature mechanical failure and hydrogen evolution during corrosion.[28] They can be employed in temporary orthopedic fixators, porous bone scaffolds, and biodegradable cardiovascular stents, avoiding secondary surgery for implant removal. AM focuses on addressing these issues by employing low-energy density to suppress evaporation and balling effects, mitigating challenges associated with magnesium's low boiling point and high vapor pressure, while rapid solidification refines the microstructure to regulate degradation rates.[29] Zinc alloys offer moderate degradation rates and favorable biocompatibility[30,31] but suffer from inadequate mechanical properties and low as-fabricated density in AM processes. To enhance performance, AM strategies focus on optimizing scanning strategies to reduce elemental segregation, thereby improving mechanical integrity. Iron-based biodegradable alloys possess high strength and biocompatibility.[32] However, their degradation is excessively slow, hindering complete absorption within the desired timeframe. AM enables the fabrication of tailored porous structures to accelerate corrosion, making these alloys suitable for load-bearing bone scaffolds and orthopedic fixators.

However, the actual AM process of biomedical metals constitutes a thermo-fluid-solid coupled physical metallurgical process involving rapid solidification, phase transformations, and complex stress evolution.[33] The ultimate result, in relation to the performance and quality of the biomedical metal, is significantly influenced by material composition, powder characteristics, process parameters (*e.g.*, laser power, scanning speed, and scanning strategy), equipment condition, and even environmental factors.[34,35] These factors exhibit strong nonlinear interactions, forming a high-dimensional, complex parameter space. Conventional research and production models are predicated on engineers' experience and extensive trial-and-error experimentation. This not only leads to prolonged development cycles and high costs but also hinders the systematic capture and understanding of underlying patterns. Consequently, this can result in limitations on the performance of the product and a compromise to batch consistency.

1.2. Introduction to machine learning (ML)

ML is a fundamental component of artificial intelligence (AI) that provides a novel approach to addressing the aforementioned limitations. It possesses the distinct capacity to automatically discern patterns from data, facilitating precise predictions and decisions.[33] By continuously acquiring new knowledge and advanced capabilities, and through self-optimization and updating through specific optimization algorithms and other methods, more precise judgment outcomes can be achieved.[36-38] Against the backdrop of rapid AI advancement, ML exhibits increasingly broad applicability. In biomedical metal AM, its implementation typically follows a systematic workflow comprising four key stages: data acquisition and preprocessing, feature engineering, model selection and training, and model evaluation.

With regard to the collection of data, the present corpus of ML data in AM is primarily derived from the following sources:[39,40] Experimental data form the core, encompassing process parameters and mechanical property data obtained through systematic experiments, real-time molten pool dynamics captured via *in situ* monitoring techniques (*e.g.*, thermal imaging and acoustic emission [AE]), and microstructural/defect data derived from microscopic characterization (*e.g.*, scanning electron microscope [SEM] and micro-computed tomography [micro-CT]). However, acquiring experimental data is costly and time-consuming. Second, simulation data, particularly that generated from multi-physics models such as finite element analysis, have been demonstrated to effectively supplement experimental data. Databases formed by integrating public datasets and academic literature, along with industrial production data accumulated by manufacturers, also provide valuable resources for model development. Nevertheless, the latter is

frequently challenging to acquire due to concerns regarding commercial sensitivity.[41,42] To address fundamental challenges such as data scarcity, heterogeneity, and insufficient high-quality labeled data, researchers employ diverse strategies, including multimodal data fusion and transfer learning. Subsequent preprocessing steps, including data sampling, anomaly detection and handling, data discretization, and standardization, have been shown to enhance training efficiency and prediction accuracy.

The objective of feature engineering is to extract or construct features that are most representative of the prediction target from raw data, thus serving as a key factor in enhancing model performance. Common methods include principal component analysis, independent component analysis, categorical encoding, and clustering. The process of feature engineering has been shown to reduce dimensionality, thereby eliminating redundancy and highlighting key parameters that influence material properties.[43,44]

Model selection and training involve choosing appropriate ML algorithms based on specific tasks and data characteristics. ML algorithms are primarily categorized into four types (Figure 2):[45-47]

(i) Supervised learning: Supervised learning models extract feature values and mapping relationships between input and output data from known samples. They assign specific labels to data points and continuously train on sample data relationships to predict unknown data. Supervised learning is further divided into regression and classification. Regression primarily handles continuous variables, while classification deals with discrete variables. Regression algorithms encompass a range of methods, including linear regression, Gaussian process regression (GPR), and regression trees. The applications of regression algorithms in the field of AM primarily encompass the following: process window prediction, process parameter optimization, alloy property prediction, geometric deviation control, and closed-loop control. Common classification algorithms include linear discriminant analysis, naïve Bayes, support vector machines (SVM), K-nearest neighbors, random forest, and classification trees.[48,49] The primary applications of these algorithms encompass defect detection, quality assessment, and geometric deviation control.

(ii) Unsupervised learning: Unsupervised learning algorithms are characterized by their ability to function without the requirement of labeled input-output pairs. Instead, they analyze relationships within known data to categorize and partition data based on inherent patterns.[50] Unsupervised learning algorithms can be categorized into two classifications: clustering and dimensionality reduction. In the context of clustering algorithms, ML involves the division of data into groups of records that exhibit

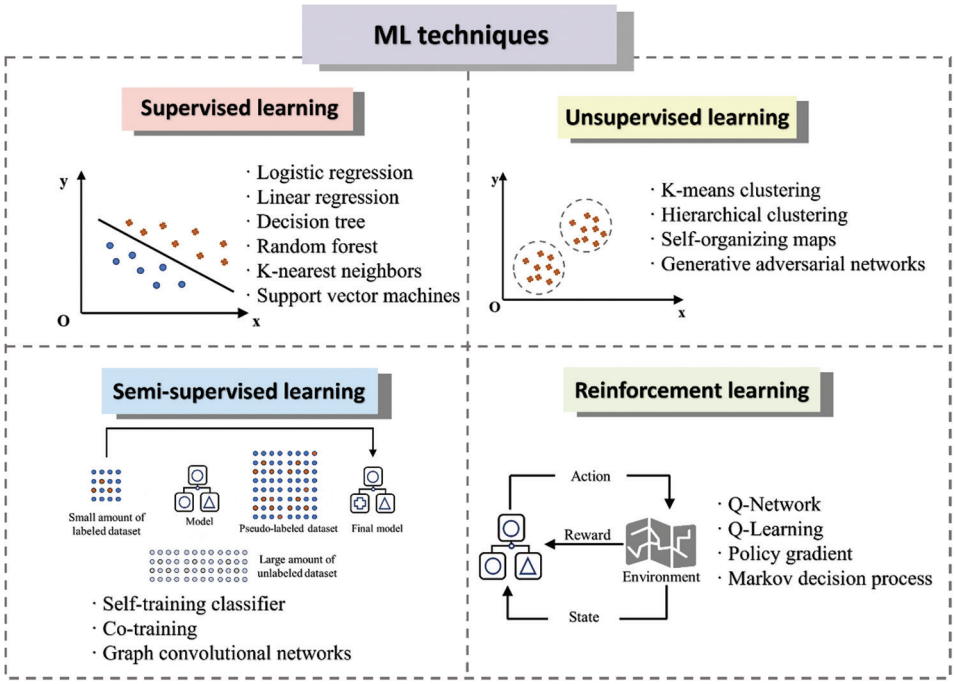

Figure 2. Four categories of machine learning and common algorithms. Image created by the authors.

similar characteristics, without the explicit definition of the nature of these groups. Common algorithms include K-means, hierarchical clustering, generative adversarial networks, and self-organizing maps (SOMs). Dimension reduction algorithms reduce data dimensions to enhance visualization and processing efficiency while preserving key features and lowering complexity. These algorithms play a crucial role in handling high-dimensional datasets, particularly in image processing tasks.

(iii) Semi-supervised learning: Semi-supervised learning algorithms are positioned as an intermediate model between supervised and unsupervised learning approaches. This methodology employs the use of pseudo-labels or a limited amount of labeled data in conjunction with a substantial volume of unlabeled data for the purpose of performing data classification and achieving predictive outcomes. Key algorithms include self-training classifier and graph convolutional networks. This learning approach is particularly valuable when labeled data acquisition is costly but unlabeled data are relatively accessible.

(iv) Reinforcement learning: Reinforcement learning represents one of the more complex ML models. It employs a trial-and-error approach to seek optimal solutions within specific domains, learning through positive reinforcement signals generated by its environment. Typical algorithms include Q-learning, deep Q-network, policy gradient, and Markov decision process. The field of reinforcement learning has demonstrated significant potential in domains such as robot control and resource scheduling.

Model evaluation must be conducted on data independent from the training set to avoid overfitting or underfitting. Common evaluation methods include k-fold cross-validation. Evaluation metrics are selected based on task type: regression problems commonly use root mean square error (RMSE), mean absolute error (MAE), and coefficient of determination (R^2); classification problems employ accuracy, recall, and F1 score; and clustering problems may utilize metrics like the Landis index. Evaluation results can further optimize model hyperparameters to achieve optimal performance.[51,52]

1.3. ML-driven AM of biomedical metals

AM offers freedom for the personalization of biomedical metals, while the highly nonlinear and dynamically uncertain process poses significant challenges in achieving precise control over process-structure-property relationships. The challenges manifest across three aspects: (i) forward prediction of properties difficulties: the intricate relationship between process parameters and final properties defies description through simple models; (ii) inverse optimization of process parameters inefficiencies: global optimization and multi-objective trade-off inefficiencies in high-dimensional parameter space; and (iii) quality control challenges: insufficient real-time diagnostic and intervention capabilities for identifying and addressing defects during the manufacturing process. It is within this context that ML emerges as a transformative tool, capable of uncovering hidden patterns from historical data, simulations, and real-time process monitoring. This data-driven approach enables the construction of precise predictive models and efficient optimization strategies, thereby addressing the core bottlenecks in AM.

Although existing reviews have improved our understanding of biomedical metals and ML applications in AM, the research in this specific subfield is not integrated. For instance, Bahl *et al.*[53] systematically reviewed the design, thermo-mechanical processing, and performance evaluation of metastable β titanium alloys for biomedical applications. Li *et al.*[54] reviewed the effects of various surface morphologies on the *in vitro* and *in vivo* performance of biomedical metallic materials, while delving into the underlying mechanisms linking surface topography to biological responses. Wang *et al.*[55] reviewed the research progress on Mg-based alloys as biomedical materials, with a particular focus on strategies for optimizing their mechanical properties and corrosion behavior. Existing reviews on biomedical metallic materials seldom incorporate ML methodologies; they are more frequently mentioned as future perspectives in the outlook section, such as Guo *et al.*[56] specifically highlighted the prospects of ML in accelerating intelligent design, printing processes, and performance prediction of powder-based three-dimensional (3D) printed titanium alloys providing new insights for future research. For the field of ML-driven alloy design, Li *et al.*[57] outlined the use of ML in multi-property optimization of high-entropy alloys, while Hu *et al.*[58] summarized ML's role in establishing composition-processing-property linkages and enabling inverse design. For ML in AM, Jin *et al.*[59] elaborated on the specific applications of ML across different AM processes and the construction of digital twins, and Zhu *et al.*[60] reviewed ML applications in condition monitoring and defect diagnosis for metal AM. Further expanding on the applications of ML in AM, Chen *et al.*[61] reviewed the application of ML in AM from design and process optimization to *in situ* defect detection and post-process quality assessment and highlighted the innovative integration of emerging ML techniques, such as reinforcement learning and physics-informed

ML, for enhancing quality assurance and advancing intelligent manufacturing in AM. Inayathullah *et al.*[62] focused on physics-aware hybrid data approaches and evaluated the performance of various advanced ML algorithms in enhancing the precision and efficiency of AM. This review, therefore, narrows its scope to the specific domain of ML applications in AM process of biomedical metals.

This review is organized around three interconnected dimensions that form a manufacturing framework (Figure 3): (i) building forward predictability: in response to the stringent requirements of medical metals for mechanical compatibility, biocompatibility, and service reliability, ML establishes surrogate models between process parameters and key performance indicators, laying the foundation for understanding complex process-structure-property relationships and enabling function-oriented manufacturing; (ii) enhancing process inverse optimization efficiency: confronted with the inefficiency of traditional trial-and-error methods in navigating high-dimensional parameter spaces, ML-driven optimization algorithms synergize exploration and exploitation to identify optimal performance parameters or comprehensively balanced process windows, thereby enhancing development and research efficiency; and (iii) upgrade of process controllability: by leveraging multi-source *in situ* monitoring data, ML enables real-time defect diagnosis during the manufacturing process. This facilitates a shift in quality control strategy from post-fabrication inspection to in-process control and prior prediction, providing crucial support for the clinical translation and standardization of additively manufactured biomedical metals.

2. ML-driven forward prediction of AM biomedical metals

2.1. Overview

Forward prediction in AM refers to the use of ML models to forecast the performance metrics of final products based on known process parameters, material composition, or initial conditions.[58] This approach follows the process-structure–property paradigm, aiming to construct high-precision and efficient surrogate models that map manufacturing inputs to functional outputs. Traditional methods, which rely heavily on experimental iteration and physics-based or empirical formulas, often encounter limitations due to the high-dimensional and strongly non-linear coupling effects within the parameter space. In contrast, ML-driven forward prediction serves as a powerful surrogate model capable of automatically extracting complex nonlinear mappings from large volumes of high-dimensional process data. This effectively overcomes difficulties arising from unclear underlying mechanisms and provides a reliable foundation for subsequent inverse optimization aimed at determining process parameters from target properties.

For biomedical metals, the successful application critically depends on mechanical compatibility, biocompatibility, and long-term service reliability.[63] Accurately predicting the final performance of AM-fabricated biomedical components is essential to achieving right-first-time manufacturing and accelerating clinical translation. Key aspects requiring prediction include macrostructure quality, microstructure, mechanical properties, fatigue life, and defects, all of which collectively determine implant performance in complex biological

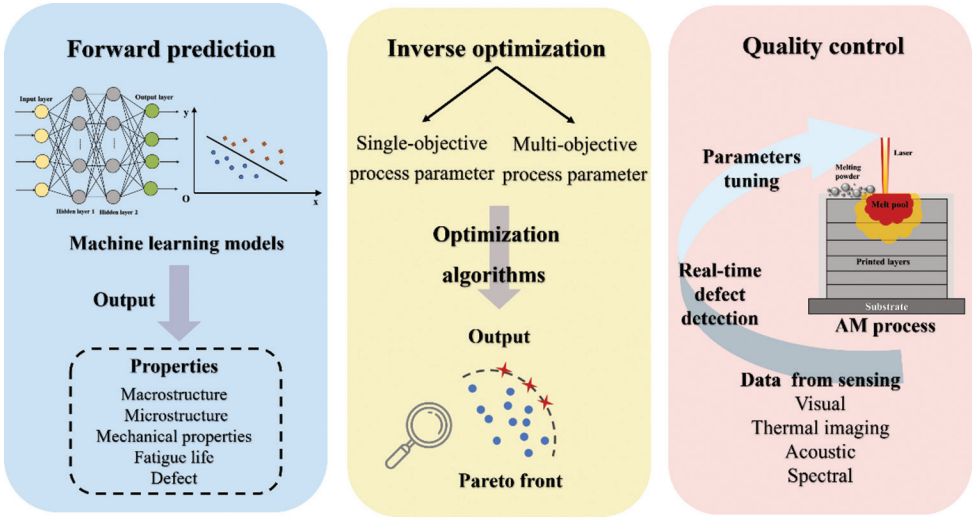

Figure 3. Overall framework of the review: machine learning–driven additive manufacturing of biomedical metals, including forward prediction, inverse optimization, and quality control. Image created by the authors.

environments.[39] This chapter elaborates on the application of ML in the forward prediction of these attributes for AM-fabricated biomedical metals, demonstrating how data-driven modeling supports performance forecasting.

2.2. Macrostructure quality forward prediction

In additively manufactured biomedical metal, the macrostructure quality of parts forms the foundation for their successful application. Among these, density and surface roughness are the two most critical macrostructure quality indicators. ML models enable precise forward prediction of these indicators by learning correlations between process parameters and macrostructural properties.

2.2.1. Density

Density serves as a core metric for assessing internal defects in additively manufactured parts. High density is essential for ensuring the superior mechanical properties and long-term service safety of biomedical metals.[64] Early studies such as Bartolomeu *et al.*[65] employed traditional statistical models like response surface methodology. These successfully established quantitative relationships between LB-PBF process parameters and density for Ti-6Al-4V, revealing the significance of parameter interactions and demonstrating preliminary validation of the feasibility of establishing quantitative process-density mapping through data-driven methods.

As datasets expand and algorithms advance, more sophisticated ML models demonstrate superior predictive performance. ML models, utilizing process parameters as inputs, can accurately predict the relative density of final parts, thereby enabling the avoidance of high-porosity process windows before manufacturing. For instance, Maitra *et al.*[66] constructed comprehensive Ti-6Al-4V LB-PBF data set from 48 publications, employing GPR models to predict densification behavior. The GPR model achieved a remarkably low MAE of 1.12%, and its outstanding engineering applicability was validated through actual printing tests (MAE = 0.27%). In another study by Jiang *et al.*,[67] a dataset comprising 63 parameter trials was constructed with the aim of improving the density and mechanical properties of the high-entropy alloy $Ti_{1.5}Nb_1Ta_{0.5}Zr_1Mo_{0.5}$ (TNTZM), a preferred clinical alloy, during the LB-PBF process. Using laser power and scanning speed as inputs, the AdaBoost model achieved the best performance on the test set (R^2 = 0.85, RMSE = 0.37). This approach successfully produced TNTZM samples with a density of 99.9%. Subsequent heat treatment increased the yield strength by over 150 MPa while maintaining approximately 50% ductility, validating the predictive accuracy of ML model.

The universality of this data-driven approach was further validated across diverse material systems. Gor *et al.*[68] conducted a systematic comparison of multiple models for predicting the density of 316L stainless steel, with artificial neural networks (ANN) and SVM demonstrating superior performance, achieving R^2 values of 0.95 and 0.92, respectively, for density prediction (Figure 4A and B). Collectively, these studies demonstrate that diverse ML models can achieve high predictive accuracy for densification behavior in LB-PBF. By establishing precise quantitative links between process parameters and relative density, these data-driven approaches offer a reliable strategy to avoid high-porosity process conditions, thereby enabling the direct fabrication of highly dense parts.

2.2.2. Surface roughness

Surface roughness is a critical factor determining product quality. In the engineering field, excessive surface roughness not only directly leads to a shortened product lifespan but also significantly impairs mechanical properties such as tensile strength and fatigue strength. This degradation of macrostructure properties is closely related to adverse effects on the material's microstructure.[69,70] For biomedical metals, surface roughness directly regulates biocompatibility, influencing cell adhesion, proliferation, differentiation (osseointegration), and antibacterial performance.[71,72] However, excessively high roughness can also become an initiation site for fatigue cracks, posing a threat to long-term service safety. Given the complex and critical multi-dimensional impact of surface roughness on product performance, its stringent control is essential.

Consequently, various ML models have been developed to predict surface roughness for different AM processes, aiming to achieve proactive control. Koo *et al.*[73] employed random forest regression, extreme gradient boosting (XGBoost), and SVR models to predict the down-skin surface roughness in LB-PBF. The input features included laser power, scanning speed, layer thickness, hatching distance, and overhang angle. Among these models, the XGBoost model demonstrated the best performance (R^2 = 0.63). For wire arc AM (WAAM), which typically involves larger thermal input and a more unstable process, different approaches have been explored. Xia *et al.*[74] utilized a genetic algorithm-optimized adaptive neuro-fuzzy inference system (GA-ANFIS) model to predict surface roughness. This GA-ANFIS model achieved a very high prediction accuracy (R^2 = 0.94), which was verified to be highly consistent with actual measurements through a laser vision scanning system. This indicates that the GA-ANFIS model, combining the interpretability of fuzzy logic and powerful non-linear fitting capability, can

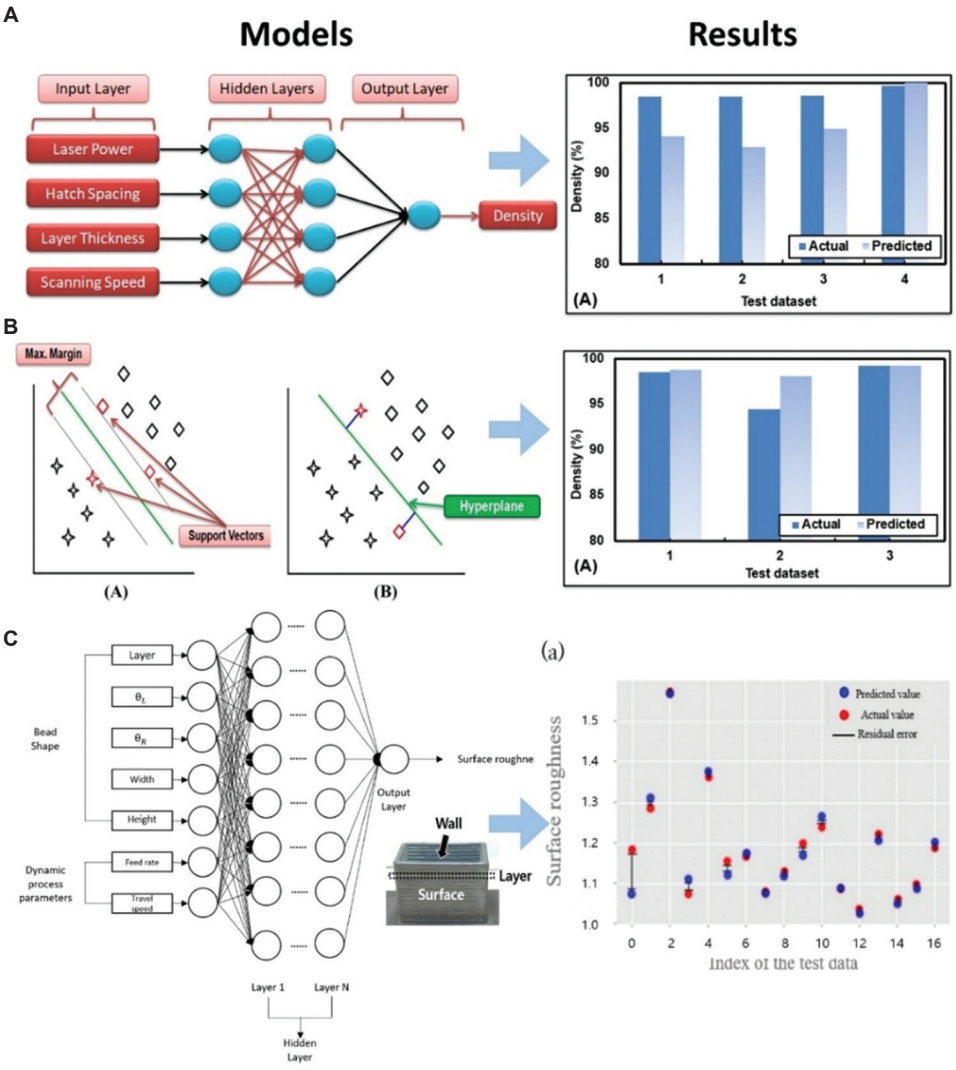

Figure 4. Models and results for macrostructure quality prediction. (A) Artificial neural network model for density prediction;[68] (B) support vector machine model for density prediction;[68] and (C) deep neural network model for surface roughness prediction.[75]

effectively predict and control macro-topography even in the challenging WAAM process. Similarly, So *et al.*[75] used a deep neural network (DNN) to predict the surface roughness between consecutively stacked layers in the WAAM process (Figure 4C). Wire feed speed, travel speed, and the geometric features of the previously deposited layer were utilized as inputs. The DNN model exhibited excellent performance on the test set, with an RMSE of 0.03 and a high correlation coefficient (r = 0.97) between predicted and actual values, demonstrating strong predictive capability. Surface roughness prediction through ML models, ranging from ensemble methods such as XGBoost to hybrid systems like GA-ANFIS and deep learning approaches like DNN, has shown considerable promise across different AM technologies, including LB-PBF and WAAM. These data-driven prediction methods provide an effective pathway for the precise control and optimization of surface roughness, thereby forming a crucial foundation for enhancing overall product quality and reliability.

2.3. Microstructure forward prediction

Microstructure serves as the critical bridge linking AM process parameters to macrostructure properties.[76] Factors such as grain size, morphology, and phase composition directly influence a material's mechanical and bio-functional properties.[77] However, compared with conventional manufacturing methodologies, the inherently intricate kinetics of AM processes can significantly alter the solidification behavior and grain structure of alloys during fabrication. Therefore, accurately predicting microstructure is central to achieving customized performance in biomedical metals.

Regarding phase composition and morphology prediction, Zhang *et al.*[78] synthesized 144 sets of Ti–xAl–yV alloy samples through DED and utilized a backpropagation neural network to establish a mapping from composition to microstructure and mechanical properties. The models successfully predicted the volume fraction of α-phase and the average width of α-laths, achieving high prediction accuracy with R^2 values exceeding 0.96. This direct composition–microstructure mapping provides a powerful high-throughput screening tool for rapidly designing novel biomedical titanium alloys with tailored microstructures, such as low-modulus β-Ti alloys. Furthermore, unsupervised deep learning has revolutionized microstructure characterization. Calvat *et al.*[79] employed variational autoencoders for low-dimensional feature extraction from raw electron backscatter diffraction Kikuchi diffraction patterns (Figure 5A and B), successfully revealing microstructural heterogeneities such as dislocation cell structures and intra-grain orientation gradients in AM Inconel 718. Although the research focused on high-temperature alloys, its methodology offers a novel perspective for quantifying and regulating microstructural heterogeneity in biomedical metals. ML has shifted from describing known microstructures to discovering unknown ones. It can predict classical phase compositions and grain sizes while extracting hidden microstructural features from massive datasets that remain inaccessible to traditional methods. By establishing links between process parameters and these quantified features, processes may be directed to refine grains and suppress detrimental phases, thereby optimizing the overall performance of biomedical metals.

2.4. Mechanical property forward prediction

Biomedical metals, particularly those used for implants, endure complex mechanical environments within the human body while fulfilling their biological functions. Mechanical property adaptation is a fundamental requirement for biomedical metals, particularly for load-bearing implants where modulus matching with bone tissue is crucial to prevent stress shielding. ML surrogate models enable predictive mechanical property design by establishing direct correlations between process parameters, heat treatment conditions, and resulting mechanical performance.

In a study on DED titanium alloys, Chi *et al.*[80] employed an XGBoost model to establish relationships between process parameters, utilizing laser power, scanning rate, and heat treatment conditions as inputs to accurately predict the ultimate tensile strength (UTS) and elongation of the material. Ti-17 alloy specimens fabricated under the guidance of the model exhibited mechanical properties in close agreement with the predicted values, achieving a UTS of 1050 MPa and an elongation of 12.5%. Considering the multifactorial effects of process–heat treatment–microstructure interactions, Wang *et al.*[81] demonstrated the advantages of multi-scale modeling. Employing a multilayer perceptron, they found that incorporating heat treatment–induced microstructural features significantly improved the prediction accuracy of Ti-6Al-4V tensile strength, with the R^2 increasing from 0.80 to 0.91. This indicates that incorporating microstructure as an intermediate variable enhances both the physical plausibility and accuracy of mechanical property predictions. Liu *et al.*[82] developed an ML-based knowledge transfer framework to accelerate process optimization for new metal AM systems. Focusing on LB-PBF of Ti-6Al-4V, the study employed a naïve Bayes classifier to model process-property relationships. The model used process parameters as inputs to predict discretized levels of relative density and microhardness as outputs. The predictive performance was robust, achieving accuracies of 85.6% for density classification and 88% for microhardness classification, with area under the curve values of 0.88 and 0.93, respectively. Experimental validation confirmed that the model could successfully recommend process parameters for new printer models not included in the training data, effectively demonstrating

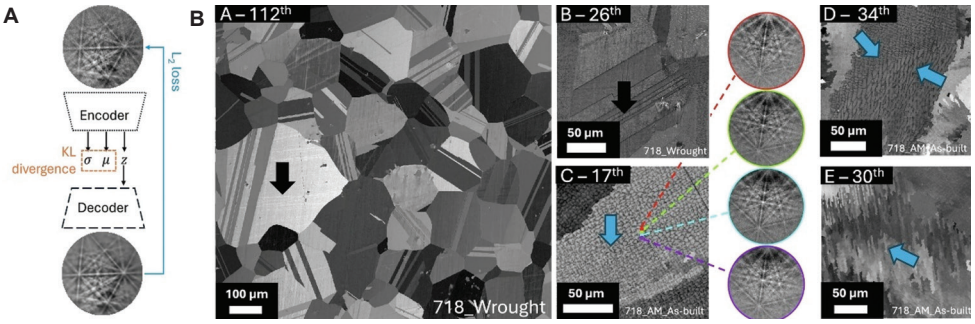

Figure 5. Microstructure characterization of additively manufactured metals by machine learning. (A) Variational autoencoder training principle and (B) latent space feature maps for microstructure heterogeneity identification. Image reprinted with permission from Calvat *et al.*[79] Copyright © 2025 The Authors.

cross-printer knowledge transfer across three industrial scenarios and significantly reducing the experimental burden for process qualification. In addition, Fang *et al.*,[83] as illustrated in Figure 6, integrated a validated thermal model with a 1D convolutional neural network (CNN) to analyze thermal history data, accurately predicting the mechanical properties, specifically the UTS, yield stress, and failure stress of DED Inconel 718 thin walls and demonstrating high predictive accuracy for UTS with a test set R^2 of 0.67. The thermal history-performance prediction framework established in this study is equally applicable to forecasting performance changes in biomedical metals during AM caused by complex thermal cycling. For the elastic modulus which is critical to biomedical implants, Liu *et al.*[84] developed a Young's modulus prediction model for Ti-6Al-4V based on an ANFIS. This model achieved a prediction error of only 0.66 GPa, far outperforming traditional theoretical models, and effectively quantified microstructure effects, providing a reliable foundation for precision control of implant modulus.

With the increasing application of ML models in AM of biomedical metals, model interpretability has become crucial for ensuring prediction reliability and guiding process optimization. Shapley additive explanations (SHAP) analysis, one of the most widely used interpretability methods,[85] quantifies the contribution of each input feature to model predictions, thereby revealing the influence mechanisms of process parameters on strength and ductility. As shown in Figure 7, the MechProNet framework developed by Akbari *et al.*[86] integrated 1600 data points and employed models such as random forest to achieve high-precision predictions ($R^2 > 0.90$) for yield strength, tensile strength, and other properties. Concurrently, SHAP analysis systematically examined the influence of multiple AM factors on mechanical properties such as yield strength and UTS (Figure 8). The analysis indicated that post-processing conditions are the most significant factor affecting yield strength, followed by material thermophysical properties, processing parameters, and the material itself.

SHAP analysis serves a dual purpose: it quantifies the importance of influencing factors and reveals the direction of their effects on mechanical properties. This enhances the transparency of ML models and validates the consistency between predictions and underlying physical mechanisms. Such interpretability not only improves model trustworthiness but also provides new insights into understanding complex process–structure–property relationships in AM. By clarifying the influence mechanisms of key process parameters, it effectively guides the process development of novel biomedical alloys, reduces trial-and-error costs, and accelerates clinical translation.

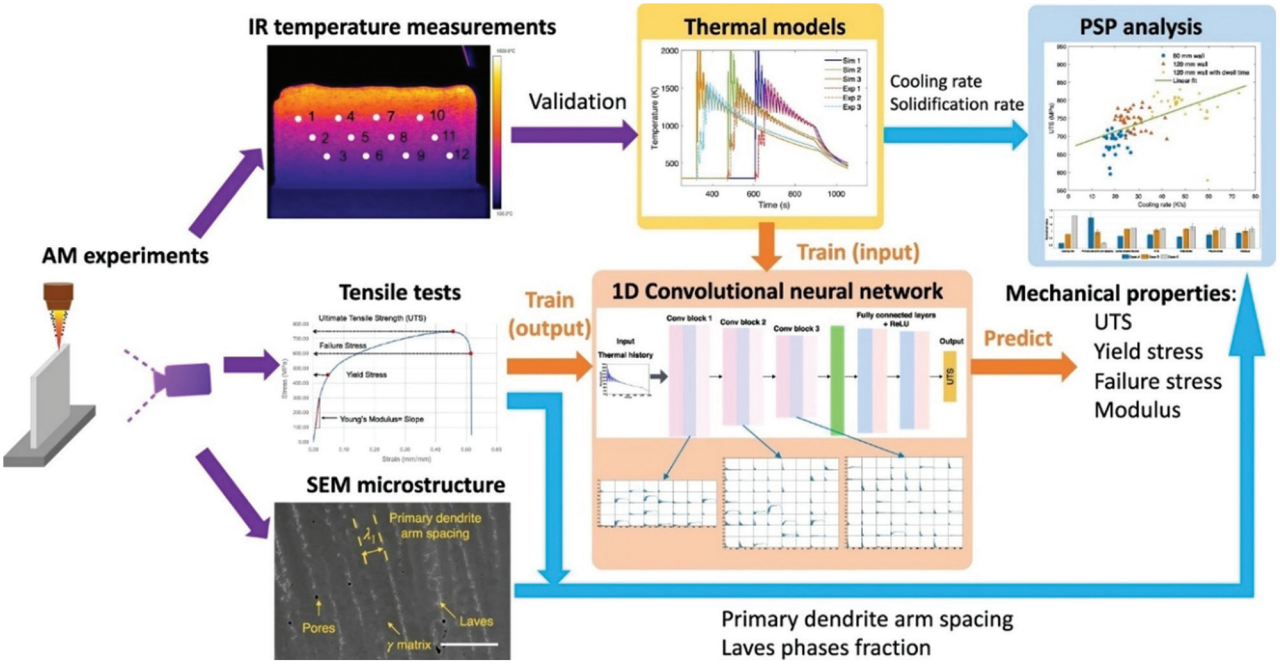

Figure 6. Prediction and characterization of additively manufactured metals by machine learning. Variational autoencoder training principle and latent space feature maps for microstructure heterogeneity identification.[83]
Abbreviations: AM: Additive manufacturing; IR: Infrared; PSP: Process-structure-properties; SEM: Scanning electron microscopy; UTS: Ultimate tensile strength.

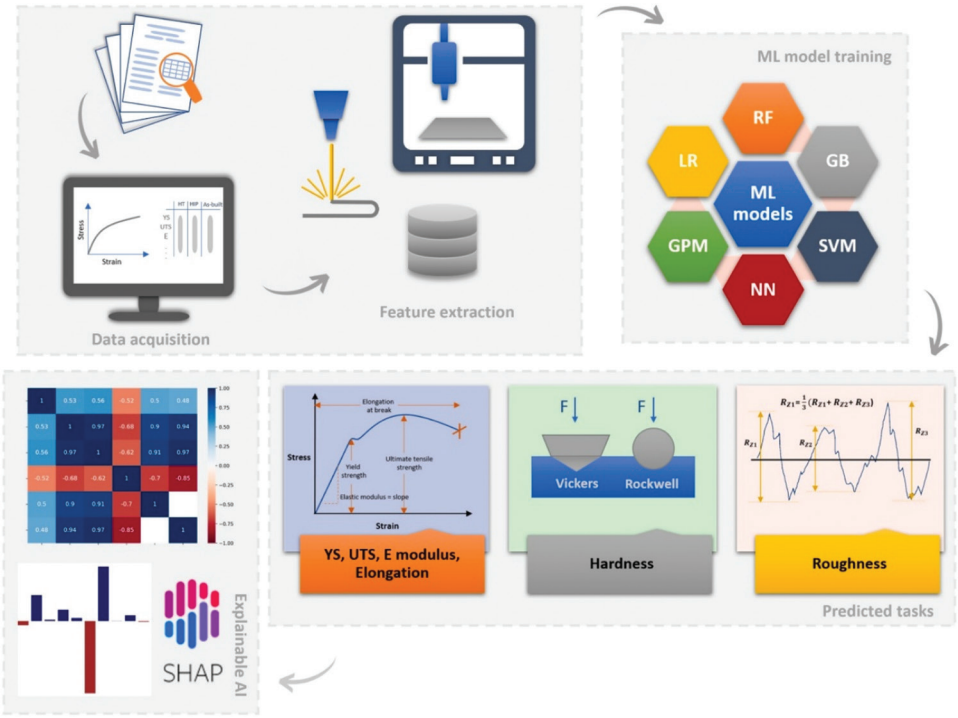

Figure 7. Workflow utilized to predict mechanical properties, including data collection, feature extraction, machine learning model training, predictive tasks, and model analysis.[86]
Abbreviations: AI: Artificial intelligence; E modulus: Elastic modulus; GB: Gradient boosting; GPM: Gaussian process model; LR: Linear regression; NN: Neural network; RF: Random forest; SHAP: Shapley additive explanations; SVM: Support vector machine; UTS: Ultimate tensile strength; YS: Yield strength.

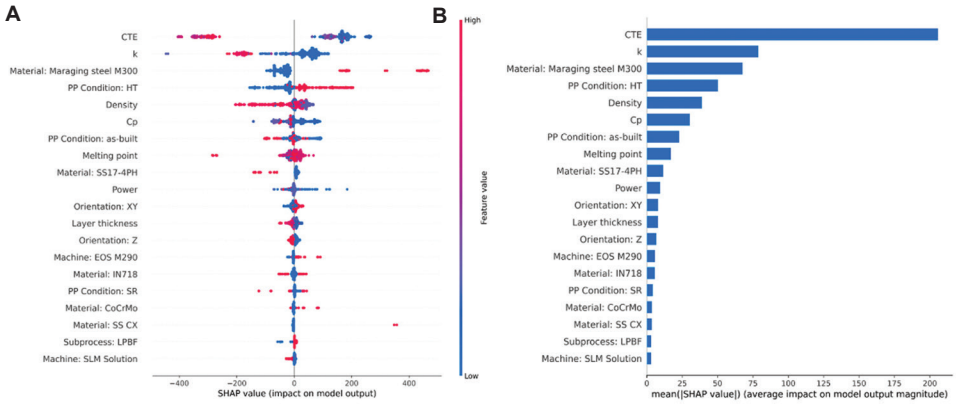

Figure 8. Swarm plot (A) and mean SHAP plot (B) for the XGBoost model predicting yield strength.[86]
Abbreviations: SHAP: Shapley additive explanations; XGBoost: Extreme gradient boosting.

2.5. Fatigue life forward prediction

Fatigue is also a predominant cause of metal failure, particularly for biomedical metallic materials serving in environments under cyclic loading.[87,88] Consequently, accurate prediction of fatigue life is crucial for ensuring the long-term safety and reliability of implants. In recent years, hybrid approaches integrating physical models with data-driven methods have emerged as a promising pathway to enhance prediction accuracy. For instance, Zhan *et al.*[89] developed a hybrid framework combining continuum damage mechanics with a random forest model. Using the stress concentration factor, maximum stress, and stress ratio as inputs, the model effectively predicted the fatigue life of additively manufactured titanium alloy, demonstrating significantly higher accuracy than pure physical models. This method proves particularly suitable

for predicting the fatigue behavior of actual components with geometrical features, highlighting its substantial practical engineering value. Regarding direct prediction based on process parameters, Zhang *et al.*[90] constructed an ANFIS model for LB-PBF 316L stainless steel. The model successfully predicted high-cycle fatigue life using process parameters and post-processing parameters in conjunction with the maximum cyclic stress, maintaining prediction errors within an acceptable range. Similarly, Shen *et al.*[91] employed feature engineering to optimize a multilayer perceptron model for Ti-6Al-4V alloy. By incorporating defect characteristics obtained from micro-CT scans, they established a high-precision fatigue life prediction model and explicitly identified defect location as the most critical factor influencing life. Evidently, the ML prediction of fatigue life is evolving from a reliance solely on process parameters toward an integrated framework that incorporates mechanical loading conditions with key defect characteristics such as size, shape, and location.

2.6. Defect forward prediction

Common defects in AM, such as porosity, lack of fusion, and cracks (Figure 9), are key risk sources that compromise the reliability of metals[92,93] and can lead to clinical failure. These defects not only act as stress concentration sites, significantly reducing the fatigue strength and fracture toughness of the material, but in biodegradable metals, they may also accelerate localized corrosion, leading to premature mechanical degradation or the release of unintended metal ions. Therefore, proactively predicting and avoiding defects before production is a critical task for ensuring product quality. In this context, ML, particularly its important subfield, has demonstrated significant potential in key tasks such as defect identification, classification, and generation.

In the diagnosis and prediction of defect types, Lee *et al.*[94] established an explainable ML framework for the laser metal deposition process. The study used GPR to predict porosity and geometric dimensions, and an SVM to classify defect types (*e.g.*, gas pores, keyholes, and lack of fusion), achieving an overall accuracy exceeding 0.93. Through SHAP analysis, the influence weight of various process parameters on defect formation was systematically quantified. Results indicated that the powder feeding rate had the greatest impact on the deposited height, while laser power was the most critical factor controlling porosity. Similarly, Gui *et al.*[95] designed and fabricated 32 sets of S30C samples with different process parameters and conducted actual inspection and classification of internal defects using X-ray CT and SEM. By employing quantitative surface morphology parameters as defect detection criteria, an SVM model was utilized to predict defects based on process parameters (current, scanning speed, and line offset), achieving an accuracy of 0.95 and an F1 score of 0.73.

Furthermore, Du *et al.*[96] integrated purely data-driven methods with physical laws to reveal the underlying mechanisms of defect formation and establish high-precision prediction models. Addressing balling defects in

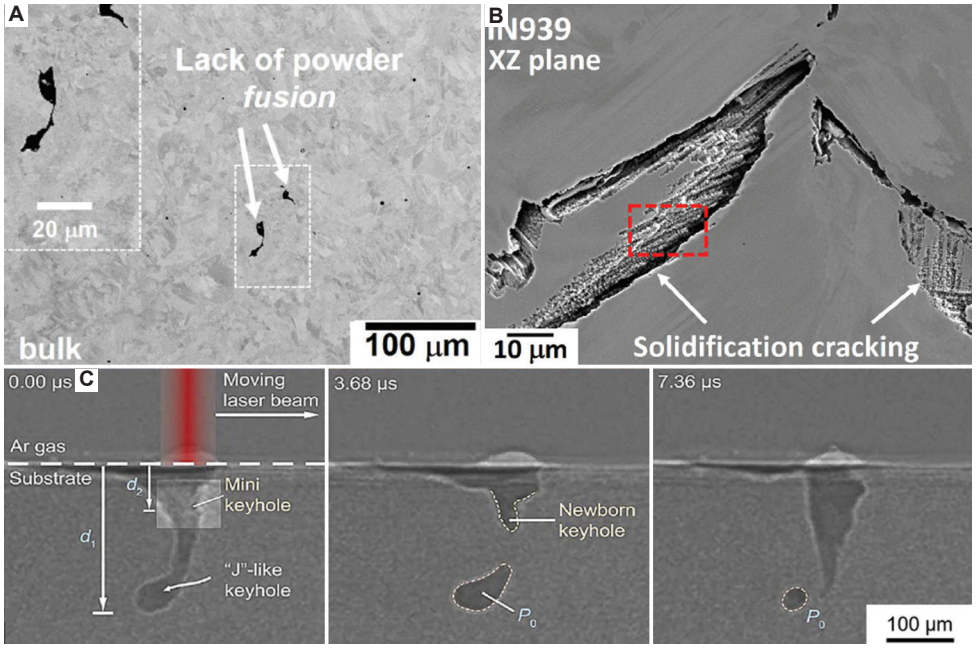

Figure 9. Common defects in additive manufacturing. (A) Lack of powder fusion; (B) Crack;[92] (C) Formation of keyhole.[93]

LB-PBF, instead of using process parameters directly, they utilized a validated 3D heat transfer and fluid dynamics model to compute six feature variables closely related to the balling formation mechanism, such as volumetric energy density, surface tension, and melt pool aspect ratio—as inputs for ML. Using a genetic algorithm, they constructed a balling susceptibility index prediction model, which achieved approximately 90% prediction accuracy tested against 166 experimental datasets, with its effectiveness further validated through LB-PBF experiments.

In defect prediction, the usage of ML is evolving from post-detection toward pre-hoc warning and virtual twins. By generating virtual microstructures consistent with real defect statistics and leveraging explainable models to clarify causal relationships between process parameters and defect types, ML paves a new path toward achieving comprehensive, forward-looking quality control throughout the entire biomedical metals AM process.

3. ML-driven inverse optimization of AM process

3.1. Overview

After achieving accurate prediction of the process-structure-property relationships, the core challenge in AM process research shifts from an analytical problem to an inverse problem of greater engineering value. In biomedical metallic AM, inverse optimization denotes ML-based algorithms searching within high-dimensional process parameter spaces to identify optimal parameter combinations or Pareto fronts. Its core output comprises either a set of process parameters meeting target performance criteria or a process window achieving multi-objective trade-offs, thereby bridging material design with applications.

Traditional optimization pathways face three major challenges: (i) high-dimensional complexity: the AM process involves numerous parameters, such as laser power, scanning speed, hatch spacing, layer thickness, and scanning strategy. These parameters interact in complex, non-linear, and coupled ways.[97] This high-dimensional parameter space makes optimization through traditional empirical methods or exhaustive search extremely difficult; (ii) cost and time constraints: full factorial design of experiments is a common method in traditional optimization, but the number of required experiments grows exponentially with the number of parameters. For specific metal AM alloys or systems, budget constraints make data-intensive methods difficult to generalize; and (iii) susceptibility to local optimum: traditional optimization methods based on single-point responses, such as one-factor-at-a-time or some local search algorithms, are prone to becoming trapped in local optima, failing to discover the global optimal process window.[98] This means potentially missing parameter combinations that could achieve higher performance or better overall benefits.

Against this backdrop, optimization frameworks driven by ML, by integrating performance prediction models with intelligent search algorithms,[99,100] enable precise and efficient mapping from the performance space back to the process parameter space, ultimately facilitating intelligent decision-making from performance requirements to process recipes.

3.2. Introduction to optimization algorithms

Within the inverse optimization framework, optimization algorithms search the process parameter space to identify combinations that achieve target performance metrics. Different algorithms, with their unique mechanisms, are suitable for different application scenarios.[101,102] For inverse optimizing a single key performance objective, algorithms strive to find the global optimum within the parameter space. Evolutionary algorithms such as genetic algorithm and particle swarm optimization (PSO), which simulate natural selection or collective behavior, perform global exploration in complex, non-linear spaces and can effectively avoid local optima, making them common choices for solving such problems.

However, optimization in AM is inherently a multi-objective optimization (MOO) problem. The core challenge of MOO lies in handling these conflicting objectives to find the best compromise solutions. The goal is no longer to obtain a single optimal solution, but to identify a set of non-dominated solutions known as the Pareto optimal set. These solutions collectively form the Pareto front, the set of all Pareto optimal points in the objective space, which clearly delineates the trade-off boundaries between different performance metrics beyond which no further improvement is possible without worsening another. Each solution on this front represents a specific performance trade-off scheme; no single objective can be further improved without degrading at least one other objective. This allows decision-makers to select the most suitable process parameter combination from this set based on specific clinical application requirements. As illustrated in the schematic by Hua *et al.*[103] (Figure 10), within a 3D objective space, both the search directions defined by uniform reference vectors (hollow circles in the figure) and the actual Pareto optimal solution set (solid points in the figure) are simultaneously presented.

Commonly used MOO algorithms include the following: (i) non-dominated sorting genetic algorithm II (NSGA-II): noted for its elitist strategy, fast non-dominated

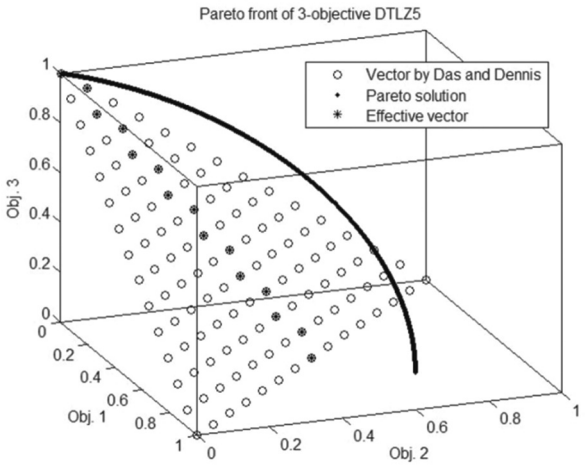

Figure 10. Illustration of Pareto front with 3-objective problem[103]

sorting, and crowding distance calculation mechanism, this algorithm can stably find a Pareto front with good convergence and high diversity, comprehensively revealing the trade-off relationships between performances. It is one of the most widely used algorithms in AM;[104,105] (ii) multi-objective PSO: known for its fast convergence speed, this algorithm guides the search direction by maintaining the personal best and global best positions. Although sometimes slightly inferior to NSGA-II in terms of the uniformity of the solution distribution, it is an efficient choice when computational resources are limited and rapid acquisition of approximate optimal process parameters is desired;[106] (iii) multi-objective accelerated process optimization (m-APO): an emerging efficient framework that significantly reduces the number of experiments required to find a satisfactory Pareto solution set by skillfully leveraging prior knowledge and an innovative space-filling search mechanism. It is particularly suitable for rapid process adaptation;[107] and (iv) multi-objective Bayesian optimization (MOBO): especially suitable for optimizing expensive-to-evaluate black-box functions.[95,100,108] When the performance prediction model itself is computationally expensive to train, or when the optimization process needs to be directly coupled with high-fidelity simulations, frameworks combining GPR with MOBO can inversely locate optimal process parameters with minimal evaluations by intelligently balancing exploration and exploitation, demonstrating high sample efficiency.[109,110]

3.3. Single-objective inverse optimization

When the design of biomedical metals has an extreme requirement for a single core performance indicator, such as load-bearing sites requiring extremely high fatigue life, or the need for precise control of elastic modulus to match bone modulus,[111] single-objective inverse optimization provides efficient solutions by identifying process parameters that achieve those targets. The core of the ML implementation path is to construct an inverse search framework driven by the performance target. This involves first training a high-accuracy forward surrogate model that maps process parameters to the target performance. Then, with the goal of making the model's predicted value as close as possible to the desired performance, optimization algorithms are used to perform a global search within the process parameter space, inversely deriving the optimal combination of process parameters.

Narayana *et al.*[112] explicitly aimed to determine the optimal process parameters for achieving extremely high density and a specific build height for Ti-6Al-4V in DED. By training an ANN as an accurate forward predictor and coupling it with an optimization algorithm for inverse search, they inversely solved for the optimal combination of laser power, scan speed, and other parameters that would meet these predefined geometric and density requirements. Similarly, the work of Nguyen *et al.*[113] focused on identifying the process parameter set that would achieve the target near-full density (>99.8%) in LB-PBF Ti-6Al-4V. Using a deep learning model to inversely explore the process parameter space, they determined the specific laser power, scanning strategy, and other parameters that would minimize pore formation while maintaining the desired density threshold. In scenarios aiming to maximize specific mechanical properties (such as surface hardness and tensile strength) of implants, ML can likewise circumvent the limitations of traditional experience. Gan *et al.*[114] employed a SOM to inversely identify the optimal process window corresponding to target microhardness values in DED nickel-based superalloys. Their approach mapped from desired hardness values back to the optimal powder feed rate and other process parameters that would achieve those targets (Figure 11A and B). This work demonstrates the potential of unsupervised learning techniques such as SOMs in identifying the process window for biomedical metal AM through reverse identification.

Furthermore, melt pool stability directly determines the microstructure and defect state of the fabricated part. Tapia *et al.*[115] developed a surrogate modeling framework based on GPR that could inversely guide the selection of LB-PBF process parameters of 316L stainless steel. Specifically, to achieve a stable and appropriately sized melt pool, the model could output the specific laser power and scanning speed combinations that would produce the desired thermal characteristics.

Single-objective inverse optimization still holds an important position in the AM of biomedical metals,

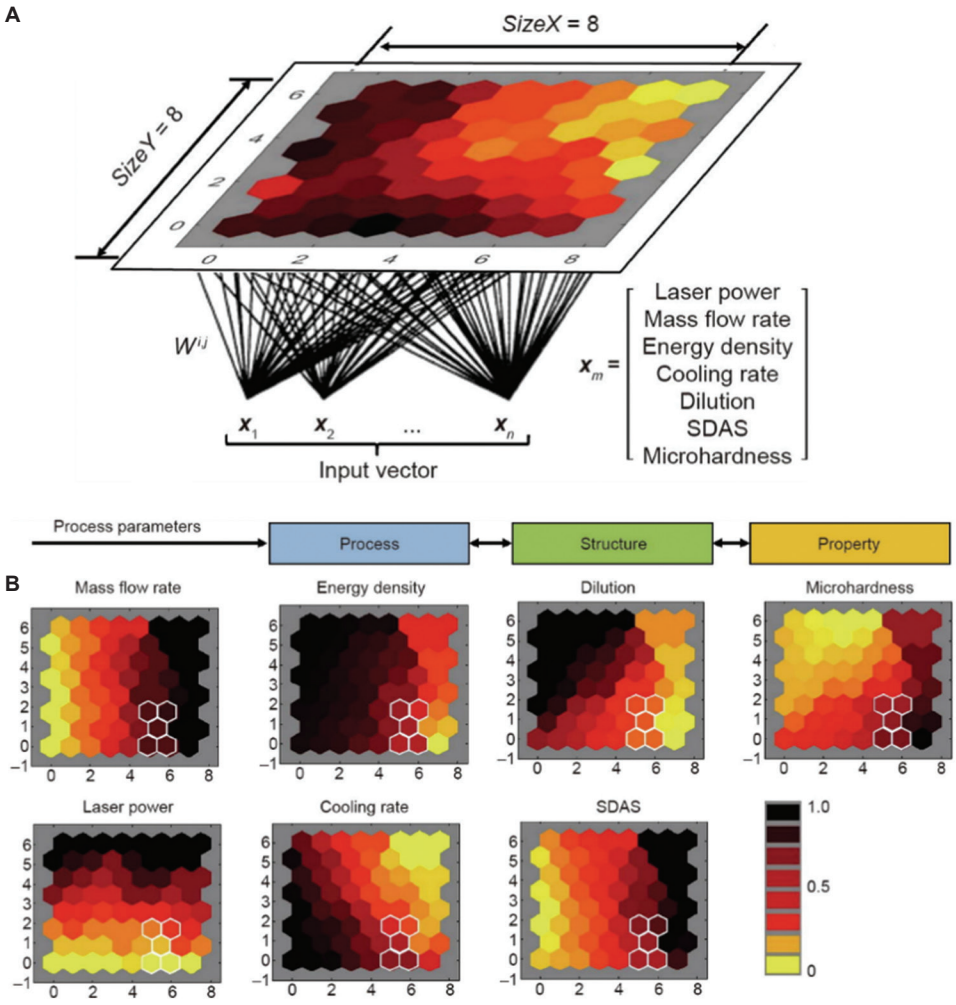

Figure 11. Machine learning–driven additive manufacturing process optimization for nickel-based high-temperature. (A) SOM including input vectors. (B) Identification of the optimal design window through contour plots of all design variables.[114]
Abbreviations: SDAS: Secondary dendrite arm spacing; SOM: Self-organizing map.

particularly in the customized development of implants for specific clinical application scenarios. When a single performance indicator becomes the key design constraint, focusing optimization on that specific target can ensure the implant's reliability and safety in that particular environment.

3.4. Multi-objective inverse optimization

The service performance of biomedical metals often requires the synergistic satisfaction of multiple performance indicators, which frequently exhibit trade-off relationships. For instance, increasing strength may sacrifice ductility, while reducing the elastic modulus may compromise fatigue performance due to the introduction of excessive porosity. MOO algorithms generate Pareto fronts, enabling selection of process parameters based on clinical needs.[116,117] ML-driven multi-objective inverse optimization identifies Pareto-optimal process parameter sets that achieve different balances of conflicting performance targets, and the workflow is illustrated in Figure 12.

Aboutaleb *et al.*[107] addressed the classic trade-off in Ti-6Al-4V mechanical properties by inversely identifying Pareto-optimal process parameter combinations that simultaneously maximized the elastic modulus and UTS. The m-APO framework outputs a set of Pareto-optimal process parameters, and compared to time-consuming full-factorial experimental designs, it reduces the computational cost by 51.8%, highlighting its significant value in rapid process development.

Beyond bulk materials properties, MOO methods are equally suitable for guiding the design of complex structures with specific functional requirements. Meng

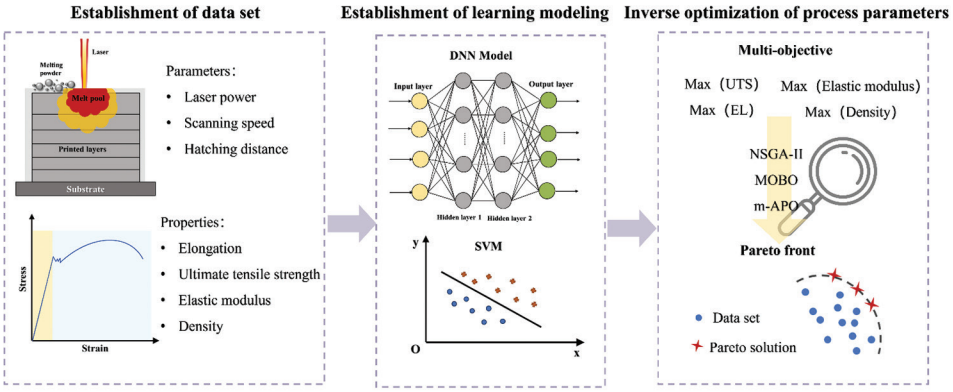

Figure 12. Workflow for machine learning-based multi-objective inverse optimization of process parameters. Image created by the authors. Abbreviations: DNN: Deep neural network; EL: Elongation; SVM: Support vector machine; UTS: Ultimate tensile strength.

et al.[118] used the NSGA-II to solve for the optimal LB-PBF process parameters that would simultaneously maximize energy absorption and minimize density in bio-inspired lattice structures. The inverse optimization approach determined the specific laser parameters and scanning strategies that achieved different compromises between these competing structural performance objectives.

Regarding the synergistic control of geometric accuracy, precise control over the deposition morphology is crucial when manufacturing customized biomedical metals with complex geometries. Cai *et al.*,[119] working with wire-laser DED, inversely derived optimal process parameter combinations that would simultaneously control the deposited layer height and width. They established a forward prediction model using SVR and coupled it with the NSGA-II algorithm for inverse MOO. They successfully inversely derived the optimal process parameter combinations that could synergistically meet these two-dimensional requirements from the desired geometries.

In the parameter inverse identification for coordinating density and controlled porosity, this represents a particularly classic contradiction in the biomedical field. Biomedical metals often require both high densities to ensure mechanical performance and specific surface or internal porosity to promote osseointegration. Heiss *et al.*,[120] during the LB-PBF manufacturing of biodegradable Zn alloy, innovatively used principal component analysis to reduce the dimensionality and quantify the multi-dimensional pore morphology characteristics, subsequently creating a clear process map. The map effectively inversely identified the process window capable of simultaneously achieving high bulk density and ideal pore morphology, successfully producing demonstrator parts that achieved a balance between mechanical performance and biological function.

With the deepening of the green manufacturing concept, process optimization is no longer limited to part performance. Peng *et al.*[121] aimed to identify pareto-optimal process parameters that would minimize specific energy consumption while maximize powder usage rate. They constructed predictive models from process parameters to these two economic/environmental indicator and used the NSGA-II algorithm for multi-objective inverse optimization. The inverse optimization framework solved for the laser power and scanning parameter combinations that achieved different trade-offs between economic and environmental performance indicators.

The principal value of multi-objective inverse optimization lies in its ability to transform process development from an experience-dependent trial-and-error approach into a precise, informed decision-making process grounded in systematic trade-offs. By analyzing the shape and distribution of the Pareto front, researchers can quantify the conflict level between different performance indicators. This clear trade-off landscape provides a critical foundation for final decision-making. In clinical applications, the optimal solution can be selected from a set of Pareto-optimal process parameter sets based on the specific implantation site and patient needs, thereby best addressing the immediate clinical priorities.

4. ML-driven quality control and monitoring

4.1. Overview

The AM technology, particularly for biomedical metals (*e.g.*, titanium alloys, cobalt-chromium alloys, and biodegradable magnesium alloys), has garnered significant attention due to its unique advantages in producing complex porous structures and enabling personalized customization. However, physical variability during manufacturing,

inconsistencies in powder materials, and resulting defects (such as porosity, lack of fusion, and cracks) remain major obstacles to its widespread industrial adoption. Traditional methods heavily rely on post-printing destructive testing or CT, which are not only costly and inefficient but, more critically, incapable of intervening in or repairing defects that arise during the manufacturing process.[122]

At present, ML technology is driving a fundamental paradigm shift in AM quality control. The core lies in integrating ML to fully leverage the vast data generated during manufacturing. This shifts quality control from a passive, post-inspection approach to a proactive, in-process prevention, and intervention model. It transitions from a passive, offline, sampling-based system to an active, online intelligent monitoring system. This reduces reliance on human expertise, enabling real-time quality monitoring, early defect alerts, and even autonomous process optimization.[123] The shift aims to make every biomedical metal printing process transparent, controllable, and reliable, thereby ensuring that products possess high reliability and batch-to-batch consistency.[124]

4.2. Sensing technology for AM monitoring

In the field of AM, the integrated application of multiple monitoring methods enables comprehensive perception of process states. Different sensor types capture information from distinct dimensions of the physical process, providing the basis for training and inference of ML models.[125]

Thermal imaging sensing: Typically, thermal cameras operate on line-scan or push-broom principle, where a single imaged line is optically dispersed onto a 2D sensor to simultaneously record one spatial and one spectral dimension, with full-field temperature mapping achieved through subsequent scanning of this line across the target (Figure 13A).[123,126-128] Thermal imaging cameras provide direct records of process thermal history by monitoring temperature field distributions across the molten pool and its heat affected zone. Temperature history and gradients serve as critical indicators for material phase transformations, residual stresses, and defect formation. Abnormal cooling rates or localized overheating can lead to undesirable phase changes and are also closely linked to defects such as porosity and hot cracks. Liu *et al.*[129] employed infrared thermal imaging cameras to capture real-time thermal image sequences during large-scale AM processes. By integrating a CNN long short-term memory model, they achieved temporal prediction of future temperature distributions, enabling early identification and early warning of abnormal temperatures.

Visual sensing: High speed cameras can capture the morphological dynamics of the molten pool with extremely high spatio-temporal resolution, including brightness, size, geometry, and fluctuations (Figure 13B). This visual information provides an intuitive basis for assessing molten pool stability.[130-133] The molten pool's dimensions, circularity, and fluctuations reflect energy input and melting conditions, serving as crucial precursors to forming instability and defect generation. Yang *et al.*[134] employed a high-speed camera sensing method to capture dynamic image sequences of the molten pool, spatter, and other phenomena. The key features of the molten pool under ultrasonic disturbance were extracted and reconstructed by integrating a fully connected layer with a convolutional autoencoder approach. Mi *et al.*[135] similarly employ the cameras to capture sequential images during the DED process. Further utilization of deep CNNs enabled precise segmentation of the molten pool contour and minute spatter particles, achieving an accuracy rate of 94.71%. Despite being susceptible to interference from intense light, visual sensing has become a vital tool for detecting surface defects and geometric deviations due to its advantages of being information-rich and highly real-time.

Acoustic and spectral sensing: Microphones or AE sensors can collect acoustic signals and stress waves generated during printing by plasma, spatter, material phase transitions, and even microcracks, thereby sensitively indicating the formation of internal defects[136-138] (Figure 13C). Rahman *et al.*[139] employed AE sensing combined with the K-means clustering algorithm to achieve continuous *in situ* monitoring of multi-layer deposition states during the WAAM process, verifying the consistency of acoustic signals in identifying process states under varying material and process conditions. Spectral sensors capture spectral information with high sensitivity and rich content. For instance, Montazeri *et al.*[140] employed a multispectral optical emission sensor, combined with Fourier transform imaging and maximum likelihood estimation, to achieve real-time monitoring of pore defects during the LB-PBF process.

Different sensors have distinct strengths (Table 2); for instance, acoustic and spectral sensors are more sensitive to internal defects such as porosity and cracks; thermal sensors precisely reflect energy input and thermal history; while visual sensors inherently excel at capturing surface defects and geometric deviations. Thus, multi-sensor data fusion has become an inevitable trend. Fusing multi-sensor data overcomes the limitations of single data sources by integrating heterogeneous data into high-dimensional feature vectors. This provides ML models with a more comprehensive and complementary information view, enabling more precise defect diagnosis.[141] Gaikwad *et al.*[142]

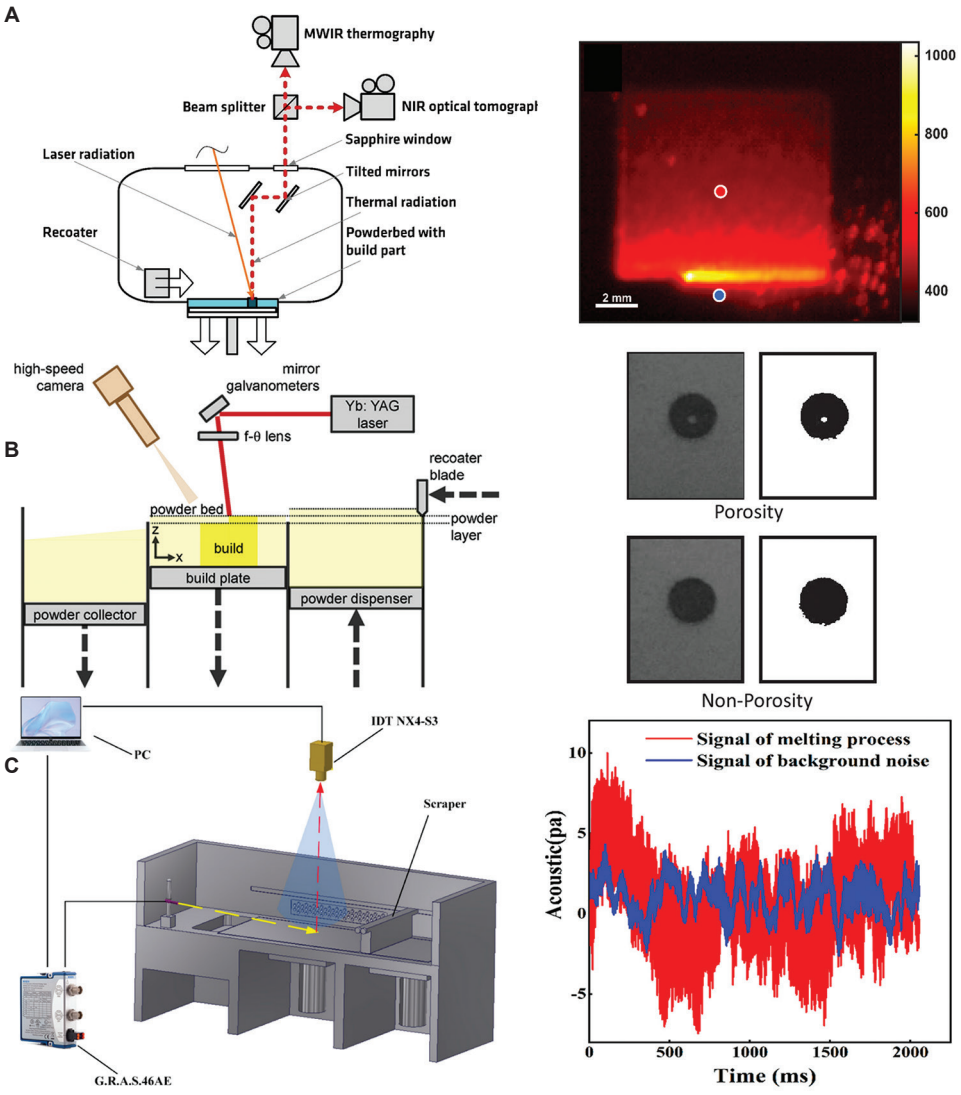

Figure 13. Sensing technologies for additive manufacturing monitoring. (A) LB-PBF machine with thermal imaging camera;[128] (B) LB-PBF machine with high-speed camera;[132] and (C) LB-PBF machine with microphone.[138]
Abbreviation: LB-PBF: Laser powder bed fusion.

Table 2. Sensor technologies and machine learning applications for online quality monitoring in additive manufacturing

Sensor type	Monitoring target	Data format	Advantages	Limitations
Visual sensor	Melt pool morphology, spatter, surface defects, geometric deviations	2D images/video sequences	Information-rich, intuitive, high spatio-temporal resolution	Susceptible to intense light/glare interference; large data volume
Thermal imaging sensors	Melt pool and heat-affected zone temperature field, cooling rate, thermal history	2D temperature field/ thermal images	Directly records process thermal history; correlates with energy input and phase transformations; sensitive to overheating	Accuracy affected by material emissivity; difficult to directly reflect internal defects
Acoustic sensors	Internal defects (porosity, cracks, micro-cracks), process stability	1D time-domain/ frequency-domain signals/ acoustic emission signals	Sensitive to internal defects, low cost, easy installation	Signals susceptible to environmental noise interference; feature extraction is relatively complex
Spectral sensors	Plasma plume, elemental characteristics, internal physical changes in molten pool	1D spectral sequence	Highly sensitive to internal physical changes in the molten pool; rich information content	Expensive equipment, specialized data analysis

fused heterogeneous sensor data from a co-axial pyrometer and a high-speed video camera and developed a sequential decision analysis neural network model to achieve accurate prediction and assessment of the geometric quality of single tracks in LB-PBF.

4.3. Application of ML methods in real-time defect detection

In the AM process, ML provides a powerful technical means for achieving *in situ* process monitoring and quality assessment by analyzing real-time multi-source sensor data. Based on the characteristics of data and challenges encountered in actual production, two primary technical approaches have emerged: precise identification and localization of known defects, and acute detection of unknown anomalies when labeled samples are scarce.

Supervised learning methods play a crucial role when common defect types in manufacturing processes, such as spatter, spheroidization, and poor powder distribution, are well understood and sufficient annotated data have been accumulated. For *in situ* quality monitoring of LB-PBF, Knaak *et al.*[143] developed a technique that marries high dynamic range optical imaging with CNN (Figure 14). This synergy provides high-spatial-resolution capabilities and facilitates layer-by-layer prediction of surface roughness, thereby enabling real-time quality assessment and process optimization. These models can learn defect features directly from image data, enabling the current state to be automatically classified. These models can learn defect features directly from image data, enabling the current state to be automatically classified. For instance, Scime *et al.*[144] addressed powder bed anomalies during the LB-PBF process by constructing a multi-scale CNN using an enhanced AlexNet architecture to automatically analyze grayscale images of the powder bed after powder spreading. This model autonomously learned and achieved high-precision recognition and classification of six types of powder bed anomalies, achieving an overall classification accuracy of 97% while pinpointing defects with pixel-level precision. Similarly, in the L-DED process, Chen *et al.*[145] developed a multi-sensor fusion digital twin framework based on supervised learning strategies. This model enables real-time identification and localization of known defect types such as cracks and critical-pore voids, subsequently generating a virtual quality map registered with the part's 3D volume, achieving a defect classification accuracy of 96%. It significantly outperforms single-sensor approaches, thereby demonstrating the effectiveness and robustness of supervised methods in multimodal fusion scenarios.

However, a more prevalent challenge in industrial settings lies in the diverse and unpredictable nature of anomalies, making it extremely costly or even impractical to obtain large quantities of labeled defect samples. Faced with this challenge, unsupervised or semi-supervised anomaly detection methods demonstrate unique value. Their core principle is not to directly identify specific defects, but

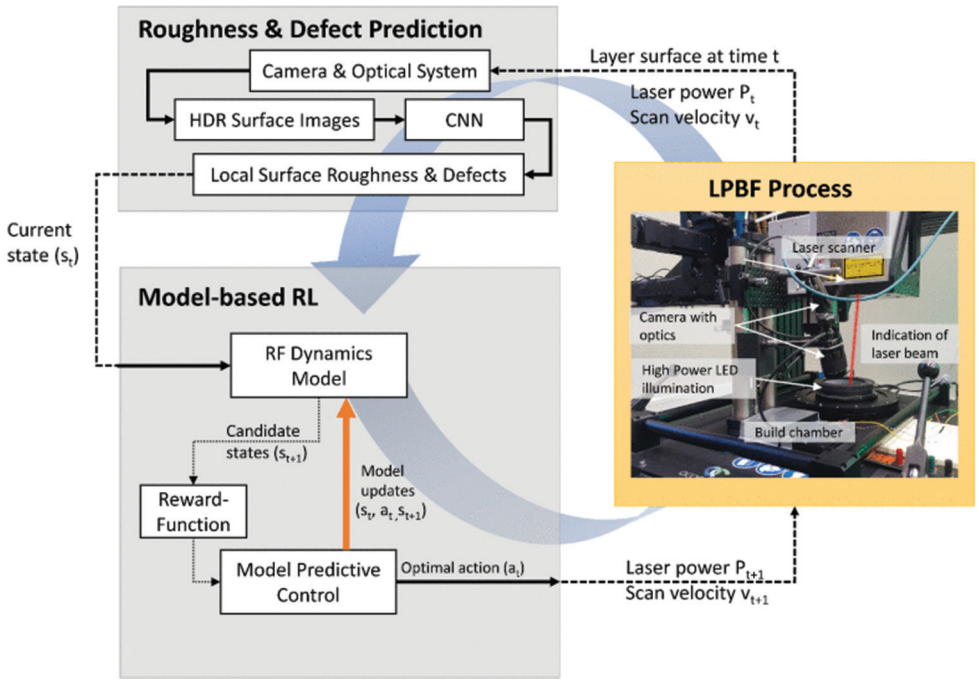

Figure 14. Framework for layer-wise monitoring and optimization of laser powder bed fusion processes.[143]
Abbreviations: CNN: Convolutional neural network; RF: Random forest; RL: Reinforcement learning; LPBF: Laser powder bed fusion.

rather to enable the model to learn and memorize the data patterns characteristic of qualified states through extensive normal process data. Once real-time sensor signals deviate significantly from this learned normal pattern, the system automatically triggers an anomaly alert. Models like autoencoders learn intrinsic patterns and distributions from large amounts of normal data, enabling them to identify anomalous signals deviating from these patterns.[146] Abranovic *et al.*[147] employed a convolutional long short-term memory autoencoder (ConvLSTM Autoencoder). Trained unsupervised using only video sequences of molten pools under normal operating conditions, the model quantified process stability through its ability to predict future frames. This approach successfully achieved online detection and localization of four typical defects without requiring any annotated defect data.

Therefore, ML-based real-time diagnosis lays the core foundation for achieving closed-loop control, transitioning from sensing to decision-making and execution.[148] The ultimate goal of an intelligent monitoring system is not merely to identify defects but also to dynamically intervene in the process parameters by integrating ML's decision-making capabilities with the actuators of the AM equipment, thereby proactively suppressing defect formation. This facilitates a fundamental shift in the quality control paradigm from post-inspection toward online prediction and adaptive manufacturing.

4.4. Closed-loop control and adaptive manufacturing

The ultimate objective of quality monitoring is to integrate the sensing and decision-making capabilities of ML with the actuators of AM to create an intelligent closed-loop control system.[149] The core mechanism operates as follows (Figure 15): when online sensor data indicates that the process is deviating from normal conditions, or when ML models predict impending defects, the system instantly generates commands to dynamically adjust process parameters (*e.g.*, laser power and scan speed), thus steering the process back on track and preventing defects.[150] Within such a closed-loop framework, ML plays an indispensable role: it enables accurate, real-time diagnosis, and prediction of process states and quality indicators by automatically extracting features from multi-sensor data and establishing high-dimensional, non-linear mappings.[151] This capability to create a quantitative, intelligent process-quality mapping provides the foundational insight necessary for precise parameter adjustments.

Effective parameter tuning is central to realizing such closed-loop control, and a variety of practical approaches have been developed. Gerdes *et al.*[123] predesigned and implemented a programmed feedforward control strategy involving an automatic increase in print speed at the midpoint of the print path. Armstrong *et al.*[152] employed 3D laser scanning between layers to detect geometric errors, thereby adjusting subsequent layer paths and parameters. Both of these methods are effective ways to improve the geometric accuracy and consistency of printed structures during the AM process.

The above-mentioned control models of parameter tuning establish the practical foundation for closed-loop control. To achieve higher level autonomous optimization, strategies such as model predictive control (MPC) are widely adopted. This approach utilizes dynamic models to predict future behavior and optimize parameter adjustment decisions. A core challenge in this field is obtaining accurate and efficient dynamic system models, with the technical approach evolving from traditional methods toward data-driven techniques. Early research relied primarily on system identification-based linear MPC. For example, Liu *et al.*[153]

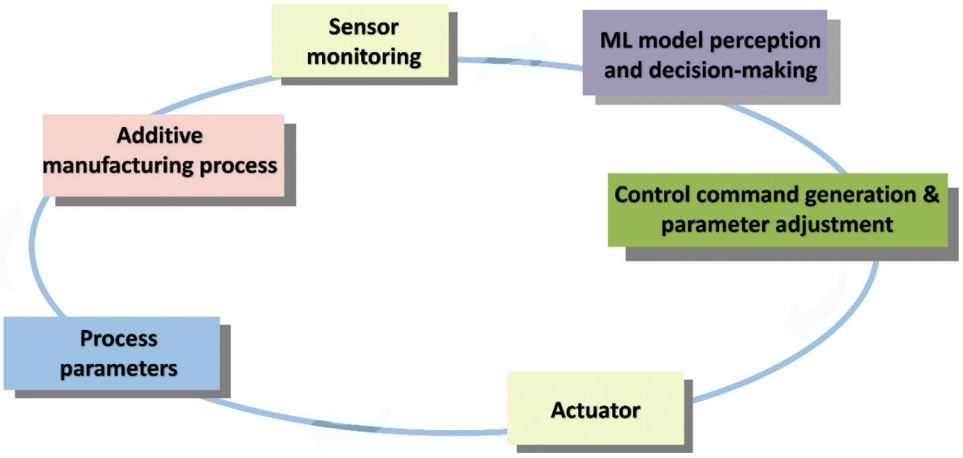

Figure 15. Schematic diagram of the intelligent closed-loop control system. Image created by the authors.
Abbreviation: ML: Machine learning.

controlled a laser metal deposition process by identifying a linear state-space model. Building on a simplified physical model of the melting pool, Cao *et al.*[154] proposed a control-oriented multi-input multi-output model and subsequently designed a tube-based robust multivariable MPC. In recent years, data-driven nonlinear MPC has emerged as a cutting-edge approach, significantly enhancing modeling and control capabilities for complex dynamics.

In the field of data-driven MPC, Chen *et al.*[155] proposed a digital twin framework based on time-series DNN and MPC. The study employed the time-series dense encoder as a surrogate model, enabling precise prediction of the entire future time domain for both molten pool temperature and depth. On this basis, MPC dynamically adjusts laser power to achieve precise temperature tracking while strictly constraining molten pool depth within the ideal dilution range of 10–30%. This approach has been shown to proactively suppress pore defect formation at its source. In comparison with conventional proportional-integral-derivative control methodologies, this framework not only demonstrates equivalent temperature tracking capability ($R^2 > 0.99$) but also generates smoother, less fluctuating laser power curves. It inherently handles multi-variable constraints, highlighting the immense potential of data-driven models in closed-loop control for complex manufacturing processes. The capability of the model to handle multivariate constraints further demonstrates the application potential of data-driven methods in the field of closed-loop control for complex manufacturing processes.

For the manufacturing of demanding biomedical metals, it is essential to ensure that the microstructures and macroscopic properties of the produced materials comply with stringent biomedical requirements, thereby maximizing the service life. Through ML-enhanced closed-loop control and adaptive manufacturing, the qualification rate and performance consistency of ML biomedical metals products can be significantly improved, while reducing reliance on operator expertise. Ultimately, this speeds up the process of bringing highly reliable, customized biomedical metals to market, paving the way for a more autonomous and intelligent future.

5. Summary and outlooks

5.1. Summary

This review examines and elaborates on the role and advancements of ML in the field of AM for biomedical metals, particularly in three core areas: forward prediction, inverse optimization, and quality control. ML is emerging as a key driver for understanding and optimizing this complex manufacturing process, propelling the technology from experience-dependent to data-driven processes.

In forward prediction, ML functions as an efficient surrogate model, accurately constructing nonlinear mappings from process parameters to macrostructure, microstructure, and mechanical properties. This lays the foundation for achieving first-time-right manufacturing. For inverse optimization, ML has driven a paradigm shift from trial-and-error experimentation to intelligent decision-making. Through sophisticated algorithms, it enables efficient searches and multi-objective trade-offs can be achieved within high-dimensional parameter spaces, thereby determining optimal process solutions for biomedical metals that meet complex clinical requirements. In quality control, ML has achieved a leap from passive detection to active intervention by integrating diverse sensor data. Through real-time identification and diagnosis of process anomalies, it establishes closed-loop adaptive manufacturing capabilities, thereby paving a viable technical pathway for zero-defect production of biomedical metals.

5.2. Current challenges

Despite significant progress in ML for AM biomedical metals, its further development and application still face critical bottlenecks:

(i) Dual challenges of data quality and quantity: The lack of high-quality, large-scale datasets remains a primary factor constraining model performance. Experimental data on biomedical metals is extremely costly to acquire, and inconsistent data standards across research institutions create severe data segregation.

(ii) Insufficient model generalization: Although existing models typically perform well under specific material and process conditions, their generalization capabilities decline significantly when confronted with new material systems or process changes. This restricts the adoption of ML solutions in widespread industrial scenarios.

(iii) Balancing physical consistency and interpretability: Most current ML models remain black boxes, with weak correlations between their predictions and underlying physical mechanisms.

(iv) Complexity of multiscale modeling: Cross-scale modeling spanning from microstructural evolution to macroscopic properties remains a major challenge. Integrating physical information across different scales and establishing accurate mapping relationships requires in-depth research.

(v) Technical barriers for real-time applications: Deploying ML models for online quality control and real-time process adjustments faces multiple technical hurdles, including computational efficiency, latency requirements, and system integration.

5.3. Outlooks

Although ML has achieved significant results in individual stages, the future development of biomedical metals AM inevitably requires breaking down barriers between these stages to build a comprehensive, multi-functional intelligent technology chain spanning front-end design to back-end manufacturing.[156] Future research will focus on the following key directions:

(i) Overcoming data constraints: Future efforts should concentrate on the development of small-sample learning, zero-shot learning, and meta-learning/ transfer learning frameworks across materials and devices. The transfer of knowledge from data-rich domains to data-scarce domains is a significant aspect of this approach, as it reduces reliance on the volume of data in the target domain while enhancing the model's generalization capabilities.

(ii) Enhancing model credibility: The incorporation of physical laws as soft or hard constraints within models, for instance through the construction of physics-informed neural networks, ensures that predictions are aligned with physical principles. Concurrently, the widespread implementation of interpretability tools such as SHAP and local interpretable model-agnostic explanations (LIME) serves to transform opaque systems into comprehensible ones.

(iii) Prospective smart alloy design and manufacturability prediction: The starting point for the future should be further advanced to the material design itself. Generative models and active learning should be leveraged to reverse-engineer novel alloys that simultaneously exhibit ideal biological functionality and superior printability,[157-159] establishing a quadruple-loop design paradigm of composition-structure-property-manufacturability to achieve synergistic design of materials and processes from the outset.

(iv) Establishing digital archives for AM process: AM is a process with strong temporal dependencies, where the quality of each layer is cumulatively influenced by the thermal history and physical state of preceding layers. By preserving layer-by-layer data throughout the manufacturing process for each component, the construction of digital archives holds immeasurable value for product performance traceability and data-driven certification systems.

(v) Further combination of digital twins: Enhance real-time interaction and online decision-making between digital twins and physical production lines to drive adaptive adjustments to process parameters, thereby achieving precise closed-loop control.[160]

In summary, the development of an integrated intelligent technology system represents an inevitable trend. In the future, driven by clinical needs, the integration of structural design, intelligent manufacturing, and performance regulation within a unified framework will be achieved to achieve full-process closed-loop optimization. The integration of design, prediction, optimization, and control into a unified framework has the potential to enhance the capabilities of AM in high-end medical applications. This approach will deliver efficient, cost-effective, and highly reliable personalized medical solutions for patients.

Acknowledgments

None.

Funding

The authors acknowledge the financial supports from the National Key Research and Development Program of China (Grant No. 2024YFE0109000), the National Natural Science Foundation of China (Grant Nos. 52274387, 52311530772), the Medical-Engineering Cross Foundation of Shanghai Jiao Tong University (Grant No. YG2024LC04), and the Fundamental Research Funds for the Central Universities (Grant No. YG2023QNA21).

Conflict of interest

The authors declare that they have no competing interests.

Author contributions

Conceptualization: Yi Mao, Liqiang Wang, Uglov Vladimir, Zhou Jing
Visualization: Yi Mao, Deyu Jiang
Writing–original draft: Yi Mao, Deyu Jiang
Writing–review & editing: All authors

Ethics approval and consent to participate

Not applicable.

Consent for publication

Not applicable.

Availability of data

Not applicable.

References

1. Cui Y, Wang L, Zhang L. Towards load-bearing biomedical titanium-based alloys: From essential requirements to future developments. *Prog Mater Sci*. 2024;144:101277.

doi: 10.1016/j.pmatsci.2024.101277

2. Isik M, Avila JD, Bandyopadhyay A. Alumina and tricalcium phosphate added CoCr alloy for load-bearing implants. *Addit Manuf*. 2020;36:101553.

doi: 10.1016/j.addma.2020.101553

3. Dong J, Lin T, Shao H, *et al.* Advances in degradation behavior of biomedical magnesium alloys: A review. *J Alloys Compd*. 2022;908:164600.

doi: 10.1016/j.jallcom.2022.164600

4. Perumal G, Ayyagari A, Chakrabarti A, *et al.* Friction stir processing of stainless steel for ascertaining its superlative performance in bioimplant applications. *ACS Appl Mater Interfaces*. 2017;9(42):36615-36631.

doi: 10.1021/acsami.7b11064

5. Sarraf M, Rezvani Ghomi E, Alipour S, Ramakrishna S, Liana Sukiman N. A state-of-the-art review of the fabrication and characteristics of titanium and its alloys for biomedical applications. *Bio Des Manuf*. 2022;5(2):371-395.

doi: 10.1007/s42242-021-00170-3

6. Hao YL, Li SJ, Yang R. Biomedical titanium alloys and their additive manufacturing. *Rare Metals*. 2016;35(9):661-671.

doi: 10.1007/s12598-016-0793-5

7. Bandyopadhyay A, Mitra I, Avila JD, Upadhyayula M, Bose S. Porous metal implants: Processing, properties, and challenges. *Int J Extreme Manuf*. 2023;5(3):032014.

doi: 10.1088/2631-7990/acdd35

8. Yang Y, Jiang R, Han C, *et al*. Frontiers in laser additive manufacturing technology. *Addit Manuf Front*. 2024;3(4):200160.

doi: 10.1016/j.amf.2024.200160

9. Zhang LC, Wang J. Stabilizing 3D-printed metal alloys. *Science*. 2024;383(6683):586-587.

doi: 10.1126/science.adn6566

10. Wong KC, Scheinemann P. Additive manufactured metallic implants for orthopaedic applications. *Sci China Mater*. 2018;61(4):440-454.

doi: 10.1007/s40843-017-9243-9

11. Luna V, Trujillo L, Gamon A, *et al.* Comprehensive and comparative heat treatment of additively manufactured inconel 625 alloy and corresponding microstructures and mechanical properties. *J Manuf Mater Process*. 2022;6(5):107.

doi: 10.3390/jmmp6050107

12. Alghamdi A, Downing D, Tino R, *et al*. Buckling phenomena in AM lattice strut elements: A design tool applied to Ti-6Al-4V LB-PBF. *Mater Des*. 2021;208:109892.

doi: 10.1016/j.matdes.2021.109892

13. Babuska TF, Krick BA, Susan DF, Kustas AB. Comparison of powder bed fusion and directed energy deposition for tailoring mechanical properties of traditionally brittle alloys. *Manuf Lett*. 2021;28:30-34.

doi: 10.1016/j.mfglet.2021.02.003

14. Gotterbarm MR, Seifi M, Melzer D, *et al*. Small scale testing of IN718 single crystals manufactured by EB-PBF. *Addit Manuf*. 2020;36:101449.

doi: 10.1016/j.addma.2020.101449

15. Qian M, Xu W, Brandt M, Tang HP. Additive manufacturing and postprocessing of Ti-6Al-4V for superior mechanical properties. *MRS Bull*. 2016;41(10):775-784.

doi: 10.1557/mrs.2016.215

16. Behjat A, Sanaei S, Mosallanejad MH, *et al*. A novel titanium alloy for load-bearing biomedical implants: Evaluating the antibacterial and biocompatibility of Ti536 produced via electron beam powder bed fusion additive manufacturing process. *Biomater Adv*. 2024;163:213928.

doi: 10.1016/j.bioadv.2024.213928

17. Ma HY, Wang JC, Qin P, *et al.* Advances in additively manufactured titanium alloys by powder bed fusion and directed energy deposition: Microstructure, defects, and mechanical behavior. *J Mater Sci Technol*. 2024;183:32-62.

doi: 10.1016/j.jmst.2023.11.003

18. Attar H, Calin M, Zhang LC, Scudino S, Eckert J. Manufacture by selective laser melting and mechanical behavior of commercially pure titanium. *Mater Sci Eng A*. 2014;593:170-177.

doi: 10.1016/j.msea.2013.11.038

19. Zhao B, Wang H, Qiao N, Wang C, Hu M. Corrosion resistance characteristics of a Ti-6Al-4V alloy scaffold that is fabricated by electron beam melting and selective laser melting for implantation *in vivo*. *Mater Sci Eng C*. 2017;70:832-841.

doi: 10.1016/j.msec.2016.07.045

20. Bai Y, Gai X, Li S, *et al*. Improved corrosion behaviour of electron beam melted Ti-6Al–4V alloy in phosphate buffered saline. *Corros Sci*. 2017;123:289-296.

doi: 10.1016/j.corsci.2017.05.003

21. Cui YW, Chen LY, Qin P, *et al.* Metastable pitting corrosion behavior of laser powder bed fusion produced Ti-6Al-4V in Hank's solution. *Corros Sci*. 2022;203:110333.

doi: 10.1016/j.corsci.2022.110333

22. Shao L, Du Y, Dai K, *et al*. β-Ti alloys for orthopedic and dental applications: A review of progress on improvement of properties through surface modification. *Coatings*. 2021;11(12):1446.

doi: 10.3390/coatings11121446

23. Wang B, Luo M, Shi Z, *et al*. Porous titanium alloys for medical application: Progress in preparation process and

surface modification research. *Mater Sci Addit Manuf*. 2024;3(1):2753.

doi: 10.36922/msam.2753

24. Kumar P, Sawant MS, Jain NK, Gupta S. Study of mechanical characteristics of additively manufactured Co-Cr-Mo-2/4/6Ti alloys for knee implant material. *CIRP J Manuf Sci Technol*. 2022;39:261-275.

doi: 10.1016/j.cirpj.2022.08.015

25. Wang Z, Yan Y, Wang Y, Su Y, Qiao L. Lifecycle of cobalt-based alloy for artificial joints: From bulk material to nanoparticles and ions due to bio-tribocorrosion. *J Mater Sci Technol*. 2020;46:98-106.

doi: 10.1016/j.jmst.2019.12.010

26. Kong D, Dong C, Wei S, *et al*. About metastable cellular structure in additively manufactured austenitic stainless steels. *Addit Manuf*. 2021;38:101804.

doi: 10.1016/j.addma.2020.101804

27. Abd-Elaziem W, Elkatatny S, Sebaey TA, Darwish MA, Abd El-Baky MA, Hamada A. Machine learning for advancing laser powder bed fusion of stainless steel. *J Mater Res Technol*. 2024;30:4986-5016.

doi: 10.1016/j.jmrt.2024.04.130

28. Guo Y, Sun M, Zhang W, Wang L. Machine learning in enhancing corrosion resistance of magnesium alloys: A comprehensive review. *Metals*. 2023;13(10):1790.

doi: 10.3390/met13101790

29. Li K, Ji C, Bai S, Jiang B, Pan F. Selective laser melting of magnesium alloys: Necessity, formability, performance, optimization and applications. *J Mater Sci Technol*. 2023;154:65-93.

doi: 10.1016/j.jmst.2022.12.053

30. Singh YP, Moses JC, Bhardwaj N, Mandal BB. Overcoming the dependence on animal models for osteoarthritis therapeutics - the promises and prospects of *in vitro* models. *Adv Healthc Mater*. 2021;10(20):e2100961.

doi: 10.1002/adhm.202100961

31. Li HF, Shi ZZ, Wang LN. Opportunities and challenges of biodegradable Zn-based alloys. *J Mater Sci Technol*. 2020;46:136-138.

doi: 10.1016/j.jmst.2019.12.014

32. Heiden M. Magnesium, iron and zinc alloys, the trifecta of bioresorbable orthopaedic and vascular implantation - a review. *J Biotechnol Biomater*. 2015;5:2.

doi: 10.4172/2155-952X.1000178

33. Wen P, Qin Y, Chen Y, *et al.* Laser additive manufacturing of Zn porous scaffolds: Shielding gas flow, surface quality and densification. *J Mater Sci Technol*. 2019;35(2):368-376.

doi: 10.1016/j.jmst.2018.09.065

34. Qin Y, Wen P, Guo H, *et al.* Additive manufacturing of biodegradable metals: Current research status and future perspectives. *Acta Biomater*. 2019;98:3-22.

doi: 10.1016/j.actbio.2019.04.046

35. Davoodi E, Montazerian H, Mirhakimi AS, *et al*. Additively manufactured metallic biomaterials. *Bioact Mater*. 2022;15:214-249.

doi: 10.1016/j.bioactmat.2021.12.027

36. Tang Z, Peng X, Li K, Metaxas DN. Towards efficient U-nets: A coupled and quantized approach. *IEEE Trans Pattern Anal Mach Intell*. 2020;42(8):2038-2050.

doi: 10.1109/TPAMI.2019.2907634

37. Janiesch C, Zschech P, Heinrich K. Machine learning and deep learning. *Electron Mark*. 2021;31(3):685-695.

doi: 10.1007/s12525-021-00475-2

38. Louridas P, Ebert C. Machine learning. *IEEE Softw*. 2016;33(5):110-115.

doi: 10.1109/MS.2016.114

39. Liu J, Ye J, Izquierdo DS, Vinel A, Shamsaei N, Shao S. A review of machine learning techniques for process and performance optimization in laser beam powder bed fusion additive manufacturing. *J Intell Manuf*. 2022;34:1-27.

doi: 10.1007/s10845-022-02012-0

40. Rui Z, Liu J, Shi Y, Wang D. Additive manufacturing method of lattice structure based on material manufacturing performance driven: Using machine learning to optimize manufacturing process. *Addit Manuf Front*. 2025:200258.

doi: 10.1016/j.amf.2025.200258

41. Calderon CE, Plata JJ, Toher C, *et al*. The AFLOW standard for high-throughput materials science calculations. *Computat Mater Sci*. 2015;108:233-238.

doi: 10.1016/j.commatsci.2015.07.019

42. Kirklin S, Saal JE, Meredig B, *et al*. The open quantum materials database (OQMD): Assessing the accuracy of DFT formation energies. *NPJ Computat Mater*. 2015;1(1):15010.

doi: 10.1038/npjcompumats.2015.10

43. Brykov MN, Petryshynets I, Pruncu CI, *et al.* Machine learning modelling and feature engineering in seismology experiment. *Sensors (Basel)*. 2020;20(15):4228.

doi: 10.3390/s20154228

44. Garg M, Goel A. Preserving integrity in online assessment using feature engineering and machine learning. *Expert Syst Appl*. 2023;225:120111.

doi: 10.1016/j.eswa.2023.120111

45. Xu M, Guo LZ. Learning from group supervision: The impact of supervision deficiency on multi-label learning. *Sci China Inform Sci*. 2021;64(3):130101.

doi: 10.1007/s11432-020-3132-4

46. Sarkar JP, Saha I, Chakraborty S, Maulik U. Machine learning integrated credibilistic semi supervised clustering for categorical data. *Appl Soft Comput*. 2020;86:105871.

doi: 10.1016/j.asoc.2019.105871

47. Hammarström H, Borin L. Unsupervised learning of morphology. *Comput Linguist*. 2011;37(2):309-350.

doi: 10.1162/COLI_a_00050

48. Nurhalizah RS, Ardianto R, Purwono P. Analisis supervised dan unsupervised learning pada machine learning: Systematic literature review. *J Ilmu Komput Inform*. 2024;4(1):61-72.

doi: 10.54082/jiki.168

49. Abd-Elaziem W, Darwish MA, Hamada A, Daoush WM. Titanium-Based alloys and composites for orthopedic implants Applications: A comprehensive review. *Mater Des*. 2024;241:112850.

doi: 10.1016/j.matdes.2024.112850

50. Aromiwura AA, Settle T, Umer M, *et al.* Artificial intelligence in cardiac computed tomography. *Prog Cardiovasc Dis*. 2023;81:54-77.

doi: 10.1016/j.pcad.2023.09.001

51. Emmert-Streib F, Dehmer M. Evaluation of regression models: Model assessment, model selection and generalization error. *Mach Learn Knowl Extract*. 2019;1(1):521-551.

doi: 10.3390/make1010032

52. Saxena A, Prasad M, Gupta A, *et al.* A review of clustering techniques and developments. *Neurocomputing*. 2017;267:664-681.

doi: 10.1016/j.neucom.2017.06.053

53. Bahl S, Suwas S, Chatterjee K. Comprehensive review on alloy design, processing, and performance of β Titanium alloys as biomedical materials. *Int Mater Rev*. 2021;66(2):114-139.

doi: 10.1080/09506608.2020.1735829

54. Li H, Yang X. Effect of surface morphologies on the *in vitro* and *in vivo* properties of biomedical metallic materials. *ACS Biomater Sci Eng*. 2024;10(10):6017-6028.

doi: 10.1021/acsbiomaterials.4c00942

55. Wang J, Dou J, Wang Z, Hu C, Yu H, Chen C. Research progress of biodegradable magnesium-based biomedical materials: A review. *J Alloys Compd*. 2022;923:166377.

doi: 10.1016/j.jallcom.2022.166377

56. Guo AXY, Cheng L, Zhan S, *et al*. Biomedical applications of the powder-based 3D printed titanium alloys: A review. *J Mater Sci Technol*. 2022;125:252-264.

doi: 10.1016/j.jmst.2021.11.084

57. Li Y, Tan J, Qian C, Liu X, Nie R. Review of machine learning-assisted multi-property design of high-entropy alloys: Phase structure, mechanical, tribological, corrosion, and hydrogen storage properties. *J Mater Res Technol*. 2025;37:3350-3377.

doi: 10.1016/j.jmrt.2025.07.005

58. Hu M, Tan Q, Knibbe R, *et al*. Recent applications of machine learning in alloy design: A review. *Mater Sci Eng R Rep*. 2023;155:100746.

doi: 10.1016/j.mser.2023.100746

59. Jin L, Zhai X, Wang K, *et al.* Big data, machine learning, and digital twin assisted additive manufacturing: A review. *Mater Des*. 2024;244:113086.

doi: 10.1016/j.matdes.2024.113086

60. Zhu K, Fuh JYH, Lin X. Metal-based additive manufacturing condition monitoring: A review on machine learning based approaches. *IEEE/ASME Trans Mechatronics*. 2022;27(5):2495-2510.

doi: 10.1109/TMECH.2021.3110818

61. Chen K, Zhang P, Yan H, *et al.* A review of machine learning in additive manufacturing: design and process. *Int J Adv Manuf Technol*. 2024;135(3):1051-1087.

doi: 10.1007/s00170-024-14543-2

62. Inayathullah S, Buddala R. Review of machine learning applications in additive manufacturing. *Results Eng*. 2025;25:103676.

doi: 10.1016/j.rineng.2024.103676

63. Kim H, Kim KH, Jeong J, Jeon H, Jung ID. Advancing intelligent additive manufacturing: Machine learning approaches for process optimization and quality control. *Int J AI Mater Des*. 2025;2(2):27-55.

doi: 10.36922/ijamd025130010

64. Li Z, Qiu J, Xu H, *et al*. Characteristics of β-type Ti-41Nb alloy produced by laser powder bed fusion: Microstructure, mechanical properties and *in vitro* biocompatibility. *J Mater Sci Technol*. 2022;124:260-272.

doi: 10.1016/j.jmst.2022.02.026

65. Bartolomeu F, Faria S, Carvalho O, *et al.* Predictive models for physical and mechanical properties of Ti6Al4V produced by Selective Laser Melting. *Mater Sci Eng A*. 2016;663:181-192.

doi: 10.1016/j.msea.2016.03.113

66. Maitra V, Shi J, Lu C. Robust prediction and validation of as-built density of Ti-6Al-4V parts manufactured via selective laser melting using a machine learning approach. *J Manuf Process*. 2022;78:183-201.

doi: 10.1016/j.jmapro.2022.04.020

67. Jiang D, Luo M, Liu C, *et al*. 3D Printing parameter optimisation combined with heat treatment for achieving high density and enhanced performance in refractory high-

entropy alloys. *Virtual Phys Prototyp.* 2025;20(1):e2524524.

doi: 10.1080/17452759.2025.2524524

68. Gor M, Dobriyal A, Wankhede V, *et al*. Density prediction in powder bed fusion additive manufacturing: Machine learning-based techniques. *Appl Sci*. 2022;12(14):7271.

doi: 10.3390/app12147271

69. Chan KS, Koike M, Mason RL, Okabe T. Fatigue life of titanium alloys fabricated by additive layer manufacturing techniques for dental implants. *Metallurgical Mater Trans A*. 2013;44(2):1010-1022.

doi: 10.1007/s11661-012-1470-4

70. Dawood HI, Mohammed KS, Rahmat A, Uday MB. The influence of the surface roughness on the microstructures and mechanical properties of 6061 aluminium alloy using friction stir welding. *Surf Coat Technol*. 2015;270:272-283.

doi: 10.1016/j.surfcoat.2015.02.045

71. Jiang X, Lu J, Zhao N, Chen Z, Zhao Z. A review of wear in additive manufacturing: Wear mechanism, materials, and process. *Lubricants*. 2024;12(9):321.

doi: 10.3390/lubricants12090321

72. Pegues J, Roach M, Scott Williamson R, Shamsaei N. Surface roughness effects on the fatigue strength of additively manufactured Ti-6Al-4V. *Int J Fatigue*. 2018;116:543-552.

doi: 10.1016/j.ijfatigue.2018.07.013

73. Koo J, Park E, Baek AMC, Kim N. *The Research of Surface Roughness Prediction with Machine Learning According to Process Parameters in Laser Powder Bed Fusion*. Berlin: Springer Singapore; 2022. p. 62-65.

74. Xia C, Pan Z, Polden J, Li H, Xu Y, Chen S. Modelling and prediction of surface roughness in wire arc additive manufacturing using machine learning. *J Intell Manuf*. 2022;33(5):1467-1482.

doi: 10.1007/s10845-020-01725-4

75. So MS, Seo GJ, Kim DB, Shin JH. Prediction of metal additively manufactured surface roughness using deep neural network. *Sensors*. 2022;22(20):7955.

doi: 10.3390/s22207955

76. Mukherjee T, Elmer JW, Wei HL, *et al*. Control of grain structure, phases, and defects in additive manufacturing of high-performance metallic components. *Prog Mater Sci*. 2023;138:101153.

doi: 10.1016/j.pmatsci.2023.101153

77. Yan F, Xiong W, Faierson E. Grain structure control of additively manufactured metallic materials. *Materials*. 2017;10(11):1260.

doi: 10.3390/ma10111260

78. Zhang F, Huang K, Zhao K, *et al*. Directed energy deposition combining high-throughput technology and machine learning to investigate the composition-microstructure-mechanical property relationships in titanium alloys. *J Mater Process Technol*. 2023;311:117800.

doi: 10.1016/j.jmatprotec.2022.117800

79. Calvat M, Bean C, Anjaria D, *et al*. Learning metal microstructural heterogeneity through spatial mapping of diffraction latent space features. *NPJ Computat Mater*. 2025;11(1):284.

doi: 10.1038/s41524-025-01770-8

80. Chi J, Huang X, He D, *et al.* Obtaining strength and ductility synergy for directed energy deposited Ti17 alloys by machine learning. *Mater Lett*. 2024;356:135537.

doi: 10.1016/j.matlet.2023.135537

81. Wang H, Li B, Zhang W, Xuan F. Microstructural feature-driven machine learning for predicting mechanical tensile strength of laser powder bed fusion (L-PBF) additively manufactured Ti6Al4V alloy. *Eng Fract Mech*. 2024;295:109788.

doi: 10.1016/j.engfracmech.2023.109788

82. Liu S, Stebner AP, Kappes BB, Zhang X. Machine learning for knowledge transfer across multiple metals additive manufacturing printers. *Addit Manuf*. 2021;39:101877.

doi: 10.1016/j.addma.2021.101877

83. Fang L, Cheng L, Glerum JA, Bennett J, Cao J, Wagner GJ. Data-driven analysis of process, structure, and properties of additively manufactured Inconel 718 thin walls. *NPJ Computat Mater*. 2022;8(1):126.

doi: 10.1038/s41524-022-00808-5

84. Liu YT, Chua C, Soh V, Sun Z, Chua CK, Sing SL. Revealing the underlying mechanism in controlling Young's modulus of additively manufactured Ti-6Al-4V using fuzzified machine learning. *Virtual Phys Prototyp.* 2025;20(1):e2443103.

doi: 10.1080/17452759.2024.2443103

85. Dong S, Wang Y, Li J, Li Y, Wang L, Zhang J. Machine learning aided prediction and design for the mechanical properties of magnesium alloys. *Metals Mater Int*. 2024;30(3):593-606.

doi: 10.1007/s12540-023-01531-6

86. Akbari P, Zamani M, Mostafaei A. Machine learning prediction of mechanical properties in metal additive manufacturing. *Addit Manuf*. 2024;91:104320.

doi: 10.1016/j.addma.2024.104320

87. Lian Z, Li M, Lu W. Fatigue life prediction of aluminum alloy via knowledge-based machine learning. *Int J Fatigue*. 2022;157:106716.

doi: 10.1016/j.ijfatigue.2021.106716

88. Johnsen AR, Petersen JE, Pedersen MM, Yıldırım HC. Factors affecting the fatigue strength of additively manufactured Ti-6Al-4V parts. *Weld World*. 2023;68(2):361-409.

doi: 10.1007/s40194-023-01604-5

89. Zhan Z, Hu W, Meng Q. Data-driven fatigue life prediction in additive manufactured titanium alloy: A damage mechanics based machine learning framework. *Eng Fract Mechan*. 2021;252:107850.

doi: 10.1016/j.engfracmech.2021.107850

90. Zhang M, Sun CN, Zhang X, *et al*. High cycle fatigue life prediction of laser additive manufactured stainless steel: A machine learning approach. *Int J Fatigue*. 2019;128:105194.

doi: 10.1016/j.ijfatigue.2019.105194

91. Shen T, Zhang W, Li B. Machine learning-enabled predictions of as-built relative density and high-cycle fatigue life of Ti6Al4V alloy additively manufactured by laser powder bed fusion. *Mater Today Commun*. 2023;37:107286.

doi: 10.1016/j.mtcomm.2023.107286

92. Tang YT, Panwisawas C, Ghoussoub JN, *et al*. Alloys-by-design: Application to new superalloys for additive manufacturing. *Acta Mater*. 2021;202:417-436.

doi: 10.1016/j.actamat.2020.09.023

93. Wang L, Zhang Y, Chia HY, Yan W. Mechanism of keyhole pore formation in metal additive manufacturing. *NPJ Computat Mater*. 2022;8(1):22.

doi: 10.1038/s41524-022-00699-6

94. Lee JA, Sagong MJ, Jung J, Kim ES, Kim HS. Explainable machine learning for understanding and predicting geometry and defect types in Fe-Ni alloys fabricated by laser metal deposition additive manufacturing. *J Mater Res Technol*. 2023;22:413-423.

doi: 10.1016/j.jmrt.2022.11.137

95. Gui Y, Aoyagi K, Bian H, Chiba A. Detection, classification and prediction of internal defects from surface morphology data of metal parts fabricated by powder bed fusion type additive manufacturing using an electron beam. *Addit Manuf*. 2022;54:102736.

doi: 10.1016/j.addma.2022.102736

96. Du Y, Mukherjee T, DebRoy T. Physics-informed machine learning and mechanistic modeling of additive manufacturing to reduce defects. *Appl Mater Today*. 2021;24:101123.

doi: 10.1016/j.apmt.2021.101123

97. Dharmadhikari S, Menon N, Basak A. A reinforcement learning approach for process parameter optimization in additive manufacturing. *Addit Manuf*. 2023;71:103556.

doi: 10.1016/j.addma.2023.103556

98. Zhou HR, Yang H, Li HQ, *et al*. Advancements in machine learning for material design and process optimization in the field of additive manufacturing. *China Foundry*. 2024;21(2):101-115.

doi: 10.1007/s41230-024-3145-3

99. Liu D, Wang Y. Metal additive manufacturing process design based on physics constrained neural networks and multi-objective Bayesian optimization. *Manuf Lett*. 2022;33:817-827.

doi: 10.1016/j.mfglet.2022.07.101

100. Ma J, Cao B, Dong S, *et al*. MLMD: A programming-free AI platform to predict and design materials. *NPJ Computat Mater*. 2024;10(1):59.

doi: 10.1038/s41524-024-01243-4

101. Hou Yi C, Jianzhao W, Xinzhi W, Wentao Y. Process parameter optimization of metal additive manufacturing: A review and outlook. *J Mater Inform*. 2022;2(4):16.

doi: 10.20517/jmi.2022.18

102. Grbcic L, Müller J, de Jong WA. Efficient inverse design optimization through multi-fidelity simulations, machine learning, and boundary refinement strategies. *Eng Comput*. 2024;40(6):4081-4108.

doi: 10.1007/s00366-024-02053-4

103. Hua Y, Jin Y, Hao K, Cao Y. Generating multiple reference vectors for a class of many-objective optimization problems with degenerate Pareto fronts. *Complex Intell Syst*. 2020;6(2):275-285.

doi: 10.1007/s40747-020-00136-5

104. Deb K, Pratap A, Agarwal S, Meyarivan T. A fast and elitist multiobjective genetic algorithm: NSGA-II. *IEEE Transactions on Evolutionary Computation*. 2002;6(2):182-197. doi:10.1109/4235.996017

105. Wang J, Feng L, Xu J, *et al*. Optimal process parameter combinations search for desired deposited layer geometry in laser-arc hybrid additive manufacturing based on multi-pass overlapping deposited layer contour prediction model and improved NSGA-II algorithm. *Optics Laser Technol*. 2025;187:112700.

doi: 10.1016/j.optlastec.2025.112700

106. Padhye N, Deb K. Multi-objective optimisation and multi-criteria decision making in SLS using evolutionary approaches. *Rapid Prototyp J*. 2011;17(6):458-478.

doi: 10.1108/13552541111184198

107. Aboutaleb AM, Mahtabi MJ, Tschopp MA, Bian L. Multi-objective accelerated process optimization of mechanical properties in laser-based additive manufacturing: Case study on Selective Laser Melting (SLM) Ti-6Al-4V. *J Manuf Process*. 2019;38:432-444.

doi: 10.1016/j.jmapro.2018.12.040

108. Startt J, McCarthy MJ, Wood MA, Donegan S, Dingreville R. Bayesian blacksmithing: Discovering thermomechanical properties and deformation mechanisms in high-entropy refractory alloys. *NPJ Computat Mater*. 2024;10(1):164.

doi: 10.1038/s41524-024-01353-z

109. Wang ZL, Ogawa T, Adachi Y. Influence of algorithm parameters of Bayesian optimization, genetic algorithm, and particle swarm optimization on their optimization performance. *Adv Theory Simul*. 2019;2(10):1900110.

doi: 10.1002/adts.201900110

110. Palm N, Landerer M, Palm H. Gaussian process regression based multi-objective Bayesian optimization for power system design. *Sustainability*. 2022;14(19):12777.

doi: 10.3390/su141912777

111. Moradi A, Tajalli S, Mosallanejad MH, Saboori A. Intelligent laser-based metal additive manufacturing: A review on machine learning for process optimization and property prediction. *Int J Adv Manuf Technol*. 2024;136(2):527-560.

doi: 10.1007/s00170-024-14858-0

112. Narayana PL, Kim JH, Lee J, *et al.* Optimization of process parameters for direct energy deposited Ti-6Al-4V alloy using neural networks. *Int J Adv Manuf Technol*. 2021;114(11):3269-3283.

doi: 10.1007/s00170-021-07115-1

113. Nguyen DS, Park HS, Lee CM. Optimization of selective laser melting process parameters for Ti-6Al-4V alloy manufacturing using deep learning. *J Manuf Process*. 2020;55:230-235.

doi: 10.1016/j.jmapro.2020.04.014

114. Gan Z, Li H, Wolff SJ, *et al*. Data-driven microstructure and microhardness design in additive manufacturing using a self-organizing map. *Engineering*. 2019;5(4):730-735.

doi: 10.1016/j.eng.2019.03.014

115. Tapia G, Khairallah S, Matthews M, King WE, Elwany A. Gaussian process-based surrogate modeling framework for process planning in laser powder-bed fusion additive manufacturing of 316L stainless steel. *Int J Adv Manuf Technol*. 2018;94(9):3591-3603.

doi: 10.1007/s00170-017-1045-z

116. Buchner C, Riedle B, Krauß J, *et al*. Machine learning-driven multi-objective parameter optimization for sustainable, efficient, and high-quality ultrasonic wire bonding. *J Intell Manuf*. 2025.

doi: 10.1007/s10845-025-02615-3

117. Wang S, Xia P, Gong F, Zeng Q, Chen K, Zhao Y. Multi objective optimization of recycled aggregate concrete based on explainable machine learning. *J Clean Prod*. 2024;445:141045.

doi: 10.1016/j.jclepro.2024.141045

118. Meng L, Zhao J, Lan X, Yang H, Wang Z. Multi-objective optimisation of bio-inspired lightweight sandwich structures based on selective laser melting. *Virtual Phys Prototyp*. 2020;15(1):106-119.

doi: 10.1080/17452759.2019.1692673

119. Cai Y, Wang Y, Chen H, Xiong J. Searching optimal process parameters for desired layer geometry in wire-laser directed energy deposition based on machine learning. *Virtual Phys Prototyp*. 2024;19(1):e2352066.

doi: 10.1080/17452759.2024.2352066

120. Heiss A, Thatikonda VS, Klotz UE. Multi-objective optimization of LPBF manufacturing with Zn-4Al-1Cu alloy for technical applications. *J Manuf Process*. 2025;134:193-206.

doi: 10.1016/j.jmapro.2024.12.049

121. Peng S, Li T, Zhao J, *et al.* Towards energy and material efficient laser cladding process: Modeling and optimization using a hybrid TS-GEP algorithm and the NSGA-II. *J Clean Prod*. 2019;227:58-69.

doi: 10.1016/j.jclepro.2019.04.187

122. Hu Z, Huang C, Xie L, Hua L, Yuan Y, Zhang LC. Machine learning assisted quality control in metal additive manufacturing: A review. *Adv Powder Mater*. 2025;4(6):100342.

doi: 10.1016/j.apmate.2025.100342

123. Gerdes S, Gaikwad A, Ramesh S, Rivero IV, Tamayol A, Rao P. Monitoring and control of biological additive manufacturing using machine learning. *J Intell Manuf*. 2024;35(3):1055-1077.

doi: 10.1007/s10845-023-02092-6

124. Pereira AG, Barbosa GF, Filho MG, Shiki SB, Silva AL. Quality control in extrusion-based additive manufacturing: A review of machine learning approaches. *IEEE Trans Cybern*. 2025;55(6):2522-2534.

doi: 10.1109/tcyb.2025.3558515

125. Khanzadeh M, Chowdhury S, Tschopp MA, Doude HR, Marufuzzaman M, Bian L. *In-situ* monitoring of melt pool images for porosity prediction in directed energy deposition processes. *IISE Trans*. 2019;51(5):437-455.

doi: 10.1080/24725854.2017.1417656

126. Yang T, Mazumder S, Jin Y, *et al*. A review of diagnostics methodologies for metal additive manufacturing processes and products. *Materials (Basel)*. 2021;14(17):4929.

doi: 10.3390/ma14174929

127. Zheng L, Zhang Q, Cao H, *et al*. Melt pool boundary extraction and its width prediction from infrared images in selective laser melting. *Mater Des*. 2019;183:108110.

doi: 10.1016/j.matdes.2019.108110

128. Mohr G, Altenburg SJ, Ulbricht A, *et al*. *In-situ* defect detection in laser powder bed fusion by using thermography and optical tomography-comparison to computed tomography. *Metals*. 2020;10(1):103.

doi: 10.3390/met10010103

129. Liu L, Ju F, Kim S. Online thermal profile prediction for large format additive manufacturing: A hybrid CNN-LSTM based approach. *Addit Manuf*. 2025;109:104882.

doi: 10.1016/j.addma.2025.104882

130. Lopez A, Bacelar R, Pires I, Santos TG, Sousa JP, Quintino L. Non-destructive testing application of radiography and ultrasound for wire and arc additive manufacturing. *Addit Manuf*. 2018;21:298-306.

doi: 10.1016/j.addma.2018.03.020

131. Wang J, Zhang X, Lu Y. Machine learning in image-based metal additive manufacturing process monitoring and control: A review. *Eng Sci Addit Manuf*. 2025;1(1):8548.

doi: 10.36922/esam.8548

132. Ansari MA, Crampton A, Garrard R, Cai B, Attallah M. A convolutional neural network (CNN) classification to identify the presence of pores in powder bed fusion images. *Int J Adv Manuf Technol*. 2022;120(7):5133-5150.

doi: 10.1007/s00170-022-08995-7

133. Lee H, Heogh W, Yang J, *et al.* Deep learning for *in-situ* powder stream fault detection in directed energy deposition process. *J Manuf Syst*. 2022;62:575-587.

doi: 10.1016/j.jmsy.2022.01.013

134. Yang Z, Zhu L, Dun Y, *et al*. *In-situ* monitoring of the melt pool dynamics in ultrasound-assisted metal 3D printing using machine learning. *Virtual Phys Prototyp*. 2023;18(1):e2251453.

doi: 10.1080/17452759.2023.2251453

135. Mi J, Zhang Y, Li H, *et al*. *In-situ* monitoring laser based directed energy deposition process with deep convolutional neural network. *J Intell Manuf*. 2023;34(2):683-693.

doi: 10.1007/s10845-021-01820-0

136. Prem PR, Sanker AP, Sebastian S, Kaliyavaradhan SK. A review on application of acoustic emission testing during additive manufacturing. *J Nondestr Eval*. 2023;42(4):96.

doi: 10.1007/s10921-023-01005-0

137. Yu Q, Zhang M, Mujumdar AS, Li J. AI-based additive manufacturing for future food: Potential applications, challenges and possible solutions. *Innov Food Sci Emerg Technol*. 2024;92:103599.

doi: 10.1016/j.ifset.2024.103599

138. Luo S, Ma X, Xu J, Li M, Cao L. Deep learning based monitoring of spatter behavior by the acoustic signal in selective laser melting. *Sensors (Basel)*. 2021;21(21):7179.

doi: 10.3390/s21217179

139. Rahman MA, Jamal S, Cruz MV, Silwal B, Taheri H. *In situ* process monitoring of multi-layer deposition in wire arc additive manufacturing (WAAM) process with acoustic data analysis and machine learning. *Int J Adv Manuf Technol*. 2024;132(9):5087-5101.

doi: 10.1007/s00170-024-13641-5

140. Montazeri M, Nassar AR, Dunbar AJ, Rao P. In-process monitoring of porosity in additive manufacturing using optical emission spectroscopy. *IISE Trans*. 2020;52(5):500-515.

doi: 10.1080/24725854.2019.1659525

141. Chen X, Fu Y, Kong F, *et al*. An in-process multi-feature data fusion nondestructive testing approach for wire arc additive manufacturing. *Rapid Prototyp J*. 2021;28(3):573-584.

doi: 10.1108/rpj-02-2021-0034

142. Gaikwad A, Giera B, Guss GM, Forien JB, Matthews MJ, Rao P. Heterogeneous sensing and scientific machine learning for quality assurance in laser powder bed fusion - A single-track study. *Addit Manuf*. 2020;36:101659.

doi: 10.1016/j.addma.2020.101659

143. Knaak C, Masseling L, Duong E, Abels P, Gillner A. Improving build quality in laser powder bed fusion using high dynamic range imaging and model-based reinforcement learning. *IEEE Access*. 2021;9:55214-55231.

doi: 10.1109/ACCESS.2021.3067302

144. Scime L, Beuth J. A multi-scale convolutional neural network for autonomous anomaly detection and classification in a laser powder bed fusion additive manufacturing process. *Addit Manuf*. 2018;24:273-286.

doi: 10.1016/j.addma.2018.09.034

145. Chen L, Bi G, Yao X, *et al*. Multisensor fusion-based digital twin for localized quality prediction in robotic laser-directed energy deposition. *Robot Comput Integr Manuf*. 2023;84:102581.

doi: 10.1016/j.rcim.2023.102581

146. Rescsanski S, Hebert R, Haghighi A, Tang J, Imani F. Towards intelligent cooperative robotics in additive manufacturing: Past, present, and future. *Robot Comput Integr Manuf*. 2025;93:102925.

doi: 10.1016/j.rcim.2024.102925

147. Abranovic B, Sarkar S, Chang-Davidson E, Beuth J. Melt pool level flaw detection in laser hot wire directed energy deposition using a convolutional long short-term memory autoencoder. *Addit Manuf*. 2024;79:103843.

doi: 10.1016/j.addma.2023.103843

148. Reutzel EW, Nassar AR. A survey of sensing and control systems for machine and process monitoring of directed-energy, metal-based additive manufacturing. *Rapid Prototyp J*. 2015;21(2):159-167.

doi: 10.1108/rpj-12-2014-0177

149. Wang Q, Michaleris P, Nassar AR, Irwin JE, Ren Y, Stutzman CB. Model-based feedforward control of laser

powder bed fusion additive manufacturing. *Addit Manuf*. 2020;31:100985.

doi: 10.1016/j.addma.2019.100985

150. Meng L, McWilliams B, Jarosinski W, *et al*. Machine learning in additive manufacturing: A review. *JOM*. 2020;72(6):2363-2377.

doi: 10.1007/s11837-020-04155-y

151. Ye D, Hong GS, Zhang Y, Zhu K, Fuh JYH. Defect detection in selective laser melting technology by acoustic signals with deep belief networks. *Int J Adv Manuf Technol*. 2018;96(5):2791-2801.

doi: 10.1007/s00170-018-1728-0

152. Armstrong AA, Pfeil A, Alleyne AG, Wagoner Johnson AJ. Process monitoring and control strategies in extrusion-based bioprinting to fabricate spatially graded structures. *Bioprinting*. 2021;21:e00126.

doi: 10.1016/j.bprint.2020.e00126

153. Liu Y, Wang L, Brandt M. Model predictive control of laser metal deposition. *Int J Adv Manuf Technol*. 2019;105(1):1055-1067.

doi: 10.1007/s00170-019-04279-9

154. Cao X, Ayalew B. Robust multivariable predictive control for laser-aided powder deposition processes. *J Franklin Instit*. 2019;356(5):2505-2529.

doi: 10.1016/j.jfranklin.2018.12.015

155. Chen YP, Karkaria V, Tsai YK, *et al.* Real-time decision-making for Digital Twin in additive manufacturing with Model Predictive Control using time-series deep neural networks. *J Manuf Syst*. 2025;80:412-424.

doi: 10.1016/j.jmsy.2025.03.009

156. Li Z, Birbilis N. NSGAN: A non-dominant sorting optimisation-based generative adversarial design framework for alloy discovery. *NPJ Computat Mater*. 2024;10(1):112.

doi: 10.1038/s41524-024-01294-7

157. Griebler JJ, Tappan AS, Rogers SA, Grillet AM, Kopatz JW. Printability criterion and filler characteristics model for material extrusion additive manufacturing. *Addit Manuf*. 2025;99:104651.

doi: 10.1016/j.addma.2025.104651

158. Ren W, Zhang YF, Wang WL, Ding SJ, Li N. Prediction and design of high hardness high entropy alloy through machine learning. *Mater Des*. 2023;235:112454.

doi: 10.1016/j.matdes.2023.112454

159. Trovato M, Belluomo L, Bici M, Prist M, Campana F, Cicconi P. Machine learning in design for additive manufacturing: A state-of-the-art discussion for a support tool in product design lifecycle. *Int J Adv Manuf Technol*. 2025;137:2157-2180.

doi: 10.1007/s00170-025-15273-9

160. Gunasegaram DR, Barnard AS, Matthews MJ, *et al*. Machine learning-assisted in-situ adaptive strategies for the control of defects and anomalies in metal additive manufacturing. *Addit Manuf*. 2024;81:104013.

doi: 10.1016/j.addma.2024.104013

ACCSCIENCE PUBLISHING

Engineering Science in Additive Manufacturing

ORIGINAL RESEARCH ARTICLE

Understanding the reusability of Ti6Al4V powder in laser powder bed fusion

Nathaniel W. Zuckschwerdt and Amit Bandyopadhyay*

W. M. Keck Biomedical Materials Research Lab, School of Mechanical and Materials Engineering, Washington State University, Pullman, Washington, United States of America

Abstract

This study aimed to determine the effects of how powder degrades in quality from use in the laser powder bed fusion process and investigate what changes in the powder cause defects in finished parts. It was determined that the reused powder affected the finished part quality, resulting in an increased number of lack-of-fusion pores. This was due to a change in the size distribution of the powder particles, characterized by an increase in larger sizes and a significant decrease in smaller sizes. There was an 11% increase in defective particles over the five prints that went through the sieving process, as well as an increase of ~2% of particles >63 μm, resulting in less powder that could be reused after each print. The results enabled the determination of the life of the powder due to the degradation of the powder from the differing property changes caused by the reuse of the powder.

Keywords: Ti6Al4V; Laser powder bed fusion; Powder degradation; Additive manufacturing; 3D printing

***Corresponding author:**
Amit Bandyopadhyay
(amitband@wsu.edu)

Citation: Zuckschwerdt NW, Bandyopadhyay A. Understanding the reusability of Ti6Al4V powder in laser powder bed fusion. *Eng Sci Add Manuf.* 2025;1(4):025420028. doi: 10.36922/ESAM025420028

Received: October 13, 2025

Revised: November 5, 2025

Accepted: November 5, 2025

Published online: November 17, 2025

1. Introduction

In the world of additive manufacturing (AM), most innovation and research efforts have focused on developing new, innovative materials and processes. Thus, it is of great importance to determine the effect that the starting materials will have on the finished products. Without this information, researchers could be pursuing an optimization of the parameters while reusing the same powder between each print, running into problems with the print that are not due to parameters, but instead are due to increasing issues with the starting materials resulting from the reuse of the powders.

With the desire to create processes that are as efficient as possible and use as few resources as possible, the world is looking towards AM for its future. From uses in the aerospace industry to biomedical implants, many items being made today could be manufactured in the future with AM.[1-6] In the biomedical field alone, over 500,000 implants made using AM are put into the human body per year in the United States. Within the field of aerospace, it takes years for a part to go from initial designs to being in a production aircraft, with every little thing about the part needing to be documented and examined, from the starting material to how each step of the manufacturing process needs to be verified, such that the process and part can be certified to be used in aircraft. In many of these processes, the end product is thoroughly examined to determine how the various parameters that can be adjusted have impacted the part being produced,

with little to no examination of the starting material used in the printing process. Thus, it is essential to understand the frequency of feed material reuse and how the reuse of powder impacts the quality of the finished product.[7-11]

At present, one method for utilizing powder for multiple prints while maintaining high quality is the process of sieving and adding a percentage of new powder.[12-14] This process is designed to extend the powder's lifespan and maintain its usability without requiring knowledge of its current properties. Thus, if it could be determined whether there are better ways to reuse the powder or know the extent to which the powder can be used without causing significant defects to the final product, it would lend itself to being able to use the powder at hand for longer while still having reliable manufacturing of the parts.[15-17] More extensive information on how the powder is degraded during the printing process and how the reuse processes can be improved to enable total use of the powder, rather than needing to throw out usable powder, is needed. With the correct information on how to process the powder to continue using it or when the powder has passed its reuse point and needs to be remanufactured, this waste can be significantly reduced while also minimizing the amount of energy required.[18-22]

This work aims to determine the reusability of Ti6Al4V (Ti64) powder in a laser powder bed fusion (LPBF) AM process. LPBF uses a laser energy source to either sinter or melt the material that is being printed on a layer-by-layer basis onto the build plate, creating the three-dimensional (3D) part in the bed of powder while being in an inert environment, unlike an electron beam PBF, thereby leading to slightly increased level of oxidation.[23,24] This is achieved by pushing the powder into the build volume with a roller at the designated layer height, then adhering it to the layer below by scanning with a laser across the powder in the desired locations for the current layer. The LPBF process generates waste powder from splatter resulting from the laser interacting with other particles in the build chamber, thereby forming larger and deformed powder particles.[25,26] After a print is finished, it is recollected for reuse in the next batch of printing. However, these defective powder particles can cause issues with subsequent prints if not appropriately addressed, and increase the number of particles that are not reusable. In the case of powders, the recollected powders are sieved before being used again, with minimal additional processing applied to the powder, including the mixing of new powder with the used powder to help minimize the defects of the used powder. A knowledge gap remains regarding the reusability of power for LPBF, which must be addressed to enhance the process's convenience, reliability, and overall efficiency, and to reduce the need for discarding feed material due to powder degradation.

With the importance of knowing how the reuse of powder affects the printing process and the part quality, much work has been done to investigate the effects with different powders.[27,28] Much of this work has been focused on the increase of oxygen content and decrease of flowability that occurs due to the oxidation/degradation of the powder during the printing process.[29,30] These types of characterizations are essential for all powders that are used when manufacturing with the LPBF process.[31,32] If the powders' flowability decreases sufficiently, defects may form within the parts, adversely affecting their mechanical properties.[33,34] With this in mind, there are still areas that can be expanded upon. In particular, sieving can show more information and possible correlation to the other powder properties, though this is related to the amount of the powder interacting with the laser during the printing process, causing the major defects that can be found in the used powders.

The objective of this research was to determine if there is a way to quickly identify the percentage of defects in feed material and identify the effects that may have on printed parts with simple processes. If only simple equipment is available to be used, such as sieves or an angle of repose tester, then the quality of the powder due to degradation could still be determined. Processes such as sieving are already conducted during the reuse process and can shed light on the powder quality without the need for more characterization. It was hypothesized that the reuse of Ti64 powder over an extended number of uses would decrease the printability of the powder and increases the number of defects in finished parts, while having a noticeable difference in the powder quality that can be examined with simple instruments. This will give users of LPBF systems the ability to quickly characterize their powder just by sieving the powder to identify the amount of powder that has degraded during the processes, as the powders should be sieved after every use before the powder is reused. The addition of testing the angle of repose will give more insight into how the powder is being affected by the printing process, while taking small samples from the sieved powder. This will allow for smarter decisions on the addition of fresh powder while taking less time to examine the powder by using processes that are already being conducted to reuse the powder.

2. Materials and methods

Printing was conducted on a 3D Systems DMP 200B SLM AM system (Rock Hill, SC, USA) using several different print settings. These prints were conducted during a

different study, where several different shapes were printed; however, the overall volume of the printed area was approximately the same. The Ti6Al4V (Ti64) powder was procured from AP&C (GE Additive, Cincinnati, Ohio, USA) with a size range of 15 μm to 45 μm. Powders were collected after each print and weighed before sieving. The powder was then sieved and weighed again to determine the amount that could be reused in the next print. The mesh size used for sieving was a 230 mesh in a 200 mm round sieve. The sieving process was done by placing ~500 g of powder in the sieve and then sieving for 10 min. This was done after every print, with the used powder being passed through the sieve once before using the powder to print again. This sieving process could have been adjusted with a 325 mesh size to maintain the large particles at 45 μm as they were received from the manufacturer, instead of letting the larger particles through with the 230 mesh. Five prints were run, and three states of the powder were examined. From the prints, two sets of parts were examined, and the microhardness of the parts was determined, as no print ran for the final powder state. From the powder, samples were taken from the as-purchased fresh, 3-use, and 5-use powders, with only the as-purchased powder for the new sample being examined. Imaging of the used and virgin powder was performed using a field-emission scanning electron microscope (FESEM; FEI Siron, Portland, USA) for both the >63 μm and <63 μm powder collected after each print. The images were then used to evaluate the percentage of defects in the <63 μm and virgin powder. The defective particles were separated into two groups, with one being the misshapen particles and the other being the particles that were welded together. Misshapen particles were determined by whether the particles were no longer spherical. For the welded particles, they were determined by whether the particles were two or more conjoined particles with a minimum size of 5 μm. Hardness was measured using a Phase II Plus Micro Vickers Hardness Tester (Phase II Plus, USA) on a ground and polished section of a part from the four prints. Imaging of the microstructure for examining the porosity of printed samples was performed using a Keyence 6000 series optical microscope (Keyence, Itasca, IL, USA) on the ground and polished surface of the samples. MATLAB was used for analyzing the scanning electron microscopy (SEM) imaging of the <63 μm powder size distribution. A piece of equipment with a metal funnel, platform, and a mounted protractor was used to determine the angle of repose of the powder.

3. Results and discussion

3.1. Ti64 powder analysis

Defect characterization, conducted using SEM, MATLAB, and manual counting, revealed the presence of defects in all three stages of the powder, with an increasing number of defects in the higher stages of use, despite the use of sieving on the recollected powder. Hand counting of the particles revealed a rapidly increasing number of defects in the powder that made it through the sieve, as the size of the defects was still small enough to pass through the sieve.

These defective particles are displayed in Figure 1A-C, even in the new powder supplied by the manufacturer. This can be due to the difficulty during the manufacturing process in achieving completely spherical particles. During the manufacturing process, as the molten spheres of metal are being cooled, collisions can occur, leading to defects in the new powder. Most of the defects would be caught if they end up being larger than the mesh size of the sieve. However, the defective particles that are smaller than the upper bound of the mesh could cause flowability issues. In Figure 1A, the displayed powder contains some small defects with an average of the percentage of the particles that are defective from a relatively spherical shape, and no welded particles gave a value of 8.8 ± 0.9% defective particles over four SEM scans. This strategy for determining the percentage of defects was applied to the other two sets of powder, with all values for the percentage of defective particles in all three batches listed in the second column of Table 1. In the new powder, most defects originate from tiny particles that are welded onto larger particles, with fewer defects being caused by larger particles that are welded or misshapen during the manufacturing process. The 3-use powder in Figure 1B contains less of the much smaller particles welded to larger particles and instead is primarily composed of misshapen particles with a higher proportion of particles that are of the same size being conjoined to each other, with the average amount of defects in the 3-use powder being approximately 6.4% higher than that of the new powder. The five powders in Figure 1C contain an even higher amount of the conjoined particles, with the average size of the particles being larger than the prior sets of powder. The percentage of particles with defects in the 5-use powder set was 10.6% higher than that of the new powder. This increase in defects could have been reduced by using a sieve size of approximately 45 μm, which is the high end of the initial distribution from the factory. These

Table 1. Characterization of powder samples and part hardness

Sample	Percentage of powder defects (%)	Percentage of recollected powder <63 μm (%)	Powder's distribution values D10, D50, D90 (μm)	Printed part's hardness (HV0.2)
New	8.8±0.9	100	13.5, 24.2, 38.9	396±41
3-Use	15.2±1.8	96.9±1.3	16.2, 26.7, 39.6	385±27
5-Use	19.4±3.3	<95	15.9, 31.3, 45	

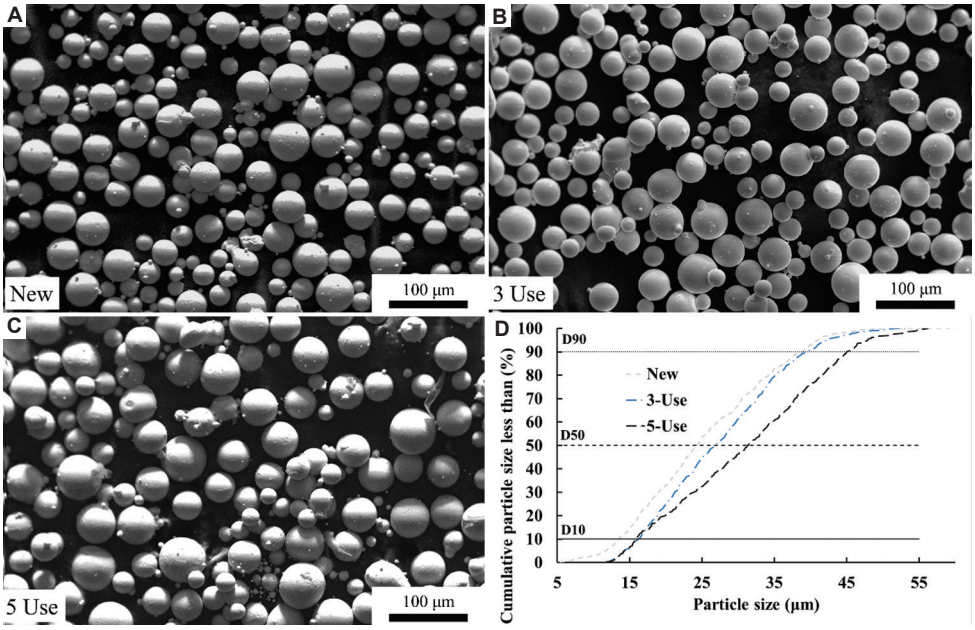

Figure 1. Sieved Ti64 powder SEM images at 200× magnification and a cumulative particle size distribution chart. (A) New as-purchased Ti64 powder. (B) 3-use Ti64 powder after sieving. (C) 5-use Ti64 powder after sieving. (D) A chart of the percentage of particles that are less than the values of particle sizes.

types of defective particles have been observed by Dai *et al.*, Jandaghi *et al.*, Moghimian *et al.*, and Ghods *et al.*[35-38]

The distribution of the new, 3-use, and 5-use powders can be interpolated from the plot in Figure 1D, which displays the percentage of particles within a specific particle size range. It also shows that there is a considerable difference in the particle sizes of the three powder types at the D10, D50, and D90 distributions, with the values listed in the fourth column of Table 1. At the D10 line, the new powder has the smallest particle size, with a lower initial slope and a higher number of particles below the initial sizes of either of the two used powders. The D10 values for the used powders were ~3 µm greater than those for the new powder. At the middle of the range with the D50 values was the largest difference in the sizes of the powder, with there being an increase of 3–4 µm going from the new to the 3-use and then 5-use powder. At the end of the range of particle sizes, at the D90 line, the new and 3-use powder have similar values, while the 5-use powder increases by ~5.5 µm. These increases in values correspond to the particle sizes of the used powders compared to the new powder, with an increase in defects in the used powders compared to the new powder.

These defects are significantly reduced in the powder through the use of sieving. Following completion of each print, there was an increase in the amount of powder that ended up being sieved out of the recollected powder. This value increased by approximately one percent after each print, with each batch of powder exhibiting an increasing number of defects, as indicated by a few values in the third column of Table 1. In large prints, around 5 kg of powder can be loaded, amounting to as much as 250 g being thrown away after just the fifth print, not including the prior prints, depending on the size of the parts being printed. The amount of powder rejected after sieving would likely continue to increase as the number of defects in the powder used increases, leading to more particles ending up in the larger size range and resulting in more particles being ≥63 µm after the next print. Figures 2A and 2B compares the new powder with the powder that failed to pass through the sieve. The particles that are rejected can be seen in Figure 2B, where all particles are welded together, with many particles being significantly larger than the sieve size and the maximum size of the new powder, as shown on the left portion of Figure 2A. In the rejected powder, the particles consist of two main categories. The first is smaller particles that have been welded to each other, such that they form a cluster of particles, and the second category is particles that have been enveloped by multiple particles, increasing the size of the particle while still maintaining a mostly spherical appearance of the particles. Depending on the flowability of the rejected powder for the LPBF process, it may still be usable in other processes or recycled into usable powder.

The powders' flowability was tested resulting in the chart in Figure 3A using the equipment in Figure 3B, revealing something interesting. Each of the powders was tested five times, filling the funnel halfway and allowing the excess

to flow off the edge of the platform. The new powder had the highest angle of repose at 27.8 ± 1°, while the two used powders had lower angles of repose at 24.6 ± 1° and 25.6 ± 0.4° for 3-use and 5-use powders, respectively, as displayed in Figure 3A. These values show that the new powder has slightly less flowability than the used powder. This could be due to the change in particle size, primarily the increase in all sizes across the powder distribution range, and the disappearance of very small particles in the used powders. This disappearance of the small particles in the used powders could be the cause of the lower angle of repose, with the lack of small particles to fill the voids between the larger particles, thus leaving gaps between particles that allow the larger particles to continue to move and flow better while having a lower packing density. This does end up with better flowability, but it could be speculated that the powder will have a worse packing density, leading to higher amounts of defects in the finished part.

3.2. Printed part quality and microhardness

The part quality was determined by examining the ground and polished sections of a part from each print. These sections were examined for defects in the parts; the representative defects are displayed in Figure 4. These parts displayed lack-of-fusion pores in all samples with the new powder, resulting in very few defects. In contrast, the 3-use powder resulted in a greater lack of fusion pores, as indicated by the dark pores in Figure 4B. For the new powder parts, there were very few pores across the entire polished surface, whereas the parts printed with the 3-use powder had more lack-of-fusion porosity. These are due to the increasing particle size and the lack of small powders (<10 μm) in the used powder, leading to a lower packing density and, ultimately, an increase in the lack-of-fusion defects. Although it has been demonstrated by Alamos *et al.*,[39] that there is no noticeable change in the fatigue life of reused Ti64 powder, our results do not support such conclusions and need more careful studies to fully understand the influence of these porosities on the static and dynamic mechanical properties of AM-processed Ti64 parts.[40,41]

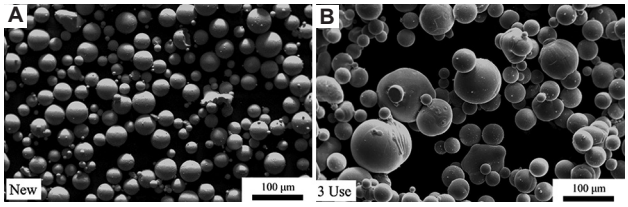

Figure 2. New Ti64 powder and the rejected powder from the 3-use powder were imaged with an SEM at 200× magnification. (A) New as-purchased powder. (B) Rejected 3-use powder.

The hardness of the parts was also tested. The values for the two parts tested, as shown in the fifth column of Table 1, reveal no noticeable differences between the parts despite the change in color of the used powders, which is due to a slightly higher number of oxidized particles resulting from the increase in defects. Although this increase in the number of oxidized particles did not affect the hardness, it has been shown that the increased oxidation does have an effect on the embrittlement, as demonstrated by Meier *et al.*,[42] though it could be another reason for the increased number of lack-of-fusion pores in the printed parts.

Our results indicate that standard tests like hardness measurements may not be appropriate to measure the part

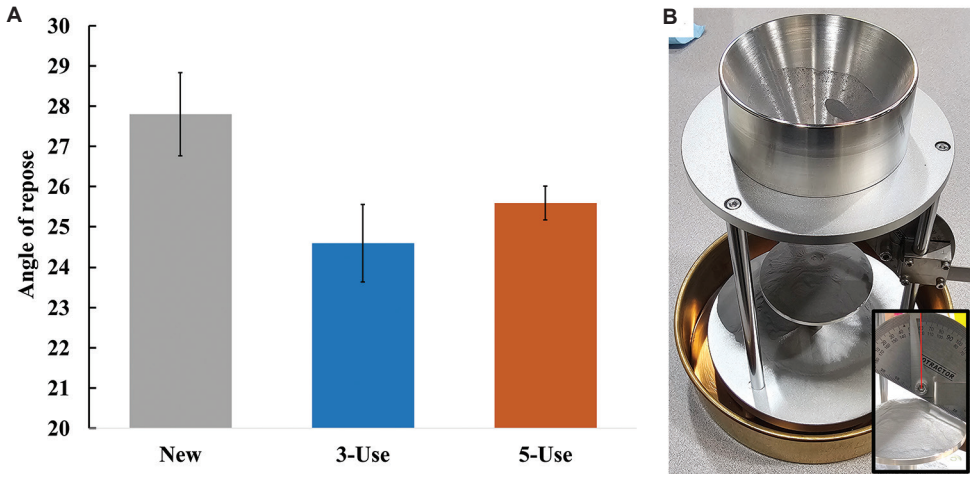

Figure 3. Angle of repose data and testing equipment used for Ti64 powder. (A) Angle of repose for the three powder conditions (n=5). (B) The overall setup for the testing, with an inset showing a measurement being taken at 60° on the protractor, resulting in an angle of repose of 30°.

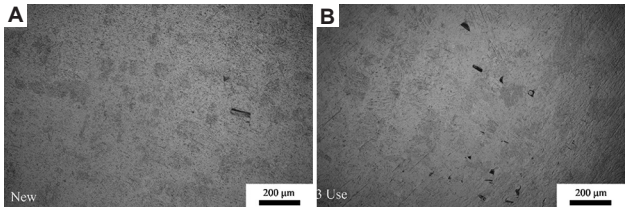

Figure 4. Optical microscope imaging of the ground and polished surfaces of the printed parts. (A) Part printed from the new powder. (B) Part printed from the 3-use powder.

quality in the LPBF process when powders are being reused. Powder flowability can change along with the powder particle size distribution due to the heat flux resulting from laser heating during printing. In our study, about 2% of the powders were found to be unusable after each print run. However, this number depends on the powder chemistry, the area of the print-bed used for printing parts, and the volume of unused powder, as compared to the used ones. Finally, the duration of the print will also impact the unused powder quality, where longer prints will have a higher chance of rejected powders.

4. Conclusion

In this study, the effect on Ti6Al4V powder during the LPBF process was examined at three points during five prints with the same powder. Over the five prints, the percentage of defective powder particles increased by ~11%. Each print resulted in ~1.5% less powder being reusable, which was discovered through the sieving process. The angle of repose of reusable powder improved by ~2°, resulting in improved flowability. Parts printed with used powder contained higher amounts of lack-of-fusion porosity. The density of parts was within a range of >98%. There was no change to the microhardness of finished parts with the reused powder. Our results showed that the occurrence of defects correlates with the weight fraction of the powder passing through the sieves, providing a simpler means of assessing powder quality for the LPBF process.

Acknowledgments

None.

Funding

The authors would like to acknowledge financial support from the National Institute of Arthritis and Musculoskeletal and Skin Diseases under Grant Number R01 AR078241. The content is solely the authors' responsibility and does not necessarily represent the National Institutes of Health's official views.

Conflict of interest

The authors declare that they have no competing interests.

Author contributions

Conceptualization: Amit Bandyopadhyay
Formal analysis: Nathaniel W. Zuckschwerdt
Investigation: Nathaniel W. Zuckschwerdt
Methodology: All authors
Writing–original draft: Nathaniel W. Zuckschwerdt
Writing–review & editing: Amit Bandyopadhyay

Ethics approval and consent to participate

Not applicable.

Consent for publication

Not applicable.

Availability of data

Data will be made available on reasonable request to the corresponding author.

References

1. Bandyopadhyay A, Heer B. Additive manufacturing of multi-material structures. *Mater Sci Eng Rep.* 2018;129:1-16.

   doi: 10.1016/j.mser.2018.04.001

2. Bandyopadhyay A, Ghosh S, Boccaccini AR, Bose S. 3D printing of biomedical materials and devices. *J Mater Res.* 2021;36(19):3713-3724.

   doi: 10.1557/s43578-021-00407-y

3. Bandyopadhyay A, Ciliveri S, Guariento S, Zuckschwerdt N, Hogg WW. Fatigue behavior of additively manufactured Ti3Al2V alloy. *Mater Sci Addit Manuf*. 2023;2(3):1705.

   doi: 10.36922/msam.1705

4. Pasang T, Budiman AS, Wang JC, *et al*. Additive manufacturing of titanium alloys - enabling re-manufacturing of aerospace and biomedical components. *Microelectron Eng*. 2023;270:111935.

   doi: 10.1016/j.mee.2022.111935

5. Alammar A, Kois JC, Revilla-León M, Att W. Additive manufacturing technologies: Current status and future perspectives. *J Prosthodont*. 2022;31:4-12.

   doi: 10.1111/jopr.13477

6. Xiong Y, Tang Y, Zhou Q, Ma Y, Rosen DW. Intelligent additive manufacturing and design: State of the art and future perspectives. *Addit Manuf*. 2022;59:103139.

   doi: 10.1016/j.addma.2022.103139

7. Gruber H, Henriksson M, Hryha E, Nyborg L. Effect of powder recycling in electron beam melting on the surface

chemistry of alloy 718 powder. *Metall Mater Trans A Phys Metall Mater Sci*. 2019;50(9):4410-4422.

doi: 10.1007/s11661-019-05333-7

8. Gorji NE, Saxena P, Corfield M, *et al*. A new method for assessing the recyclability of powders within powder bed fusion process. *Mater Charact*. 2020;161:110167.

doi: 10.1016/j.matchar.2020.110167

9. Sun P, Fang ZZ, Zhang Y, Xia Y. Review of the methods for production of spherical ti and ti alloy powder. *JOM*. 2017;69(10):1853-1860.

doi: 10.1007/s11837-017-2513-5

10. Garboczi EJ, Hrabe N. Particle shape and size analysis for metal powders used for additive manufacturing: Technique description and application to two gas-atomized and plasma-atomized Ti64 powders. *Addit Manuf*. 2020;31:100965.

doi: 10.1016/j.addma.2019.100965

11. Strondl A, Lyckfeldt O, Brodin H, Ackelid U. Characterization and control of powder properties for additive manufacturing. *JOM*. 2015;67(3):549-554.

doi: 10.1007/s11837-015-1304-0

12. Douglas R, Barnard N, Lavery N, Sullivan J, Jones T, Lancaster R. The effect of powder recycling on the mechanical performance of laser powder bed fused stainless steel 316L. *Addit Manuf*. 2024;88:104245.

doi: 10.1016/j.addma.2024.104245

13. Joju J, Verdi D, Han WS, *et al*. Sustainability assessment of feedstock powder reuse for directed laser deposition. *J Clean Prod*. 2023;388:136005.

doi: 10.1016/j.jclepro.2023.136005

14. Terrassa KL, Haley JC, MacDonald BE, Schoenung JM. Reuse of powder feedstock for directed energy deposition. *Powder Technol*. 2018;338:819-829.

doi: 10.1016/j.powtec.2018.07.065

15. Ferreira BT, Monteiro J, Borille A, Leite M, Ribeiro I. Reuse powder impacts in additive manufacturing for aeronautical parts. *Int J Adv Manuf Technol*. 2025;141:2067-2062.

doi: 10.1007/s00170-025-16619-z

16. Koushik T, Shen H, Kan WH, *et al*. Effective Ti-6Al-4V powder recycling in LPBF additive manufacturing considering powder history. *Sustain (Switzerland)*. 2023;15(21):15582.

doi: 10.3390/su152115582

17. Ochs D, Wehnert KK, Hartmann J, Schiffler A, Schmitt J. Sustainable aspects of a metal printing process chain with laser powder bed fusion (LPBF). In: *Procedia CIRP*. Vol. 98. Netherlands: Elsevier B.V.; 2021. p. 613-618.

doi: 10.1016/j.procir.2021.01.163

18. Fredriksson C. Sustainability of metal powder additive manufacturing. In: *Procedia Manufacturing*. Vol. 33. Netherlands: Elsevier B.V.; 2019. p. 139-144.

doi: 10.1016/j.promfg.2019.04.018

19. Cacace S, Furlan V, Sorci R, Semeraro Q, Boccadoro M. Using recycled material to produce gas-atomized metal powders for additive manufacturing processes. *J Clean Prod*. 2020;268:122218.

doi: 10.1016/j.jclepro.2020.122218

20. Ahmed F, Ali U, Sarker D, *et al*. Study of powder recycling and its effect on printed parts during laser powder-bed fusion of 17-4 PH stainless steel. *J Mater Process Technol*. 2020;278:116522.

doi: 10.1016/j.jmatprotec.2019.116522

21. Ren P, Ouyang Y, Mu J, *et al*. Metal powder atomization preparation, modification, and reuse for additive manufacturing: A review. *Prog Mater Sci*. 2025;152:101449.

doi: 10.1016/j.pmatsci.2025.101449

22. Arrizubieta JI, Ukar O, Ostolaza M, Mugica A. Study of the environmental implications of using metal powder in additive manufacturing and its handling. *Metals (Basel)*. 2020;10(2):261.

doi: 10.3390/met10020261

23. Ciliveri S, Bandyopadhyay A. Understanding the influence of alloying elements on the print quality of powder bed fusion-based metal additive manufacturing: Ta and Cu addition to Ti alloy. *Virtual Phys Prototyp*. 2023;18(1):e2248464.

doi: 10.1080/17452759.2023.2248464

24. Bandyopadhyay A, Mitra I, Ciliveri S, *et al*. Additively manufactured Ti-Ta-Cu alloys for the next-generation load-bearing implants. *Int J Extrem Manuf*. 2024;6(1):015503.

doi: 10.1088/2631-7990/ad07e7

25. Powell D, Rennie AEW, Geekie L, Burns N. Understanding powder degradation in metal additive manufacturing to allow the upcycling of recycled powders. *J Clean Prod*. 2020;268:122077.

doi: 10.1016/j.jclepro.2020.122077

26. Alamos FJ, Schiltz J, Kozlovsky K, *et al*. Effect of powder reuse on mechanical properties of Ti-6Al-4V produced through selective laser melting. *Int J Refract Metals Hard Mater*. 2020;91:105273.

doi: 10.1016/j.ijrmhm.2020.105273

27. Li X, Zhou M, Peng S, *et al*. Revealing effects of powder reuse for LPBF-fabricated NiTi shape memory alloys. *Front Mater Sci*. 2024;18(4):240697.

doi: 10.1007/s11706-024-0697-5

28. Gaillard GC, Courtois K, Sultan T, *et al*. Impact of Powders Reuse in LPBF Processes on the Powder Characteristics and

Samples Mechanical Properties. In: *Euro PM2020 - European Powder Metallurgy Conference*; 2020. Available from: https://www.cm/cea.hal.science/cea-04789655v1 [Last accessed on 2025 Oct 31].

29. Cordova L, Sithole C, Macía Rodríguez E, Gibson I, Campos M. Impact of powder reusability on batch repeatability of Ti6Al4V ELI for PBF-LB industrial production. *Powder Metall*. 2023;66(2):129-138.

    doi: 10.1080/00325899.2022.2133357

30. Smolina I, Gruber K, Pawlak A, *et al*. Influence of the AlSi7Mg0.6 aluminium alloy powder reuse on the quality and mechanical properties of LPBF samples. *Materials*. 2022;15(14):5019.

    doi: 10.3390/ma15145019

31. Gruber K, Smolina I, Kasprowicz M, Kurzynowski T. Evaluation of inconel 718 metallic powder to optimize the reuse of powder and to improve the performance and sustainability of the laser powder bed fusion (Lpbf) process. *Materials (Basel)*. 2021;14(6):1538.

    doi: 10.3390/ma14061538

32. Cordova L, Bor T, De Smit M, Carmignato S, Campos M, Tinga T. Effects of powder reuse on the microstructure and mechanical behaviour of Al-Mg-Sc-Zr alloy processed by laser powder bed fusion (LPBF). *Addit Manuf*. 2020;36:101625.

    doi: 10.1016/j.addma.2020.101625

33. Huang T, Sitt Thu K, Zhang Z, *et al*. Assessing the impact of top-up powder reuse strategy on MS1 powder characteristics and L-PBF printed part properties. *Metals (Basel)*. 2025;15(2):181.

    doi: 10.3390/met15020181

34. Weiss C, Haefner CL, Munk J. On the influence of AlSi10Mg powder recycling behavior in the LPBF process and consequences for mechanical properties. *JOM*. 2022;74(3):1188-1199.

    doi: 10.1007/s11837-021-05080-4

35. Dai Z, Chen X, Liu Y, Wang J, Lu J, Liu J. Effect of reuse on Cu-Cr-Nb powder and bulks produced by laser powder bed fusion. *Powder Technol*. 2025;457:120930.

    doi: 10.1016/j.powtec.2025.120930

36. Jandaghi MR, Moverare J. Exploring the efficiency of powder reusing as a sustainable approach for powder bed additive manufacturing of 316L stainless steel. *Mater Des*. 2024;244:113222.

    doi: 10.1016/j.matdes.2024.113222

37. Moghimian P, Poirié T, Habibnejad-Korayem M, *et al*. Metal powders in additive manufacturing: A review on reusability and recyclability of common titanium, nickel and aluminum alloys. *Addit Manuf*. 2021;43:102017.

    doi: 10.1016/j.addma.2021.102017

38. Ghods S, Schultz E, Wisdom C, *et al*. Electron beam additive manufacturing of Ti6Al4V: Evolution of powder morphology and part microstructure with powder reuse. *Materialia (Oxf)*. 2020;9:100631.

    doi: 10.1016/j.mtla.2020.100631

39. Alamos FJ, Schiltz J, Attardo R, *et al*. Effect of powder reuse on orthopedic metals produced through selective laser sintering. *Manuf Lett*. 2022;31:40-44.

    doi: 10.1016/j.mfglet.2021.06.002

40. Bandyopadhyay A, Traxel KD, Lang M, Juhasz M, Eliaz N, Bose S. Alloy design via additive manufacturing: Advantages, challenges, applications and perspectives. *Mater Today*. 2022;52:207-224.

    doi: 10.1016/j.mattod.2021.11.026

41. Traxel KD, Groden C, Valladares J, Bandyopadhyay A. Mechanical properties of additively manufactured variable lattice structures of Ti6Al4V. *Mater Sci Eng*. 2021;809:140925.

    doi: 10.1016/j.msea.2021.140925

42. Meier B, Warchomicka F, Ehgartner D, *et al*. Toward a sustainable laser powder bed fusion of Ti 6Al 4 V: Powder reuse and its effects on material properties during a single batch regime. *Sustain Mater Technol*. 2023;36:e00626.

    doi: 10.1016/j.susmat.2023.e00626

ACCSCIENCE PUBLISHING

Engineering Science in Additive Manufacturing

ORIGINAL RESEARCH ARTICLE

Effect of electroshock treatment on microstructure evolution of Ti-6Al-4V/Cu-Cr-Zr interface fabricated by laser melting deposition

Shiqiang Xie[1,2†], Changlin Huang[1,2†], Jiawei Gong[1,2], Pei Wang[1,2], Yan Wen[1,2*], and Lechun Xie[1,2*]

[1]State Key Laboratory of Light Superalloys, Wuhan University of Technology, Wuhan, Hubei, China

[2]Hubei Key Laboratory of Advanced Technology for Automotive Components, Wuhan University of Technology, Wuhan, Hubei, China

Abstract

This study aims to examine the effect of electroshock treatment (EST) on Ti-6Al-4V/Cu-Cr-Zr manufactured by laser melting deposition and explore the microstructure and mechanical properties to investigate the microstructure evolution of copper-based rail composite materials under high-energy-density currents. The results indicated that EST could promote atomic diffusion, enabling rapid preferential growth of TiCu in the metallurgical bonding zone. An increase of the current density promoted the nucleation of the primary Ti_2Cu phase induced by the thermal effect of EST, which led to Cu solute enrichment and composition undercooling. Moreover, EST significantly improved nucleation rate and grain boundary migration. The average β grain size of the EST-1 sample increased from 2.83 μm to 3.62 μm, approximately, while the typical basic texture of EST-1 was enhanced. In EST-1, the shear strength of Ti-6Al-4V/Cu-Cr-Zr was 132 MPa, which was 65% higher than that of the original Ti-6Al-4V/Cu-Cr-Zr composite. The improvement in shear strength can be attributed to intergranular nano-precipitation and the improved wettability of Ti-6Al-4V/Cu-Cr-Zr. This work provides valuable insights into the preparation of high-value, high-performance Cu-based composites.

Keywords: Electroshock treatment; Ti-6Al-4V/Cu-Cr-Zr interface; Microstructure evolution; Mechanical properties

†These authors contributed equally to this work.

***Corresponding authors:**
Yan Wen
(gubi2008@whut.edu.cn)
Lechun Xie
(xielechun@whut.edu.cn)

Citation: Xie S, Huang C, Gong J, Wang P, Wen Y, and Xie L. Effect of electroshock treatment on microstructure evolution of Ti-6Al-4V/Cu-Cr-Zr interface fabricated by laser melting deposition. *Eng Sci Add Manuf*. 2025;1(4):025430030.
doi: 10.36922/ESAM025430030

Received: October 21, 2025

1st revised: November 6, 2025

2nd revised: November 11, 2025

Accepted: November 12, 2025

Published online: November 28, 2025

1. Introduction

Maintaining high electrical conductivity of copper alloys while increasing surface hardness, heat resistance, and wear resistance can increase the service life of copper components.[1-5] At present, advanced surface strengthening techniques are widely employed in the preparation of reinforced layers on copper alloy surfaces to enhance their surface properties.[6-8] Laser melting deposition (LMD) is an advanced surface treatment technology, marked by high deposition efficiency, high surface accuracy, and a small heat-affected zone of the substrate.[9] Titanium alloys show characteristics, such as high hardness, high temperature resistance, and corrosion resistance. As a coating, it can significantly improve the surface performance of copper alloys.[10-12] In addition, Ti-6Al-4V has high strength and low electrical resistance, which can enhance the

strength of copper-based composites without causing a significant decrease in electrical conductivity.[13-15]

LMD enhances interfacial bond strength by promoting mixed diffusion of copper and coating material, while leading to significant amounts of copper entering the coating. As a result, there are limitations in terms of compatibility between the metal substrate and the cladding material. Other scholars have also conducted extensive research in this area. For instance, Li *et al.*[16] deposited AlCrFeNiMnx high-entropy alloy on a copper substrate and found that an increase in Mn improved the copper diffusion coefficient, facilitating diffusion of copper into the cladding layer and thus reducing the hardness of the cladding layer. By depositing CoCrNiFeTix high-entropy alloy on the copper alloy surface, Jia *et al.*[17] demonstrated that the hardness of the cladding layer increased with the addition of Ti content. CoCrW-xCu coatings with good metallurgical bonding were prepared by laser cladding by Dong *et al.*[18] Zhou *et al.*[19] achieved laser cladding of a gradient molybdenum coating on copper alloy surfaces. By adjusting process parameters, they obtained well-bonded, defect-free, and dense strengthening layers. Shear tests evaluated the bond strength, with maximum values reaching 240 MPa. The above-mentioned studies have all achieved effective strengthening of copper alloy surfaces, thereby enhancing their surface properties.

As a rapid post-processing technology, electroshock treatment (EST) optimizes the organizational structure of the material through the action of high current, offering a novel approach to enhancing material properties.[20] EST provides favorable conditions for analyzing the microstructure evolution of the bonding zone of the composite layer under high current density.[21-23] Fan *et al.*[24] investigated the effect of electrical pulse on the microstructure of spot welded joints of AA2198-T8 aluminum alloy. The interfacial defects of the welded joints were gradually reduced with the increase of the electrical pulse time. Liu *et al.*[25] explored the defect healing mechanism of 6061-T6 aluminum alloy under electrical pulse, and found that the current bypassing the holes would produce local current density increase and Joule heat effect around the holes, and the holes would be deformed and healed under the action of thermal compression stress. Qian *et al.*[26] performed EST on the interface of stainless steel joined in hot compression and found that EST promoted recrystallization at the interface and the formation of fine equiaxed crystal grains, which contributed to the healing of the interface. Taken together, EST induces the microstructure variation of the material, and such microstructural changes are closely related to the compression,[27] tensile,[28] and fatigue life of the material.[29,30]

However, no systematic studies have been reported on the microstructural evolution and texture effects of Ti-6Al-4V/Cu-Cr-Zr interfaces fabricated by LMD using EST. Therefore, in this study, we prepared Ti-6Al-4V/Cu-Cr-Zr by using LMD technology and investigated changes in microstructure and mechanical properties under high-energy-density current conditions. This research provides theoretical guidance and experimental support for enhancing the performance of copper-based composites.

2. Materials and methods

2.1. Materials preparation

In this work, a Cu-Cr-Zr alloy was used as the substrate, with its main composition shown in Table 1. The substrate sample dimensions were 43 mm × 32 mm × 7 mm. Five pieces of Cu-Cr-Zr material were prepared for LMD. Before the LMD experiments, the substrate underwent pre-treatment: First, surface oxide layers were removed by grinding with 600# and 1200# sandpaper. Subsequently, the Cu-Cr-Zr substrate surface underwent shot peening to reduce surface gloss and enhance surface roughness. In preliminary work, we thoroughly investigated the influence of surface roughness on the LMD coating properties under various shot peening parameters. Detailed comparisons of interface forming performance across six distinct *R*a values revealed that a coating with optimal forming characteristics was achieved at *R*a = 3.9 μm.[13] Consequently, all subsequent LMD experiments were conducted with a surface *R*a maintained at 3.9 μm. Finally, acetone cleaning was performed to remove oil contamination from the substrate surface, followed by ultrasonic cleaning with anhydrous ethanol to eliminate adhering contaminants and particulates. The substrate was dried and set aside for later use. Ti-6Al-4V powder with a particle size of 45–150 μm was selected as the coating material, with its main composition shown in Table 1. The powder exhibits a spherical morphology with excellent sphericity, with 80% of the particle size distribution ranging from 69 to 117 μm.[13] The coating was prepared via LMD in an argon atmosphere with oxygen content below 100 ppm, as illustrated in Figure 1A. LMD experiments were conducted using an LMD 16080 system (Nanjing Zhongke Raycham Laser Technology Co., Ltd., China), with a YLS-2000 laser source (IPG Photonics) operating at 1800 W. The powder feed rate

Table 1. Chemical composition of Cu-Cr-Zr substrate and Ti-6Al-4V powder (wt.%)

Materials	Cr	Zr	Cu	Al	V	C	N	O	Fe	Ti
Cu-Cr-Zr	1.03	0.11	Bal.	-	-	-	-	-	-	-
Ti-6Al-4V	-	-	-	6.2	4.15	0.01	0.015	0.15	0.056	Bal.

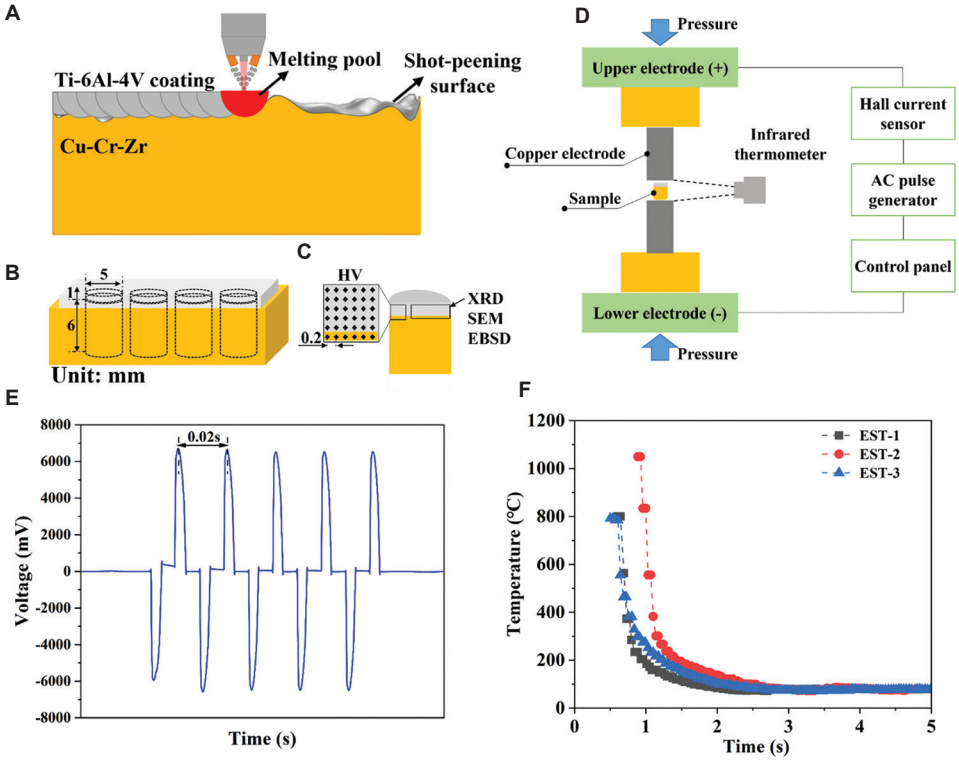

Figure 1. Schematic diagram of the experimental process. (A) Schematic of LMD; (B) schematic of EST; (C) schematic diagram of specimen preparation; (D) schematic of the microstructural characterization region; (E) EST pulse waveforms; (F) temperature changes after EST in Ti-6Al-4V/Cu-Cr-Zr (EST-0, EST-1, and EST-2 represent samples treated at different current densities, as shown in Table 2).
Abbreviations: AC: Alternating current; EBSD: Electron backscatter diffraction; EST: Electroshock treatment; LMD: Laser melting deposition; SEM: Scanning electron microscopy; XRD: X-ray diffraction.

was controlled at 6.9 g/min, and the scanning speed was set to 300 mm/min. Concurrently, the shielding gas flow was maintained at 25 L/min, and the powder delivery gas flow was 5 L/min. After sample preparation, the specimens were machined using an electrical discharge machining (EDM) device into cylinders with a diameter of 5 mm and a height of 7 mm for EST experiments (Figure 1B and C). To minimize the impact of EDM on EST experiments, the cut samples were polished using 600#, 1200#, and 4000# silicon carbide sandpaper to remove traces generated during the cutting process.

2.2. EST experimental procedure

Figure 1D illustrates a schematic of EST assembly, and the experimental apparatus includes an AC pulse generator, a Hall current sensor, and an infrared thermal imaging camera. From top to bottom, there are a removable copper upper electrode, a Ti-6Al-4V/Cu-Cr-Zr sample, and a copper lower electrode. AC pulses with the following parameters can be output: Peak current and pulse frequency. The output waveform is shown in Figure 1E. During the EST process, the sample temperature was monitored using an infrared thermal imager. The temperature rose to its peak within an extremely short time and subsequently cooled naturally in the air, with the temperature variation shown in Figure 1F. The EST time was 0.1 s with 5 pulses, and the experiment was carried out at different current densities. The samples with different current densities were named EST-1, EST-2, and EST-3, respectively, while the untreated sample was named EST-0, as shown in Table 2. For each set of EST parameters, five cylindrical specimens with a diameter of 5 mm were selected for machining. Subsequently, three specimens were chosen from each set for microstructural analysis and mechanical property testing. Both microstructure and mechanical properties

Table 2. EST parameter settings

Samples	Time (s)	Current density (A/mm²)
EST-0	0	0
EST-1	0.1	205
EST-2	0.1	262
EST-3	0.1	306

Abbreviation: EST: Electroshock treatment.

maintained a corresponding relationship to prevent random variations in the test results.

2.3. Microstructural characterization

Before microstructural characterization, cylindrical samples were sectioned using EDM. The sample surfaces were ground using 600#, 1200#, 2000#, and 4000# sandpaper. Subsequently, the observation surfaces were polished using a mixture of 0.04 μm SiO_2 suspension and H_2O_2 in a 3:2 volume ratio. Scanning electron microscopy (SEM; JSM-IT800, JEOL, Japan) was employed to analyze the coating and the microstructure of defects at the Ti-6Al-4V/Cu-Cr-Zr interface. Grain orientation characteristics were observed via electron backscatter diffraction (EBSD) and subsequently analyzed using AztecCrystal software (Oxford Instruments, UK). Simultaneously, the phase composition of the samples was characterized using X-ray diffraction (XRD) with Cu Kα radiation at 40 kV and 30 mA. The scan was performed with a step size of 0.025°, a scan speed to 1°/min, and a 2θ range of 30°–90°. The microstructure of the samples was characterized using SEM and EBSD. All microstructural characterization regions are shown in Figure 1C.

2.4. Mechanical properties

Microhardness testing was performed on samples before and after EST using a HUAYIN HV-1000A microhardness tester. To ensure measurement accuracy, a 6×6 square array of sampling points was employed, which were spaced 0.2 mm apart. The sampling point layout is shown in Figure 1C. A load of 200 g was applied with a dwell time of 10 s. Shear tests were conducted on an MTS C43 testing machine with a shear rate of 0.05 mm/min. Shear samples were prepared by splitting a cylindrical sample vertically into two equal halves, as illustrated in Figure 1C. The shear test fixture was designed according to the specimen to determine the shear strength of the coating.[13] Subsequently, the relevant shear strength was calculated based on the shear pressure and the specimen's cross-sectional area.

3. Results and discussion

3.1. Microstructure evolution of Ti-6Al-4V/Cu-Cr-Zr

To investigate the effect of EST on the Ti-6Al-4V/Cu-Cr-Zr interface, the microstructure of the metallurgical bonding zone (MBZ) was analyzed before and after EST treatment (as shown in Figure 2). The morphology of the MBZ revealed that the untreated interface exhibited a relatively flat state with minimal undulations, as depicted in Figure 2A-C. Following EST at different current densities, the MBZ formed a serrated profile at the Ti-6Al-4V interface. This bonding zone protruded toward the Ti-6Al-4V coating side and exhibited an embedded morphology (Figure 2E, F, H, I, K, and L). After EST, the MBZ exhibits a protrusion toward the Ti-6Al-4V side, manifesting as a distinct boundary line, as shown in Figure 2F, I and L. This indicates that the thermal effects of EST soften the Ti-6Al-4V coating. Under pressure, the coating undergoes plastic deformation, forming an embedded, serrated-like region.

The XRD characterization of the phase of Ti-6Al-4V coating before and after EST are shown in Figure 3. Before EST, there is no CuTi diffraction peak in the EST-0 in Figure 3A. CuTi diffraction peaks appeared in the Ti-6Al-4V coating after EST, as shown in Figure 3B-D. Meanwhile, the intensity of α phase diffraction underwent changes after EST, and the (002) crystal plane diffraction peaks disappeared for α-Ti in EST-1, as shown in Figure 3B. The intensity of (101) crystal plane diffraction peaks decreased after EST-2, as shown in Figure 3C. The intensity of the (002) and (101) crystal plane diffraction peaks of α-Ti increased in EST-3, as shown in Figure 3D. The variation in grain orientation is due to the phase transition induced by the thermal effect of EST.[31]

Figure 4A-D show the line scan results corresponding to Figure 2A, D, G, and J, respectively, indicating significant diffusion phenomena at the Ti-6Al-4V/Cu-Cr-Zr interface. The MBZ width without EST treatment was 27.4 μm (Figure 4A). After EST, the MBZ exhibited a widening trend, with MBZ widths of 50.2 μm, 43.6 μm, and 235.5 μm for the EST-1, EST-2, and EST-3 samples, respectively (Figure 4B-D). The elemental distribution curves in the MBZ exhibit a step-like pattern, indicating the formation of Cu-Ti intermetallic compounds in this region. Based on the atomic ratios of different elements within the MBZ, the presence of Cu_3Ti_2 and CuTi phases was confirmed. Following EST, the elemental concentrations in the MBZ region showed a gradual decrease, indicating diffusion of elements under the influence of EST. This phenomenon is attributed to the thermal effects of EST preferentially acting on high-energy interface regions.

The EST process generally occurs at temperatures above 800°C, while reaction $\beta Ti + Ti_2Cu \leftrightarrow \alpha Ti$ occurs at around 700°C, leading to precipitation of large amounts of αTi in the MBZ [32]. When the temperature reaches 950°C, the Ti-Cu alloy will melt to produce the liquid phase (Liquid, L), at which the reaction $L + Ti_2Cu \leftrightarrow \alpha Ti$ will occur, and when the temperature reaches about 965°C, the eutectic reaction of $L + Ti_2Cu \leftrightarrow CuTi$ will occur at the bonding zone. When the temperature continues to increase to 990°C, the precipitation of the Ti_2Cu phase occurs, $L + \beta Ti \leftrightarrow Ti_2Cu$. Based on the above reaction equations, when the thermal effect of EST on Ti-6Al-4V/

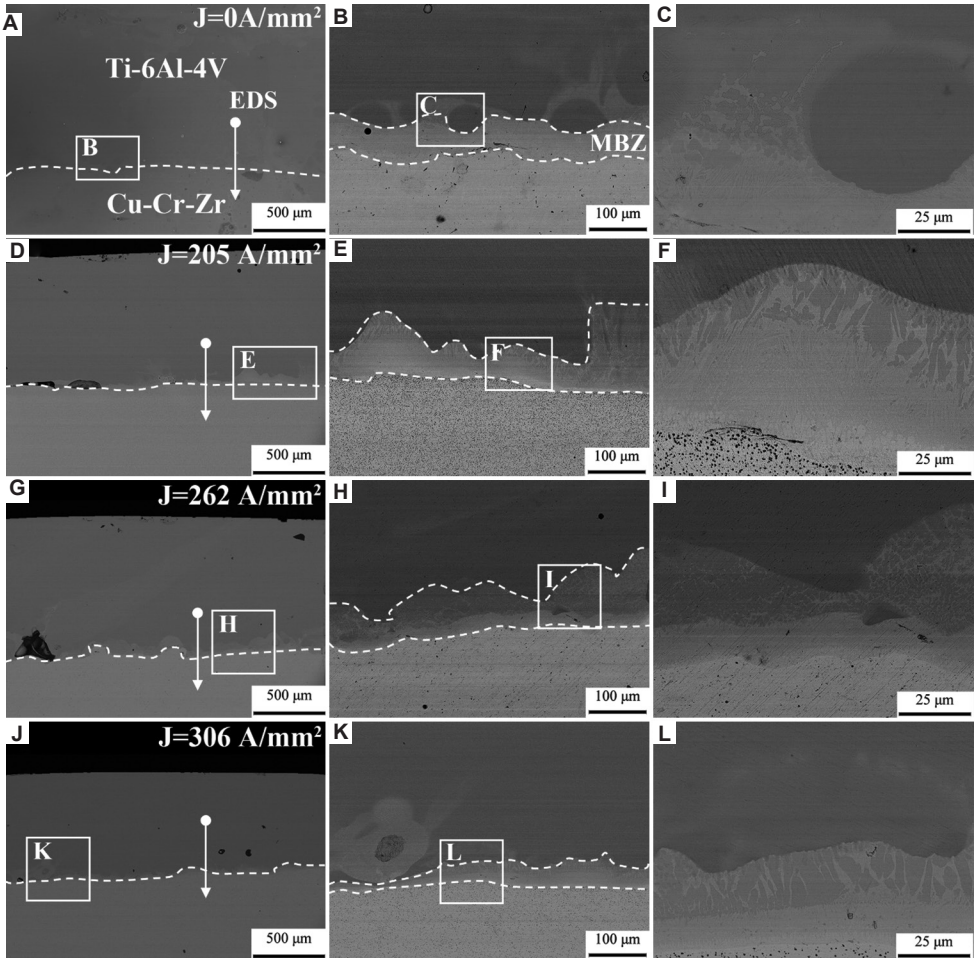

Figure 2. Interface microstructural morphology at different current densities. (A, D, G, J) microstructures of EST-0, EST-1, EST-2, and EST-3 at low magnification (×50); (B, E, H, K) microstructures of EST-0, EST-1, EST-2, and EST-3 at medium magnification (×200); (C, F, I, L) microstructures of EST-0, EST-1, EST-2, and EST-3 at high magnification (500×).
Abbreviation: EST: Electroshock treatment.

Cu-Cr-Zr is significant, the precipitation of CuTi may be accompanied by the formation of Ti_2Cu. Figure 5 shows the SEM analysis results of the precipitated phases in the MBZ region before and after EST. Figure 5A, D, G, and J depict the MBZ interface regions of the Ti-6Al-4V/Cu-Cr-Zr metal matrix composite before and after EST, respectively. Figure 5B, E, H, and K correspond to the region near the Ti-6Al-4V coating, while Figure 5C, F, I, and L correspond to the region near the Cu-Cr-Zr substrate. After EST at different current densities, precipitates primarily consisting of Ti_2Cu and CuTi formed in the MBZ, predominantly on the side adjacent to the Ti-6Al-4V coating, as seen in Figure 5E, H, and K. Based on the temperature-dependent reaction equation, the phase within the CuTi phase is Ti_2Cu. The Cu_4Ti phase near the Cu-Cr-Zr substrate underwent transformation, changing from an initial circular shape to an elliptical form, with its orientation shifting from disordered to ordered. These changes can be attributed to the influence of electric current, which induced morphological alterations in the Cu_4Ti phase.

Ti_2Cu is generated due to the thermal effect of EST, which causes Cu to diffuse into the Ti lattice by displacement diffusion.[33] A small amount of Ti_2Cu is also precipitated in the MBZ during LMD, causing the decomposition of $\alpha' \rightarrow \alpha + Ti_2Cu$ through the distribution of solute Cu.[34] The diffusion coefficient of Cu is expressed by the Arrhenius equation.[35]

$$D = D_0 \exp(-Q/RT) \quad (1)$$

Where D is the diffusion constant of solute atoms, D_0 is the diffusion constant, Q is the activation energy, R is the gas constant, and T is the temperature. Spherical particles of Ti_2Cu can enhance the ductility and processability of the alloy, whereas the acicular or lamellar particles significantly

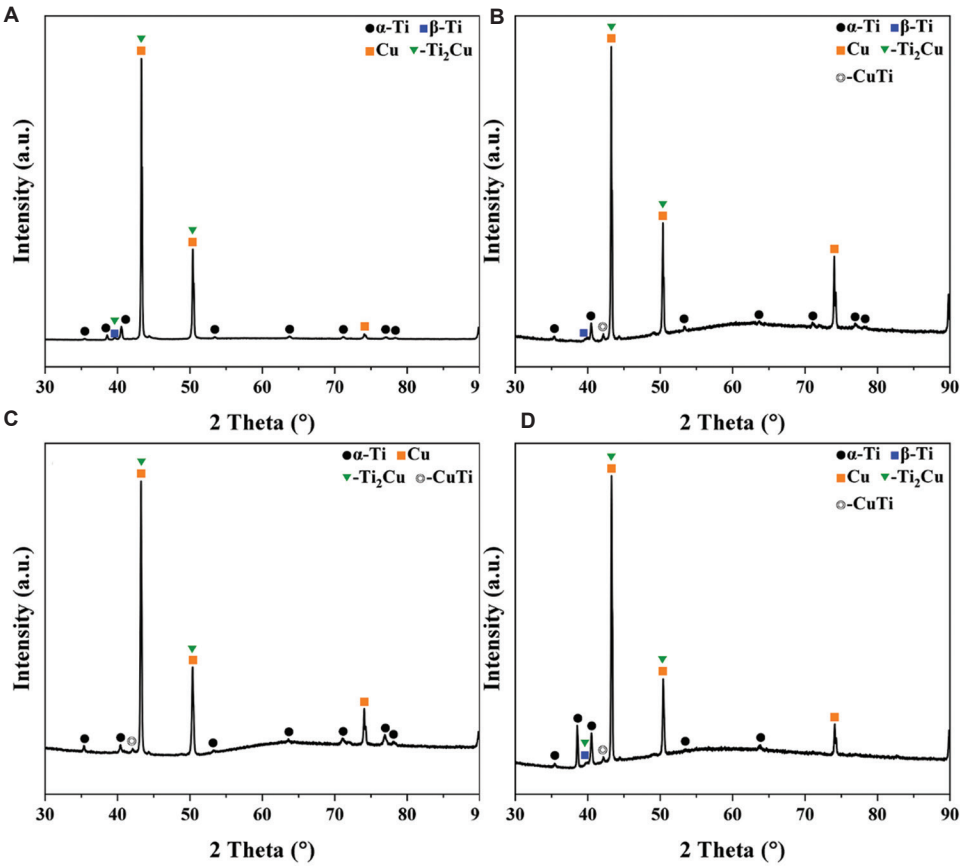

Figure 3. X-ray diffraction characterization results of Ti-6Al-4V coating before and after EST. (A) EST-0; (B) EST-1; (C) EST-2; (D) EST-3. Abbreviation: EST: Electroshock treatment.

enhance the strength of titanium alloys through the dislocation pinning effect, but they become brittle due to stress concentration. When the nucleation resistance is low during solidification or phase transformation, the particles tend to grow freely into spherical shape. When the nucleation resistance is high, the particles growth is limited, and it is easy to form an irregular interstitial structure or a finely dispersed phase. In addition, the reduction of interfacial resistance promotes the diffusion of atoms at the phase interface, inducing the formation of cavity vesicular Ti_2Cu.[36] According to the nucleation model, the driving force α for Ti_2Cu precipitation can be described as follows:[37]

$$\Delta G_m^{Ti_2Cu} = \Delta G_\gamma^{\alpha/Ti_2Cu} + \Delta G_S - \Delta G \quad (2)$$

Where ΔG_m is the molar driving force for Ti_2Cu precipitation, $\Delta G\gamma$ is the phase interface energy, ΔG_S is the strain energy of Ti_2Cu, and ΔG is the free energy of the system. Using the calculated driving force, the critical nucleation radius of Ti_2Cu can be estimated as follows: [38]

$$\gamma^* = \frac{2\Delta G_\gamma^{\alpha/Ti_2Cu} V_m^{Ti_2Cu}}{\Delta G_m^{\alpha/Ti_2Cu}} \quad (3)$$

Where V_m is the molar volume of Ti_2Cu. Equation 2 suggests that the formation of Ti_2Cu particles is governed by the nucleation barrier, which is mainly composed of the interfacial energy and the strain energy. To lower the nucleation barrier and reduce the nucleation drive of Ti_2Cu, it is necessary to optimize the interfacial structure to achieve this. This interfacial matching property is particularly critical in the early stages of nucleation, and by reducing the interfacial energy, the total nucleation barrier can be substantially weakened, allowing Ti_2Cu to form more easily.[33,36] Moreover, according to Equation 3, lower interfacial energy favors finer Ti_2Cu precipitation. The generation mechanism of the copper-rich phase of Ti_2Cu nanoparticles was revealed by the diffusion of solute copper during EST.

The shape of Cu_4Ti grains in the MBZ before EST presents an irregular morphology. After EST, the shape of Cu_4Ti

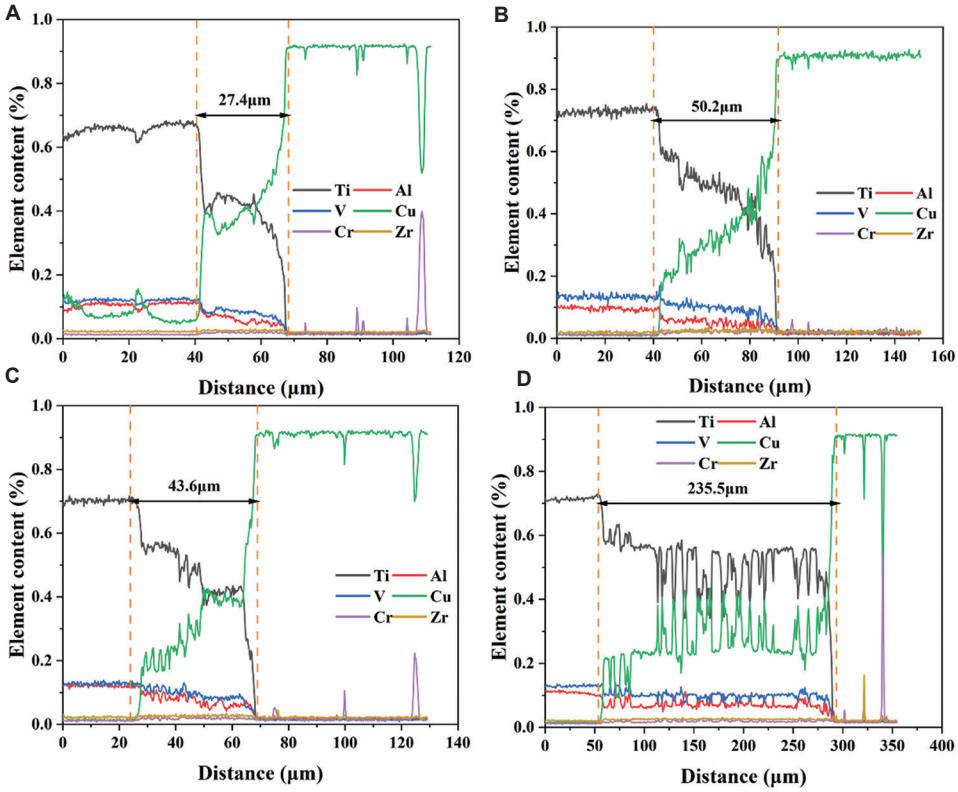

Figure 4. Elemental composition of metallurgical bonding zone at different current densities. (A) EST-0; (B) EST-1; (C) EST-2; (D) EST-3. Abbreviation: EST: Electroshock treatment.

presents an elliptical form. EST leads to the generation of a liquid phase at the Ti-6Al-4V/Cu-Cr-Zr interface, and the solute elements do not have enough time to diffuse during the non-equilibrium crystallization process. The thermal effect of EST is not significant on the Cu substrate, because the Cu substrate has good thermal conductivity and thus maintains a large degree of subcooling. Due to the effect of subcooling, the grains will grow along the subcooling direction during the growth process, which is because the subcooling direction provides more energy-driving force and makes the grains easier to grow in that direction.[39] The grains show elongation or directional growth in the subcooling direction.

3.2. Grain orientation and texture distribution

Figure 6 analyzes and displays the grain orientations of the α, β, and Cu phases in MBZ before and after EST treatment. Figure 6A shows the EST-0 sample, where the Cu phase grains in MBZ primarily exhibit orientation along the (101) direction. Figure 6B, E, H, and K show the distribution of grain boundaries in the Ti-6Al-4V/Cu-Cr-Zr hybrid zone before and after EST. Low-angle grain boundaries (LAGBs) ($2° \leq \theta \leq 15°$) are indicated by black lines, while high-angle grain boundaries (HAGBs) ($\theta \geq 15°$) are indicated by red lines. Before and after EST, Ti-6Al-4V coatings predominantly contained HAGBs with a small number of low-angle grain boundaries distributed throughout. Following EST, changes occurred in both LAGBs and HAGBs within the MBZ and Cu-Cr-Zr matrix. As shown in Figure 6B, LAGBs were primarily distributed within the MBZ. Following EST, LAGBs exhibited a trend of initial increase followed by a decrease, with the increase predominantly occurring in the Cu-Cr-Zr matrix, as shown in Figure 6E, H, and K.

As shown in Figure 7, MBZ primarily consists of the β phase. To characterize the changes in β grain size within MBZ before and after EST, the β grain sizes were statistically analyzed (as depicted in Figure 6C, F, I, and L). The d90 represents the cumulative frequency of the distribution histogram of 90%. The β grain size in the MBZ of the EST-0 sample was 2.83 μm. After EST, the β grains exhibited varying degrees of growth. The maximum increase reached 3.62 μm in the EST-1, while the minimum increase was 2.97 μm. The β grain size in the MBZ showed a significant increase trend after EST, resulting from the combined effects of thermal and non-thermal mechanisms provided by EST. In Ti-6Al-4V, the α phase (hexagonal close packed structure) is the low-temperature stable

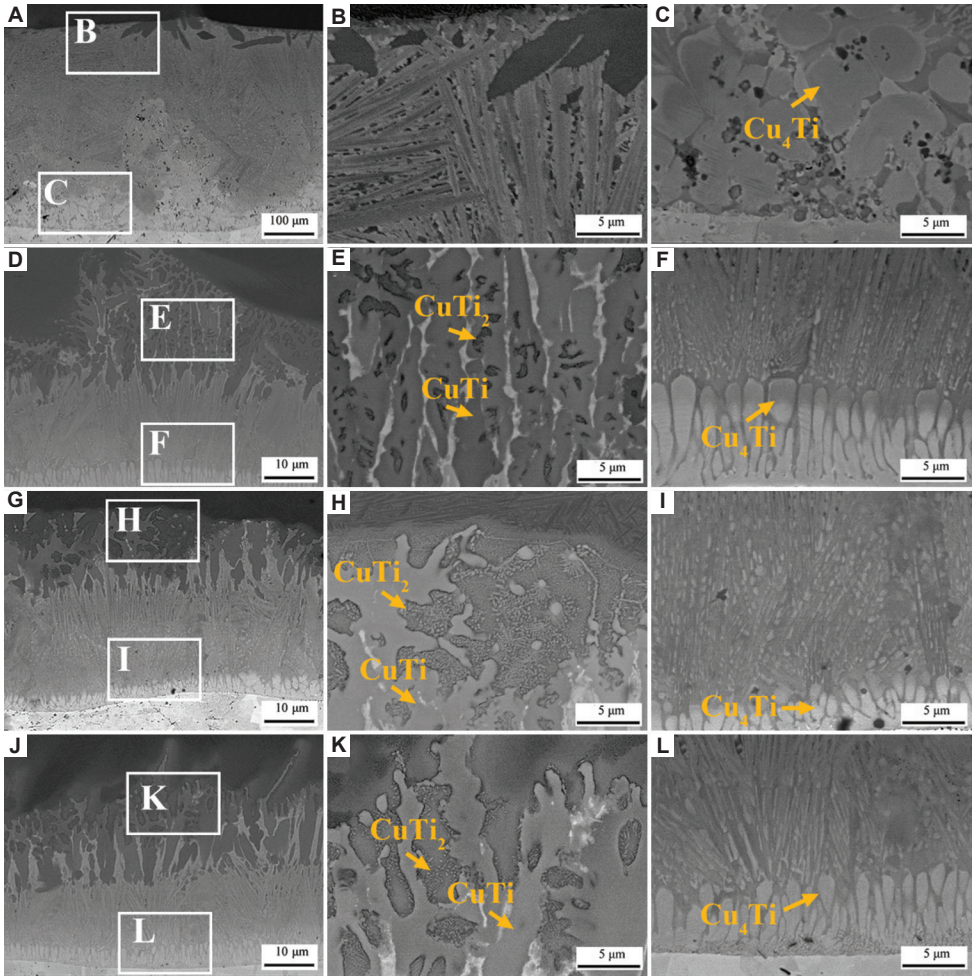

Figure 5. Scanning electron microscopy morphology of metallurgical bonding zone at different current densities. (A-C) EST-0; (D-F) EST-1; (G-I) EST-2; (J-L) EST-3.
Abbreviation: EST: Electroshock treatment.

phase, while the β phase (body-centered cubic structure) is the high-temperature stable phase. Under high-temperature conditions, the α phase dissolves into the β phase. The instantaneous high-energy pulse current of EST significantly accelerates this dissolution process. Once α phase particles are rapidly dissolved, β grain boundaries can migrate freely, leading to rapid grain growth.

The phase distribution in the MBZ before and after EST was characterized using EBSD (as shown in Figure 7A, D, G, and J). The MBZ primarily consists of β, interspersed with α and Cu phases. As depicted in Figure 7A for the ETS-0 sample, the β phase contains a significant amount of α phase, predominantly distributed near the Cu-Cr-Zr matrix side in a relatively dispersed manner. Following EST, the α phase near the Cu-Cr-Zr matrix transformed into β phase, as shown in Figure 7D, G, and J. This transformation resulted from the electromigration effect of the current, which drove atomic diffusion. The original α phase region adjacent to the interface became enriched with Cu. The Cu injection significantly lowered the stabilization temperature of the β phase within the MBZ, enabling stable β phase formation at lower temperatures. Conversely, more α phase appeared near the Ti-6Al-4V side. The primary reason for this phenomenon was the lower thermal conductivity of the Ti-6Al-4V alloy compared to Cu. This resulted in more pronounced heat accumulation adjacent to the Ti-6Al-4V interface, thereby initiating alterations in the phase constitution. In addition, a Cu phase appeared near the Ti-6Al-4V side. As Cu atoms continue migrating toward the Ti-6Al-4V side, the loss of β-stabilizing elements (Cu and V) induces the precipitation of the α phase within the β phase. Due to the low solubility of Cu in α phase, copper precipitates from α phase during its nucleation and growth, diffusing into the surrounding β phase and inhibiting the free growth of α phase. The growth of the eutectic α phase initially formed during the

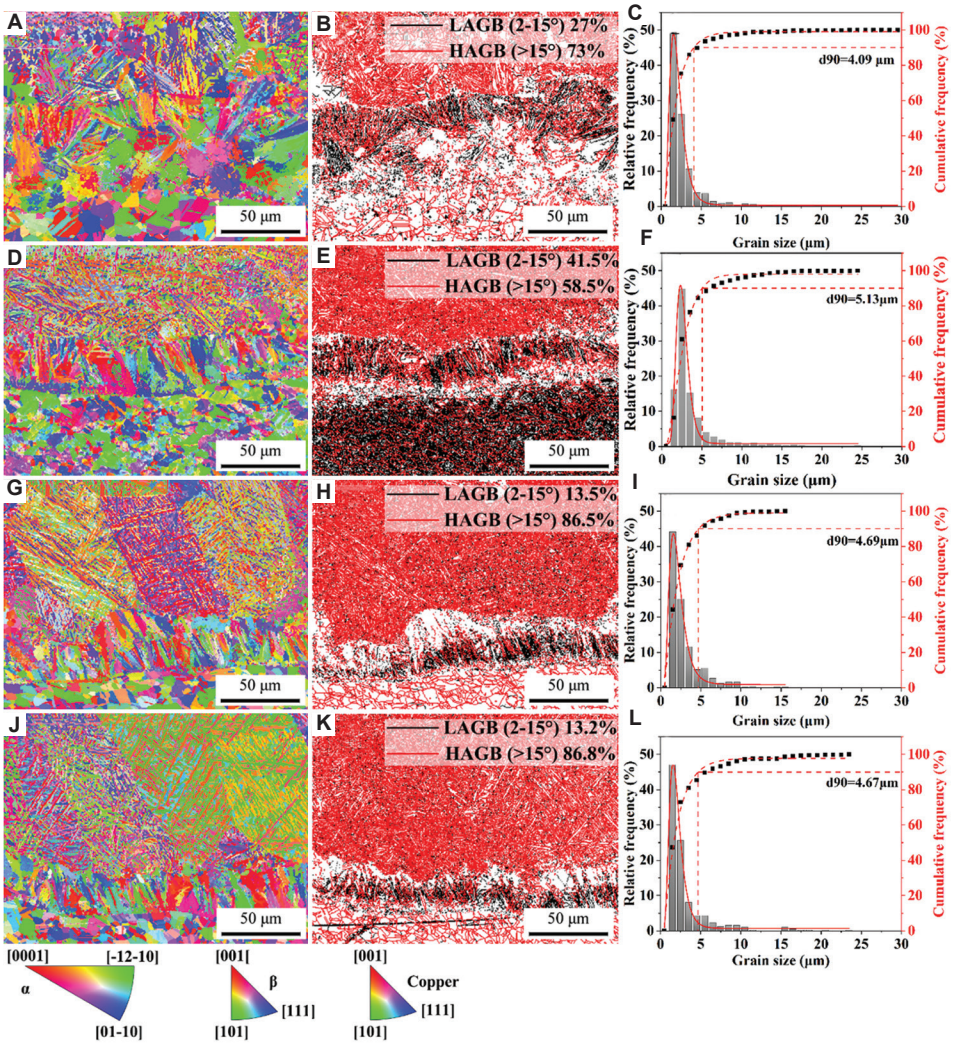

Figure 6. Grain orientation of the samples before and after EST: (A) EST-0; (D) EST-1; (G) EST-2; (J) EST-3. Distribution of Ti-6Al-4V/Cu-Cr-Zr grain boundaries before and after EST: (B) EST-0; (E) EST-1; (H) EST-2; (K) EST-3. MBZ β grain size before and after EST: (C) EST-0; (F) EST-1; (I) EST-2; (L) EST-3.

Abbreviations: EST: Electroshock treatment; HAGB: High-angle grain boundary; LAGB: Low-angle grain boundary; MBZ: Metallurgical bonding zone.

phase transformation is constrained only by the initial β phase grain boundaries and exhibits larger dimensions.

Figures 6E, 6H, 6K and 7B display the kernel average misorientation (KAM) maps of Ti-6Al-4V/Cu-Cr-Zr. The average KAM value of the EST-0 sample was 0.66°. Following EST, the average KAM values of all samples increased, with EST-1 exhibiting the greatest improvement, which achieved an average KAM value of 1.37°. Following EST, the average KAM value of the Ti-6Al-4V/Cu-Cr-Zr material increased significantly, with its dislocation density rising by at least 7.58% compared to the untreated specimens. Under the thermal effects of EST, significant intergranular interactions occur, pinning and entangling dislocations to promote recrystallization. During recrystallization, LAGB undergoes entanglement, slip, and climb mechanisms, increasing lattice distortion and dislocation density within the MBZ.

The rapid temperature increases and cooling rate under EST promotes the α+β phase transition. When the β phase transforms into α phase, there is a clear Burgers orientation relationship. This relationship determines the cubic β phase and hexagonal α/α' phase transformations as follows: {110}β//{0001}α/α', <111>β//<11-20>α/α'.[40] The orientation distribution is shown in Figure 8. The EST-0 specimen contains {-23-11} and {-3121} textures, with {-23-11} being the dominant texture exhibiting a maximum texture strength of 7.47, as depicted in Figure 8A. Following EST, the texture and intensity underwent changes. After

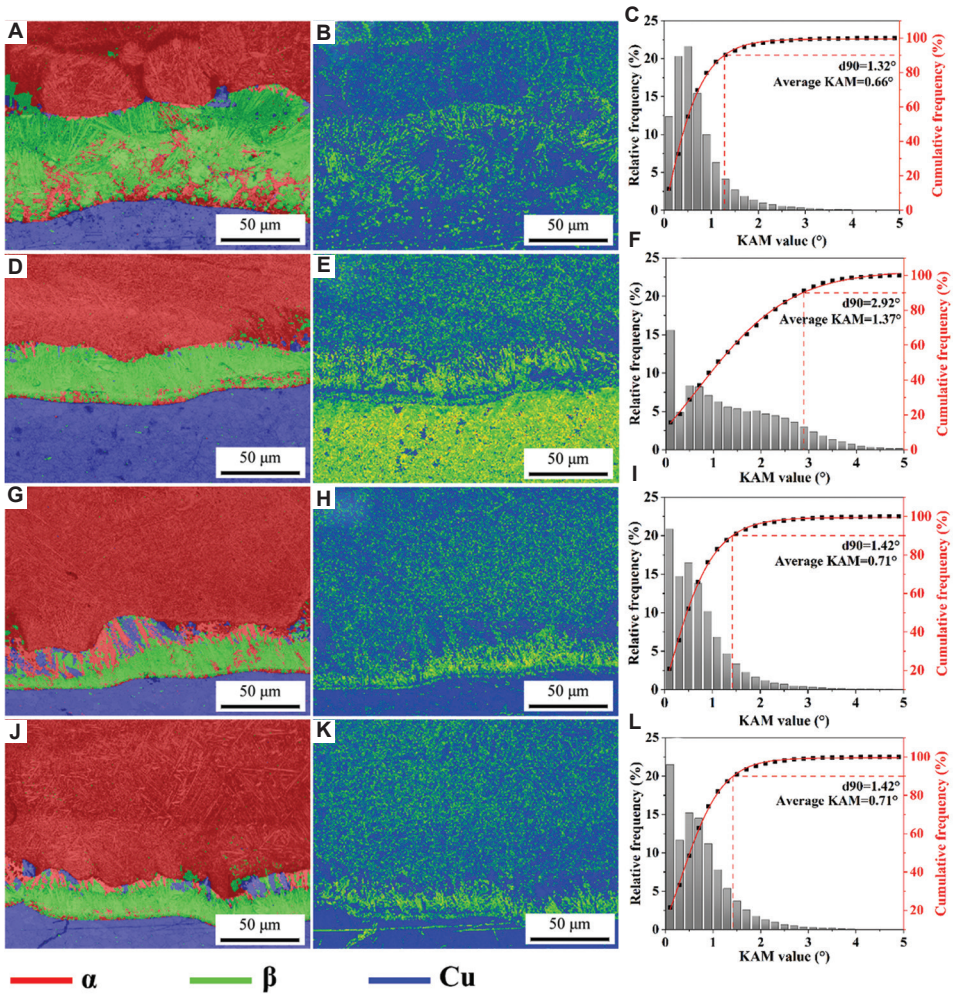

Figure 7. MBZ phase distribution: (A) EST-0; (D) EST-1; (G) EST-2; (J) EST-3. KAM distribution maps of Ti-6Al-4V/Cu-Cr-Zr before and after EST: (B) EST-0; (E) EST-1; (H) EST-2; (K) EST-3. Distribution of KAM value: (C) EST-0; (F) EST-1; (I) EST-2; (L) EST-3.
Abbreviations: EST: Electroshock treatment; KAM: Kernel average misorientation; MBZ: Metallurgical bonding zone.

processing at a current density of 205 A/mm^2 (EST-1), the texture comprised {-2113} and {3-301} textures, with {-2113} being dominant and exhibiting a maximum texture intensity of 9.99, as shown in Figure 8B. When the current density increased to 262 A/mm^2 (EST-2), as shown in Figure 8C, the texture contained {0001}, {-2113}, and {2-1-11} orientations, with a maximum texture strength of 10.03. With further current density increase, Figure 8D shows grains containing {0-1-13}, {-1102}, and {3-2-10} orientations, where {3-2-10} exhibits the highest orientation strength with a maximum value of 9.87. EST accelerates the recrystallization and grain growth processes of specific-orientation grains by providing extremely high energy density and non-thermal effects, thereby strengthening the preferred orientation of the original texture.

About the β phase (Figure 8E-H), the maximum texture strength of untreated Ti-6Al-4V/Cu-Cr-Zr is 2.99 in {111} direction with uniform texture distribution. After EST, the maximum texture strength was detected along {110} direction, but the texture strength was increased and the maximum texture strength was 3.47. Similar results were achieved in EST-2, where EST increased the stress concentration and texture strength. Increasing the current density increased the texture strength of the β phase in EST-3 and strengthened the texture strength in the {111} direction without significant orientation concentration, with a value of 4.22. Overall, after EST, the texture orientation of α and β phases becomes more concentrated.

3.3. Mechanical properties

The mechanical properties of Ti-6Al-4V/Cu-Cr-Zr composite materials were investigated under varying EST current densities, along with hardness and shear

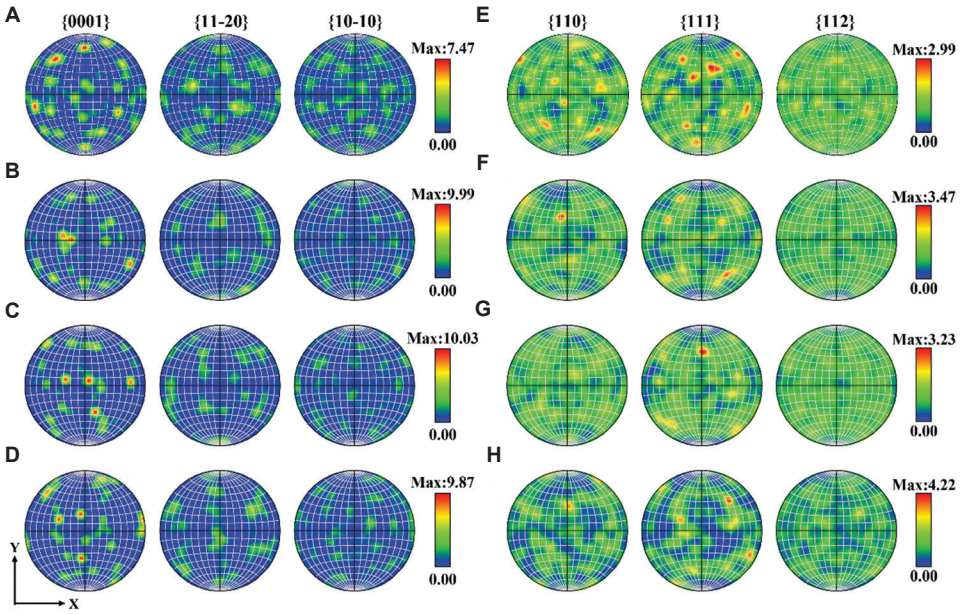

Figure 8. Texture distributions of α and β phases. (A) α phase EST-0; (B) α phase EST-1; (C) α phase EST-2; (D) α phase EST-3, (E) β phase EST-0; (F) β phase EST-1; (G) β phase EST-2; (H) β phase EST-3.
Abbreviation: EST: Electroshock treatment.

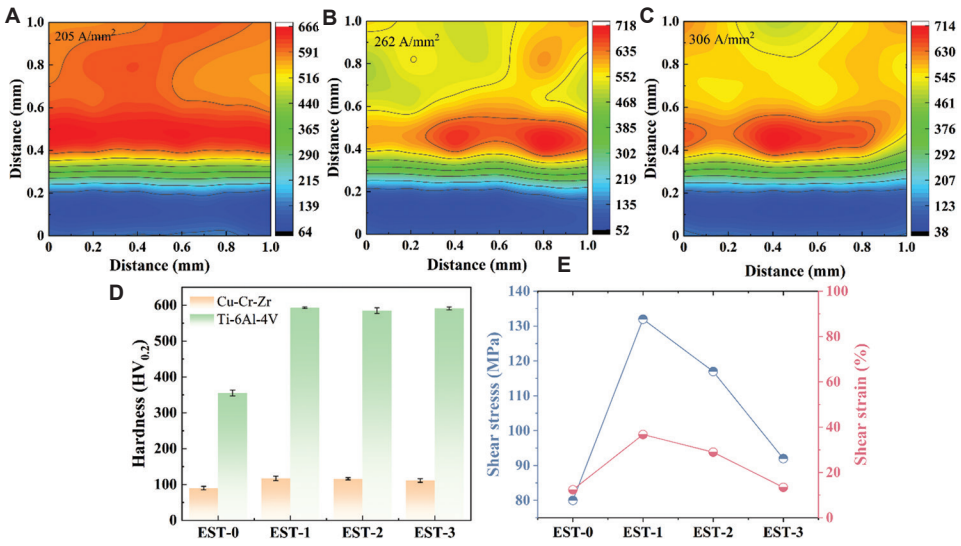

Figure 9. Changes in hardness and mechanical properties. (A) EST-1 microhardness distribution; (B) EST-2 microhardness distribution; (C) EST-3 microhardness distribution; (D) microhardness; (E) shear stress-strain.
Abbreviation: EST: Electroshock treatment.

tests. Figure 9A-D display the microhardness of the Ti-6Al-4V coating and the Cu-Cr-Zr substrate. In the EST-0 sample, the microhardness of the Ti-6Al-4V coating was 355 HV, while that of the Cu-Cr-Zr substrate was 90 HV. Following EST treatment, the microhardness of the Ti-6Al-4V coating exhibited a pronounced upward trend, with a maximum increase of approximately 70%. The Cu-Cr-Zr substrate also showed an upward trend, achieving a maximum increase of 30%, though this growth was relatively smaller compared to the Ti-6Al-4V coating. The hardness enhancement in post-EST samples is attributed to the formation of CuTi and Ti_2Cu during EST. The Cu-Ti intermetallic compound exhibits higher hardness, and the precipitation of CuTi and Ti_2Cu acts as a diffusion strengthening mechanism, thereby significantly enhancing hardness.

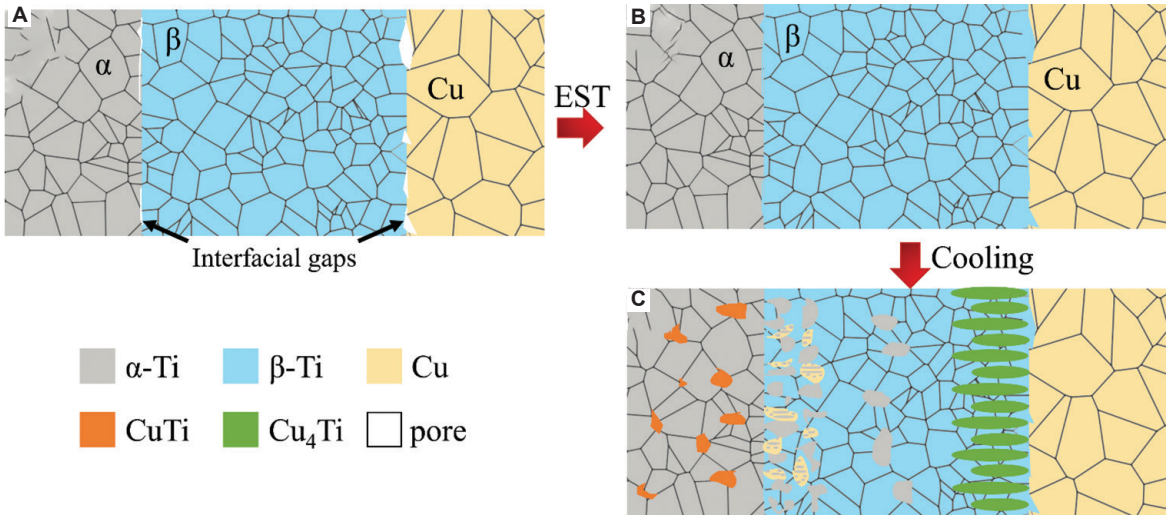

Figure 10. Schematic representation of microstructure evolution during EST. (A) Original sample; (B) EST process; (C) cooled sample. Abbreviation: EST: Electroshock treatment.

Figure 9E displays the shear engineering stress-strain curve of the Ti-6Al-4V/Cu-Cr-Zr composite. After EST, the shear strength and strain curve exhibited significant changes. The EST-0 sample achieved a shear strength of 80 MPa with an elongation of 12.35%. The reaction layer formed at the interface ensures a strong bond between the Ti-6Al-4V coating and the Cu-Cr-Zr substrate. Concurrently, the Cu-Cr-Zr matrix exhibits excellent toughness and plasticity, enabling deformation-induced resistance to external loads and thereby enhancing the overall toughness and plasticity of the Ti-6Al-4V/Cu-Cr-Zr composite. Following EST, both shear strength and elongation of the Ti-6Al-4V/Cu-Cr-Zr composite increased to varying degrees. The maximum increase occurred at a current density of 205 A/mm^2 (EST-1 sample), achieving a shear strength of 132 MPa and an elongation of 36.75%. Both shear strength and elongation exhibited an initial increase followed by a decrease across different current densities applied in EST. Comparing samples processed at varying current densities revealed that intergranular nano-precipitates play a crucial role in enhancing material strength and promoting dislocation activity, thereby improving plasticity. These intergranular nano-precipitates comprise multiple phases with distinct structures. The well-matched crystal planes favorable for dislocation slip enable continuous slip across different phase structures.[41] Following EST, the shear strength and elongation of the samples significantly surpassed those of untreated specimens. This demonstrates that adjusting current density effectively improves mechanical properties, though beyond a certain threshold, the effect becomes counterproductive.

3.4. Effect mechanism of EST on Ti-6Al-4V/Cu-Cr-Zr

The microstructural evolution of MBZ related to EST is shown in Figure 10, and the potential mechanism for the mechanism is proposed. EST can lead to a significant increase in the elongation of Ti-6Al-4V/Cu-Cr-Zr because the pressure and high temperature during EST results in the significant plastic deformation of the Ti-6Al-4V coating, which promotes the physical elimination of porosity at the bonding zone, as shown in Figure 10A and B. This process helps repair microscopic defects at the interface, thereby enhancing the material's mechanical properties.

As shown in Figure 10C, EST promotes the dissolution of precipitates and accelerates recrystallization in the MBZ of Ti-6Al-4V/Cu-Cr-Zr. With increasing temperature, thermal activation enhanced atomic diffusion and reaction kinetics. However, the interdiffusion behavior between Ti and Cu in the MBZ was greatly impacted. Diffusion of Cu atoms in the MBZ favored the stabilization of the β phase during cooling. The solid-state diffusion of Ti in the MBZ was suppressed, obviously, and an unbalanced mass flux between Ti and Cu occurred. Finally, a continuous α phase was formed on the surface. However, due to the small radius of the Cu atoms, the Cu atoms continued to diffuse through the grain boundaries into the reactive layer, and the Cu_4Ti phase might further capture Cu to promote its growth. The use of coherent intracrystalline precipitates to impede dislocation motion can enhance the strength of the material. In addition, activation of mechanisms, such as laminar dislocations and deformation can also enhance material properties. Under high-density current conditions, Ti_2Cu precipitates in the MBZ and

thereby increases material hardness, indicating that EST exhibits significant precipitation strengthening effects on Ti-6Al-4V/Cu-Cr-Zr composites. Simultaneously, the transient high temperatures generated when current flows through the Ti-6Al-4V/Cu-Cr-Zr composite repair minute internal defects, thereby improving mechanical properties. EST exhibits a pronounced homogenizing effect on the texture of LMD-fabricated Ti-6Al-4V/Cu-Cr-Zr composites, reducing anisotropy and enhancing interfacial bonding strength.

4. Conclusion

This work systematically elucidates the significant role of EST in regulating the microstructure and enhancing the mechanical properties of Ti-6Al-4V/Cu-Cr-Zr composite materials. It reveals the phase evolution mechanism induced by EST in the interfacial mixing zone (MBZ) and clarifies the precipitation strengthening effect of intermetallic compounds, such as CuTi and Ti_2Cu. The innovation lies in utilizing both thermal and non-thermal effects of EST to achieve precise control over phase composition and grain orientation, thereby significantly enhancing the hardness, shear strength, and ductility of the composite material. The main conclusions of this research are as follows.

(i) The Ti-6Al-4V/Cu-Cr-Zr composite fabricated by LMD exhibits a distinct MBZ region between the coating and the substrate. This region is primarily composed of the β phase, along with minor amounts of the α phase and Cu phase. After EST, the CuTi phase appears within the MBZ, and the diffraction peak intensity of the α phase changes: As the current density increases from 205 A/mm^2 to 306 A/mm^2, the diffraction peak intensity of the α phase ((002), (101)) first decreases and then increases. This change in α grain orientation is attributed to phase transformations induced by the thermal effects of EST, leading to chemical composition differences or the formation of precipitates.

(ii) After EST, the microhardness of the Ti-6Al-4V coating increases significantly, with a maximum improvement of nearly 70% compared to the EST-0 sample. This enhancement is attributed to the formation of CuTi and Ti_2Cu phases within the sample during the EST process. The precipitation of CuTi and Ti_2Cu acts as a diffusion promoter, substantially enhancing hardness. Following EST, both shear strength and elongation of the Ti-6Al-4V/Cu-Cr-Zr composite increased to varying degrees. Both shear strength and elongation improve with varying current densities, rising from the original sample's 80 MPa and 12.35% to 132 MPa and 36.75%, respectively. Compared to the original sample, optimal comprehensive mechanical properties are achieved at a current density of 205 A/mm^2.

(iii) EST exhibits significant precipitation strengthening effects on Ti-6Al-4V/Cu-Cr-Zr composites, regulating microstructure and enhancing material hardness. Concurrently, EST facilitates the repair of microdefects within the material, further improving its mechanical properties. These changes collectively enhance the performance of the cladding layer and broaden the applicability of Ti-6Al-4V/Cu-Cr-Zr composites.

This work presents a novel process for optimizing the properties of dissimilar metal composites fabricated by LMD, broadening the application prospects of Ti-6Al-4V/Cu-Cr-Zr composites in high-strength structural components for use in the aerospace and other fields. Future efforts will focus on further optimizing EST process parameters, exploring its applicability to other material systems, and conducting in-depth studies on the stability of its long-term service performance.

Acknowledgments

None.

Funding

This work was financially supported by the Major Research Plan of the National Natural Science Foundation of China (Grant No. 92266102), the National Natural Science Foundation of China (Grant No. 52271135, No. 52433026, No. 52571177), the Key Laboratory of Green Fabrication and Surface Technology of Advanced Metal Materials (GFST2024KF05), and the Innovative Research Group Project of Hubei Provincial Natural Science Foundation (Grant No. 2025AFA014).

Conflict of interest

The authors declare they have no competing interests.

Author contributions

Conceptualization: Shiqiang Xie, Changlin Huang
Data curation: Shiqiang Xie, Changlin Huang, Jiawei Gong
Formal analysis: Shiqiang Xie, Jiawei Gong, Pei Wang, Lechun Xie
Funding acquisition: Lechun Xie
Investigation: Changlin Huang, Jiawei Gong
Methodology: Shiqiang Xie, Changlin Huang, Jiawei Gong
Project administration: Lechun Xie
Software: Shiqiang Xie, Pei Wang
Supervision: Yan Wen
Validation: Changlin Huang, Pei Wang
Writing – original draft: Shiqiang Xie, Changlin Huang

Writing – review & editing: Yan Wen, Lechun Xie

Ethics approval and consent to participate

Not applicable.

Consent for publication

Not applicable.

Availability of data

The data that support the findings of this study are available from the corresponding author upon reasonable request.

References

1. He C, Zhou J, Zhou R, *et al*. Nanocrystalline copper for direct copper-to-copper bonding with improved cross-interface formation at low thermal budget. *Nat Commun*. 2024;15(1):7095.

   doi: 10.1038/s41467-024-51510-7

2. Du L, Liu K, Hu D, *et al*. Microstructural and mechanical anisotropy in pressure-assisted sintered copper nanoparticles. *Acta Materialia*. 2025;287:120772.

   doi: 10.1016/j.actamat.2025.120772

3. Nordet G, Gorny C, Mayi Y, *et al*. Absorptivity measurements during laser powder bed fusion of pure copper with a 1 kW cw green laser. *Optics Laser Technol*. 2022;147:107612.

   doi: 10.1016/j.optlastec.2021.107612

4. Liang YZ, Li L, Shen P. Pulsed current-driven wetting of 3YSZ by liquid Cu and its mechanisms. *J Eur Ceram Soc*. 2022;42(2):552-560.

   doi: 10.1016/j.jeurceramsoc.2021.10.021

5. Yang K, Wang Y, Guo M, *et al*. Recent development of advanced precipitation-strengthened Cu alloys with high strength and conductivity: A review. *Prog Mater Sci*. 2023;138:101141.

   doi: 10.1016/j.pmatsci.2023.101141

6. Imran MK, Masood SH, Brandt M, Bhattacharya S, Mazumder J. Direct metal deposition (DMD) of H13 tool steel on copper alloy substrate: Evaluation of mechanical properties. *Mater Sci Eng A*. 2011;528(9):3342-3349.

   doi: 10.1016/j.msea.2010.12.099

7. Romanov DA, Pochetukha VV, Sosnin KV, *et al*. Increase in properties of copper electrical contacts in formation of composite coatings based on Ni–C–Ag–N system. *J Mater Res Technol*. 2022;19:947-966.

   doi: 10.1016/j.jmrt.2022.05.040

8. Lu S, Wang L, Zhou J, Liang J. Microstructure and tribological properties of laser-cladded Co-Ti3SiC2 coating with Ni-based interlayer on copper alloy. *Tribol Int*. 2022;171:107549.

   doi: 10.1016/j.triboint.2022.107549

9. Hu Z, Huang C, Xie L, Hua L, Yuan Y, Zhang LC. Machine learning assisted quality control in metal additive manufacturing: A review. *Adv Powder Mater*. 2025;4(6):100342.

   doi: 10.1016/j.apmate.2025.100342

10. Liu Q, Chu S, Zhang X, *et al*. Laser shock processing of titanium alloys: A critical review on the microstructure evolution and enhanced engineering performance. *J Mater Sci Technol*. 2025;209:262-291.

    doi: 10.1016/j.jmst.2024.04.075

11. Tian Y, Shen J, Hu S, Gou J, Cui Y. Effects of cold metal transfer mode on the reaction layer of wire and arc additive-manufactured Ti-6Al-4V/Al-6.25Cu dissimilar alloys. *J Mater Sci Technol*. 2021;74:35-45.

    doi: 10.1016/j.jmst.2020.09.014

12. Zhou Y, Xu X, Zhao Y, *et al*. Introducing Zhao Y, 0nanodomains in Ti-6Al-4V: The mechanism of accelerating $\alpha \rightarrow \beta$ transformation kinetics via electropulsing. *J Mater Sci Technol*. 2023;162:109-117.

    doi: 10.1016/j.jmst.2023.04.014

13. Xie S, Huang C, Ding C, *et al*. Microstructure and tribological properties of laser melting deposited Tiposited coating on CuoatiZr substrate. *Adv Eng Mater*. 2025;27:2500531.

    doi: 10.1002/adem.202500531

14. Nai X, Chen H, Zhao S, *et al*. Investigation on the microstructure, mechanical and electrical properties of Ti3SiC2/Cu joint obtained by Ti25Zr25Ni25Cu25 amorphous high entropy alloy and Ag composite filler. *Mater Sci Eng A*. 2023;877:145190.

    doi: 10.1016/j.msea.2023.145190

15. Liu C, Wang H, Zhou J, *et al*. Optimising the mechanism of electroshock treatment on the tensile behaviour of the laser melting deposited Ti55531 alloy. *Virtual Phys Prototyp*. 2025;20(1):2449174.

    doi: 10.1080/17452759.2024.2449174

16. Li X, Feng Y, Wang X, *et al*. Microstructures and properties of AlCrFeNiMnx high-entropy alloy coatings fabricated by laser cladding on a copper substrate. *J Alloys Compd*. 2022;926:166778.

    doi: 10.1016/j.jallcom.2022.166778

17. Jia H, Li X, Dong Z, Jia L, Luo H. Microstructure, wear and corrosion properties of laser melted CoCrNiFeTix high-entropy alloy coatings on copper alloys. *J Alloys Compd*. 2025;1021:179674.

    doi: 10.1016/j.jallcom.2025.179674

18. Dong Q, Zheng S, An Y, Pu J. Effect of copper addition on

the microstructure, wear resistance, anti-corrosion and antibacterial behavior of laser cladding CoCrW coatings in marine environment. *Surf Coat Technol*. 2025;502:131966.

doi: 10.1016/j.surfcoat.2025.131966

19. Zhou YJ, Li Y, Tan N, *et al*. Preparation process and mechanical properties of laser cladding gradient molybdenum coating on copper alloy. *Surface Coat Technol*. 2023;470:129888.

doi: 10.1016/j.surfcoat.2023.129888

20. Wu YY, Zhou J, Han GL, *et al*. *In-situ* SEM characterization of fracture mechanism of TiB/Ti-2Al-6Sn titanium matrix composites after electroshocking treatment. *Rare Metals*. 2024;43(6):2805-2818.

doi: 10.1007/s12598-023-02614-4

21. Bhowmik A, Tan JL, Yang Y, *et al*. Misorientation and dislocation evolution in rapid residual stress relaxation by electropulsing. *J Mater Sci Technol*. 2025;209:292-299.

doi: 10.1016/j.jmst.2024.05.031

22. Chen K, Zhan L, Yu W. Rapidly modifying microstructure and mechanical properties of AA7150 Al alloy processed with electropulsing treatment. *J Mater Sci Technol*. 2021;95:172-179.

doi: 10.1016/j.jmst.2021.03.060

23. Xie L, Sun H, Wen Y, Hua L, Zhang LC. Electromagnetic treatment enhancing performance of metal materials: A review. *Prog Mater Sci*. 2025;153:101488.

doi: 10.1016/j.pmatsci.2025.101488

24. Fan W, Chu Q, Yang X, Li W, Zou Y, Hao S. Microstructure and mechanical properties of probeless friction stir spot welded Al-Li alloy joints via fast electric pulse treatment: A comparative study. *Mater Charact*. 2023;205:113276.

doi: 10.1016/j.matchar.2023.113276

25. Liu X, Yang Y, Chen H, Li Y, Xu S, Zhang R. Mesoscopic defect healing and fatigue lifetime improvement of 6061-T6 aluminum alloy by electropulsing treatment. *Eng Fail Anal*. 2023;146:107111.

doi: 10.1016/j.engfailanal.2023.107111

26. Qian D, Li W, Deng J, Wang F, Wu M. Promoting the interface connection of hot-compression bonded stainless steel via introducing a novel electroshocking treatment. *J Mater Res Technol*. 2022;18:2140-2151.

doi: 10.1016/j.jmrt.2022.03.128

27. Bao J, Chen W, Bai J, Xu J, Shan D, Guo B. Local softening deformation and phase transformation induced by electric current in electrically-assisted micro-compression of Ti–6Al–4V alloy. *Mater Sci Eng A*. 2022;831:142262.

doi: 10.1016/j.msea.2021.142262

28. Wu W, Song Y, Lu J, Yu Y, Hua L. Novel strategy of electroshock treatment for improving mechanical performances of Al–Zn–Mg–Cu alloy by edge dislocation increment. *Mater Sci Eng A*. 2022;854:143805.

doi: 10.1016/j.msea.2022.143805

29. Jung J, Ju Y, Morita Y, Toku Y. Enhancement of fatigue life of aluminum alloy affected by the density of pulsed electric current. *Int J Fatigue*. 2017;103:419-425.

doi: 10.1016/j.ijfatigue.2017.06.021

30. Zhang S, Geng M, Kim MJ, Bae JH, Nam Han H, Hong ST. Prolonged fatigue life in aluminum clad steel by electropulsing treatment: Retardation of interface-microcrack formation. *Int J Fatigue*. 2023;167:107376.

doi: 10.1016/j.ijfatigue.2022.107376

31. Ren X, Wang Z, An R. A promising approach to enhance fatigue life of TC11 titanium alloy: Low dislocation density and surface grain refinement induced by electropulsing. *J Mater Sci Technol*. 2025;204:60-70.

doi: 10.1016/j.jmst.2024.03.020

32. Bo H, Duarte LI, Zhu WJ, *et al*. Experimental study and thermodynamic assessment of the Cu–Fe–Ti system. *Calphad*. 2013;40:24-33.

doi: 10.1016/j.calphad.2012.12.001

33. Donthula H, Vishwanadh B, Alam T, *et al*. Morphological evolution of transformation products and eutectoid transformation(s) in a hyper-eutectoid Ti-12 at% Cu alloy. *Acta Mater*. 2019;168:63-75.

doi: 10.1016/j.actamat.2019.01.044

34. Murray JL. The Cu–Ti (copper-titanium) system. *Bull Alloy Phase Diagr*. 1983;4(1):81-95.

doi: 10.1007/BF02880329

35. Li K, Yang J, Yi Y, *et al*. Enhanced strength-ductility synergy and mechanisms of heterostructured Ti6Al4V-Cu alloys produced by laser powder bed fusion. *Acta Mater*. 2023;256:119112.

doi: 10.1016/j.actamat.2023.119112

36. Yao X, Sun QY, Xiao L, Sun J. Effect of Ti_2Cu precipitates on mechanical behavior of Ti–2.5Cu alloy subjected to different heat treatments. *J Alloys Compds*. 2009;484(1-2):196-202.

doi: 10.1016/j.jallcom.2009.04.095

37. Jiang Q, Wen Z. *Thermodynamics of Materials*. Beijing, China: Higher Education Press; 2011.

38. Zhang YJ, Miyamoto G, Shinbo K, Furuhara T. Quantitative measurements of phase equilibria at migrating α/γ interface and dispersion of VC interphase precipitates: Evaluation of driving force for interphase precipitation. *Acta Mater*. 2017;128:166-175.

doi: 10.1016/j.actamat.2017.02.020

39. Zhao R, Li L, Nie Z, Ma Z, Guo Q. Effects of pre-heating

induced interfacial diffusion on microstructure and related mechanical properties of direct laser metal deposited Inconel 625 superalloy on a Cu-Cr-Zr substrate. *Mater Sci Eng A*. 2025;920:147551.

doi: 10.1016/j.msea.2024.147551

40. Lin J, Zhou J, Zhang S, *et al*. Rapidly achieving a reliable full-ceramic interface of ZrC-SiC composite using Ti interlayer via pulsed electric current joining. *J Eur Ceram Soc*. 2023;43(5):1777-1789.

doi: 10.1016/j.jeurceramsoc.2022.12.048

41. Zou J, Chen S, Cheng P, *et al.* Achieving high strength and large ductility in a $Cr_{30}Co_{30}Ni_{30}Al_5Ti_5$ alloy through intergranular precipitation. *J Mater Sci Technol*. 2025;215:167-179.

doi: 10.1016/j.jmst.2024.07.029

ACCSCIENCE PUBLISHING

Engineering Science in Additive Manufacturing

ORIGINAL RESEARCH ARTICLE

TwinPrint: A dual-arm robotic 3D bioprinting solution for multi-material biofabrication of soft matter constructs

Noofa Hammad[1†], Zainab N. Khan[1†], Hibatallah Alwazani[1,2], Kowther Kahin[1], Dana M. Alhattab[1,3], Christian Baumgartner[4], and Charlotte A. E. Hauser[1,3,4*]

[1]Laboratory for Nanomedicine, Division of Biological and Environmental Science and Engineering, King Abdullah University of Science and Technology (KAUST), Thuwal, Makkah Province, Saudi Arabia

[2]Communication Theory Lab, Department of Electrical Engineering, University of British Columbia-Okanagan, Kelowna, BC, Canada

[3]Computational Bioscience Research Center, King Abdullah University of Science and Technology, Thuwal, Makkah Province, Saudi Arabia

[4]Institute of Health Care Engineering with European Testing Center of Medical Devices, Graz University of Technology (TU Graz), Graz, Styria, Austria

Abstract

As the field of three-dimensional (3D) bioprinting gains increased momentum, complex 3D bioprinters are being developed to keep up with the needs of biofabrication and tissue engineering. Cartesian-based linear 3D bioprinters have facilitated the fabrication of 3D biological constructs and scaffolds. However, to achieve meaningful advancement in biofabrication, 3D bioprinters need increased freedom of motion, seamless multi-material printing, full automation, and ease of use. In this paper, we propose TwinPrint, a dual-arm robotic 3D bioprinting system, designed to be compatible with soft bioinks to build multi-material constructs, crucial for creating functional tissue. The uniquely integrated robotic 3D bioprinter—comprising an in-house fabricated coaxial nozzle, two 4-axis robotic arms, six microfluidic pumps, and a software interface—work harmoniously as a single unit. We showcase the development of the Python-based software and Graphical User Interface, integrating all components into a single easy-to-use interface. Due to their human-like and instantaneous gelation properties, peptide-based bioinks were used as printing material to test the system. Developed in our laboratory as an alternative to gelatin- and alginate-based bioinks, they avoided chemical and ultraviolet-crosslinking by solidifying instantaneously under physiological conditions. For system performance testing, acellular and cellular constructs were observed for structural fidelity, multi-material layering, printing accuracy, cell viability, and proliferation. Overall, our proposed system showcases an innovative integration of robotics for biofabrication to expedite the printing process and enable multi-task print protocols. By saving time, increasing degrees of freedom, and expanding printing complexity, we believe TwinPrint is a promising next step for biofabrication.

Keywords: 3D bioprinting; Extrusion-based printing; Peptide bioinks; Multi-robot systems; Multi-material construct

[†]*These authors contributed equally to this work.*

***Corresponding author:**
Charlotte A. E. Hauser
(charlotte.hauser-funke@tugraz.at)

Citation: Hammad N, Khan ZN, Alwazani H, *et al*. TwinPrint: A dual-arm robotic 3D bioprinting solution for multi-material biofabrication of soft matter constructs. *Eng Sci Add Manuf*. 2025;1(4):025410025. doi: 10.36922/ESAM025410025

Received: October 9, 2025

Revised: November 13, 2025

Accepted: November 21, 2025

Published online: December 5, 2025

1. Introduction

Three-dimensional (3D) bioprinting technology has facilitated remarkable advancements in the biofabrication of complex biomimetic tissues,[1,2] thus catering to challenges in organ donor shortage and enabling solutions in personalized medicine to reduce immune system response. The most demanding applications for engineered tissues include the cartilage,[3] skin,[4,5] cardiac tissue,[6] vascular grafts,[7] and hard tissues such as bones.[8] It has also shown high potential in eliminating dependency on animal testing by introducing artificially constructed organs for pharmacology and pharmaceutical research.[9]

The heterogeneity and complexity of human tissues necessitate 3D bioprinting of multi-material and multi-cellular constructs with physical and mechanical properties closer to native tissues.[10] This entails the integration of various biomaterials and cell types to fabricate a single biomimetic construct.[11,12] In light of this, several researchers have proposed methods to accomplish the goal of 3D printing multi-material acellular and cellular scaffolds of varying mechanical properties and print resolutions. Some have modified the design of commercial, conventional 3D printers by integrating multiple printheads for multi-material 3D bioprinting.[11,13] On the other hand, Liu *et al.*[14] and Miri *et al.*[15] developed their own multi-head 3D bioprinter with a rapid switching mechanism for bioink interchangeability. A handheld multi-material 3D printer was introduced by Pagan *et al.*[16] for *in situ* 3D bioprinting for tissue repair applications.

Ultrashort self-assembling amphiphilic peptides are compounds with both hydrophobic and hydrophilic regions.[17,18] Peptide Ac-Ile-Val-Cha-Lys-NH_2 (IVZK), which was investigated in this study for its suitable properties belongs to a class of tetrameric ultrashort self-assembling peptides that was described in detail in earlier publications.[19,20] These peptides assemble into fibers and further into 3D supramolecular structures in the form of hydrogels by non-covalent interactions, such as van der Waals interactions and hydrogen bonding. Adding ionic solutions such as phosphate-buffered saline (PBS) to aqueous peptide solutions can accelerate their fiber formation, reducing gelation times to minutes and seconds, depending on the specific peptide sequence and the peptide concentration. These properties underscore the potential of ultrashort self-assembling amphiphilic peptides as an optimal bioink material in extrusion-based 3D printing and bioprinting, as alternatives to gelatin and alginate-based bioinks, to facilitate instantaneous layer-by-layer printing of acellular and cell-laden material.

With several promising attempts at developing multi-material 3D bioprinters, certain challenges still exist. Primarily, large-scale printing has not yet been realized. Clinically practical sizes need to be achieved without extending fabrication time.[21] This requires an array of new approaches such as concurrent printing, robotic maneuverability, and full system integration and automation.

Of note, a vast majority of 3D bioprinting systems involve pre-mixing or post-printing curing protocols, *i.e.*, bioinks are pre-mixed before loading in a pressure-based extruder, and final crosslinking occurs through curing processes after printing. This approach, while common, is not as biologically suitable on the grand scale, due to its dependency on ultraviolet-based or chemical crosslinking techniques. Soft matter bioinks, such as ultrashort self-assembling peptides, are key candidates to explore for 3D bioprinting due to their instantaneous gelation properties, biocompatibility, and nanofibrous topography resembling the natural extracellular matrix.[17,18,22] While avoiding the use of harmful crosslinking reagents, their instantaneous binding nature requires increased precision control. Screw-driven syringe pump extrusion systems have been found to offer better control and flow accuracy when working with ultrashort peptides.[9,23] Our previous research explored the development of microfluidic syringe pump extrusion systems embedded with dual coaxial nozzles to accommodate the gelation nature of peptide bioink.[20,23-25]

Examining the use of articulated robots for 3D biofabrication applications highlights a number of advantages. In comparison to traditional Cartesian 3D bioprinters, articulated robot workspace is not confined and can perform successful *in situ* bioprinting at regions such as curved or irregular anatomical sites,[26-28] and perform additional tasks aside from 3D bioprinting, making them cost-effective. More significantly, articulated robots offer additional degrees of freedom, which allows for faster fabrication time of highly curved scaffolds with intricate geometry while achieving high deposition precision and printing resolution.[29] Non-planar robotic printing can revolutionize 3D bioprinting by breaking away from the traditional layer-by-layer XYZ approach and creating more defined extrusion paths to fabricate complex organs and tissues.[30-32] A multi-arm configuration running in tandem reduced biofabrication time considerably by increasing the degrees of freedom from the standard 3 axes to 5–6 axes, which would be vital for *in situ* bioprinting at the clinical phase.[33]

Among many challenges facing 3D bioprinting, one significant obstacle is achieving reliability and robustness.[34] Currently, 3D bioprinting is hindered by extrusion failures, bioink incompatible mechanical and rheological properties, and the lack of robust, end-to-end automation.

In this work, we address the latter challenge by advancing the automation and integration of the different parts within the 3D bioprinting system, with the goal of accelerating the technology's overall progress.

Consequently, in this paper, we propose a dual-arm, microfluidic extrusion-based multi-material 3D bioprinter, called TwinPrint, with an integrated graphical user interface (GUI). TwinPrint leverages the advantages of robotic arms to develop a system catering to soft matter bioinks, including peptide hydrogels, to achieve 3D bioprinting of multi-material, geometrically complex bio-constructs for skin grafting, disease models, and drug testing applications. Taking user workflow into account, an intuitive GUI is developed in a pre-, intra-, and post-printing layout for quick navigation. Moreover, several tests to evaluate the system performance, printability, biocompatibility, and cell viability are performed.

To the best of our knowledge, this is the first work of its kind that presents synchronized dual robotic arms for 3D bioprinting, free from any crosslinking dependencies that could further complicate the printing process and present potential harm to cell viability. More importantly, the demonstration of layer-by-layer switching of robotic arms is an advantageous time saver as compared to a linear Cartesian system with a head switching mechanism. Given the fragile nature of cell viability in the bioprinting process, quicker standardized protocols are extremely crucial in realizing realistic goals of clinical bioprinting. Finally, the capability of increasing degrees of freedom in a robotic arm setup adds further time, space, and structural complexity advantages that are far from possible with state-of-the-art Cartesian printers.

2. Materials and methods

2.1. Peptide synthesis

Peptide Ac-Ile-Val-Cha-Lys-NH_2 (IVZK) was synthesized using the solid-phase peptide synthesis method on a CS136X peptide synthesizer (CSBio, USA). After synthesis, the peptide was removed from the resin using a mixture of 95% trifluoroacetic acid, 2.5% tri-isopropyl silane, and 2.5% water at room temperature for 2 h. The peptide was then precipitated by adding cold diethyl ether to the peptide solution and kept overnight at 4°C. The precipitated peptide was separated from the supernatant by centrifugation. Finally, the peptide was purified by reverse-phase high-performance liquid chromatography with a C-18 column (2–98% acetonitrile in 15 min) at a flow rate of 20 mL/min and collected at a yield of over 60%. The peptides were stored within sealed Falcon containers at −80°C, and peptide aliquots were taken for experiments.

2.2. System description

The TwinPrint System, as the name implies, consists of two identical 3D bioprinting sets; a set is composed of a 3D printing robotic arm and a microfluidic-based extrusion system, as depicted in Figure 1. Previous studies have described our 3D bioprinter at length.[20,23,24] In a single print job, the sets take turns in printing with different materials, constituting a multi-material structure. Before printing, the robotic arms agree on a start point from which each robot calculates its movements with respect to this point. A GUI Software is built using Python to control and integrate the system's different components from a single software platform. The system input is a G-code (Geometry Code) file of a desired construct, from which the required data are extracted and transmitted to the robots for command execution. As G-code is designed to contain information for Cartesian systems, it first needs to be converted to polar coordinates for it to be understandable by the robots.

2.2.1. Geometry code (G-code) obtainment

3D bioprinting is an additive manufacturing process that uses a computer-aided design (CAD) model, which is converted into an standard template library (STL) file to define the 3D geometry of the object as a mesh of small triangles.[35,36] Conventionally, the first step in printing is to load a desired STL file into the printing software and slice it into G-code, which denotes the required XYZ movements and speeds at each coordinate to print the 3D object layer by layer.[37] To this effect, basic objects were designed in Solidworks® CAD software (Dassault Systèmes, France), including cuboids and rings, and sliced to obtain their G-codes. However, because robots are designed with

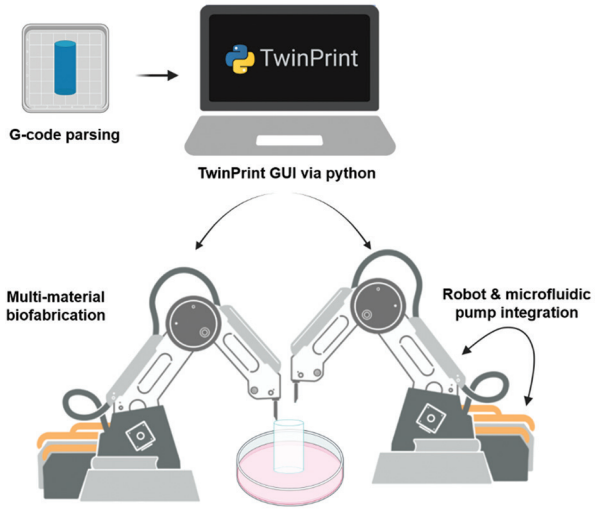

Figure 1. An illustration of the TwinPrint system
Abbreviation: GUI: Graphical user interface.

increased degrees of freedom and do not naturally read G-code, a parsing approach was developed to extract the required commands for each point from the G-code.

2.2.2. Geometry code (G-code) parsing

The Dobot Magician is compatible with a Repetier host 3D printing software that establishes communication between a single Dobot and the software, allowing users to load G-code files and 3D print, as is done with generic Cartesian 3D printers. However, in this case, the aim is to integrate two Dobot Magician arms for communication and printing, which is beyond the scope of the Repetier Host software. Hence, a Python program was developed from scratch to achieve this goal. Because the default Dobot application programming interface (API) protocol is not designed to accept G-code files, a G-code parser was first implemented in the Python program. For successful translation, the parsing process included two essential steps: information extraction and instantaneous coordinate calculations. The parser first scans the loaded G-code file of the 3D construct intended to be printed, line by line, looking for a specific pattern of interest, denoted by a letter G followed by a number that indicates the type of geometry change. In addition, the G line provides information on the selected positioning type (absolute or relative), XYZ coordinates, and extrusion feed rate (denoted by F). For instance, G90 sets the positioning type to "Absolute" for the subsequent G lines, which contain the XYZ geometric locations with respect to the current location.

When a G-code file is loaded into the Python program, instantaneous geometric coordinate recalculations are done based on the selected positioning type, and the new coordinates are stored temporarily in the system. Absolute positioning moves the robotic arm exactly to the XYZ coordinates, while relative positioning indicates how far the XYZ point is from the current location. The user specifies and saves a starting point to which each absolute coordinate is added. In the case of relative positioning, the XYZ coordinates of the starting point are only added to the first geometric location in the G-code. The rest of the coordinates are added, one by one, to the latest accumulated value.

Furthermore, the number of layers in a 3D structure is found by counting how many times the Z value is altered in the G-code file while parsing. Here, the Z value stands for the height parameter in the print. This information is useful when splitting the layers between the two arms to send the recalculated coordinates associated with each layer to the appropriate arm, and to keep track of printing progress, in terms of numbers of layers that have been printed and are still left. Moreover, the printing time (t_p) in seconds for a print is calculated based on the speed of the arm (v) and the total displacement (d_T) of the arm, and the formula is expressed as follows:

$$t_P = \frac{d_T}{v} \tag{1}$$

In terms of extrusion, the flow rate from all active syringe pumps provides an approximate total flow rate for the extrusion at the tip of the needle. While it is an approximation due to material loss during extrusion, the effects are considered negligible. The movement of the arms is synced with the speed of extrusion, which is, decidedly, the summed-up flow rate of the active pumps. Note that the F value of the G-code refers to the feed rate, or the print move, in which extrusion occurs. It is essential that the speed setting is aligned with the rate of extrusion to avoid shearing and inconsistency in the case of quickened movement, and an undesirable thickness in the case of slower movements. Hence, the compatibility of both speeds for the pumps and arm needs to be optimized to ensure optimal print quality.

2.3. Robotic arms integration

For the dual-arm integration, the TwinPrint system leverages Dynamic-link libraries alongside a Python API provided by Dobot® to communicate with the robots. The two robotic arms are connected via separate computer USB ports and take turns in printing based on the number of layers specified for each arm by the user. The arms initially agree on a global point in 3D space as a start point for the cooperative 3D printing to begin. The two robotic arms are positioned facing each other with respect to the location of the plate. The arm's maximum reachability in terms of the x-axis must be taken into consideration; the farther the arm is placed, the less printing space it can cover. The user specifies and saves the set global point within the printing workspace in the system, which acts as a reference point from which the 3D structure coordinates are recalculated by each arm separately. Therefore, precision when setting the common global point is of utmost importance. Slight offsets from the robotic arm motors prove to be detrimental to the print quality.

For collision avoidance between the two arms, the handing-over process is timed; only one arm moves at a time to or from the printing workspace. In addition, the waiting location of each arm is at a particular distance away from the set global point. While the arm is waiting for its turn, it is kept moving back and forth in a segment of 2 mm to avoid timeout.

In the case that the arms are working in tandem on the same 3D structure, they are bound to operate within the

same printing workspace collectively. Hence, the printing area is not necessarily doubled by using dual arms as one might previously assume. Both arms must reach the entire print area. On the other hand, if the print is not divided layer by layer and instead, divided from the X or Y dimension, then the printing area can be doubled. Hence, the maximum print area is a function of the allocation of printing sequence to both arms. At minimum, it could be the same as the printing area of one arm, and at maximum, it could be doubled.

2.4. Microfluidic syringe pumps integration

A set of Cellix® ExiGo microfluidic syringe pumps (Cellix, Ireland), consisting of four pumps, is connected to the TwinPrint GUI via a USB cable. The computer port number and the unique addresses of the pumps are used for bidirectional communications in a master-slave approach without confusion. An API containing all the functions necessary to operate and handle communications with pumps is created in Python. The pumps can be operated synchronously with the arms, or separately as a whole set or individually. Flow rates are set for extrusion depending on the viscosity of the biomaterial used.

Overall system performance can be hampered due to continuous monitoring and updating of individual pump statuses to the GUI, considering that there are eight pumps in the system. To reduce the communication overload, one query command, called "Status Word," is used to return information about the entire set rather than query-specific or pump-specific commands despite their simpler, straightforward responses. Further calculations and conversions have to be done to extract the useful information from the Status Word's response. The backend code requests an update on the screen only if a pump status has changed from the previous received status, which eliminates the unnecessary communications with the GUI.

2.5. GUI

The GUI Python toolkit used to build the TwinPrint GUI was wxPython. The GUI layout and features incorporated into the TwinPrint GUI were selected specifically based on past 3D bioprinting experience over the span of 5 years, to suit researchers' needs in the Laboratory for Nanomedicine. The design was developed from a user's perspective, *i.e.*, what the user would need for easy control before and during printing. Pre-printing, several parameters are set by the user, while during 3D bioprinting, the user controls the devices and monitors print and flow status.

The user interface is based on classes that inherit attributes and methods from wxPython classes to create and manage the GUI widgets as well as display updated information on the screen. Additional methods are added to those classes to perform side calculations, *e.g.*, based on the user's inputs, feedback from a device, and communication with the APIs. Therefore, there are intensive background operations and constant requests to update the GUI within the system that can cause a delay in providing updates on screen or even worse, cause GUI freezing or crashing. To avoid these issues, threading, which is a locking mechanism, in addition to the pub/subapproach is applied.

Most system calculations are dependent on the results of other calculations that can occur in other parts of the system. This makes the adoption of the threading approach ideal, as the threads can share the memory space as well as expedite execution time. In addition, it avoids the issue of an unresponsive GUI. Hence, background operations are allocated to threads, called worker threads, and each has a certain task to do. The threads may request to update information on-screen according to their tasks and results. Another thread, called the GUI thread, is responsible for making the GUI appear on-screen, is dedicated to interacting with the GUI screen. A single Python class method is allocated for coordinating GUI update requests to prevent simultaneous screen updates from multiple sources. Furthermore, a locking method is applied to the GUI updating class to permit only one update request to be received and executed at a time. Furthermore, to establish efficient, instantaneous communication between the various GUI classes, the pub/sub approach is utilized.

2.6. System tests

After system design and development, a series of tests were conducted to evaluate TwinPrint. For the evaluation of printing accuracy with dual-arms, several pen tests were performed to draw different shapes and compare them with single-arm results (section 3.2). To ensure seamless pump communication, an experiment was set up to compare flow rates run by TwinPrint and SmartFlo®—the default pump software (section 3.3). For dual-arm synchronization, an acellular 3D printing experiment was conducted (section 3.4). To study cell viability, a disease model was created using cellular 3D bioprinting with multiple cell types (section 3.5).

2.7. Acellular 3D printing and cellular 3D bioprinting of a disease model

We performed acellular printing experiments as described in detail in section 3.4 to test the material deposition of the system and print resolution. For the cellular bioprinting experiment, we printed using two cell types to mimic a multi-cellular disease model; acute myeloid leukemia (AML) cell line (HL60) and human bone marrow mesenchymal stem

cells (BM-MSCs). The HL60 and BM-MSCs cell lines were supplied by ATCC (USA) and Professor Abdalla Awidi (Cell Therapy Center, University of Jordan, Amman, Jordan), respectively. Human BM-MSCs were cultured and maintained, as described before. Briefly, the cells were cultured at a seeding density of 4×10^3 cells/cm^2; when cultures reached 80% confluence, the cells were subcultured using 0.25% trypsin. Cells in passages 4–8 were used in the bioprinting experiments. Human BM-MSCs cells were maintained in α-modified minimum essential medium (α-MEM) supplemented with 10% mesenchymal stem cell–qualified fetal bovine serum (FBS), 2 mM L-glutamine, and 1% penicillin/streptomycin (GIBCO, ThermoFisher, USA). HL-60 AML cell line was cultured in RPMI-1640 media supplemented with 10% FBS and 1% penicillin/streptomycin (GIBCO, ThermoFisher, USA). The cells were maintained at a density of 500×10^3 cells/mL media. Before bioprinting, human BM-MSCs were stained with Cell Tracker™ Green 5-chloromethyl fluorescein diacetate (CMFDA) Dye (Invitrogen, ThermoFisher, USA) at a final concentration of 10 μM, and the HL-60 cell line was stained with CellTracker™ Red CMTPX Dye (Invitrogen, ThermoFisher, USA) at a final concentration of 5 μM.

For bioprinting, human BM-MSCs (3×10^6 cells) were mixed with 500 μL of 1× PBS and loaded into the microfluidic tubing of the first robotic arm. In addition, HL-60 (9×10^6 cells) were mixed with 500 μL 1× PBS and loaded into the microfluidic tubing of the second robotic arm. Each cell type was printed separately using the two robotic arms in an alternating layer-by-layer fashion. Growth media composed of a 1:1 ratio of human BM-MSCs and HL-60 cell line media was added to the printed cell-laden constructs. The printed cell-laden constructs were placed in the CO_2 incubator set at 37°C, 5% CO_2, and 95% relative humidity, with media exchange every 3 days.

For cytoskeletal staining, cell-laden constructs were fixed with 4% formaldehyde solution for 30 min and then incubated in a cold cytoskeleton buffer (3 mM $MgCl_2$, 300 mM sucrose, and 0.5% Triton X-100 in PBS solution) for 5 min. The cell-laden constructs were then incubated in blocking buffer solution (5% FBS, 0.1% Tween-20, and 0.02% sodium azide in PBS) for 30 min. For F-actin, anti-mouse IgG (whole molecule)-FITC and rhodamine-phalloidin (1:300; Thermo Fisher Scientific, USA) were added to the cell-laden constructs for 1 h. Then DAPI were added for 5 min to counterstain the nucleus. The cell-laden constructs were observed and imaged using a laser scanning confocal microscope (Zeiss LSM 710 Inverted Confocal Microscope, Germany).

For confocal microscopy imaging, an inverted laser scanning confocal microscope (Zeiss LSM 880 Inverted Confocal Microscope, Germany) was used to observe and evaluate cells within the printed constructs. Human BM-MSCs stained with CMFDA Dye were observed using 492 nm excitation and 517 nm emission filters. HL-60 cells stained with 5-chloromethyl tetraphenyl-p-xylylene (CMTPX) dye were observed using 577 nm excitation and 602 nm emission filters. Z-stack images were obtained to evaluate the 3D distribution of cells within the printed cell-laden constructs.

3. Results and discussion

3.1. TwinPrint system

The TwinPrint System, as shown in Figure 2, comprises two sets of four microfluidic syringe pumps, two robotic arms with custom-designed nozzles,[23] tubes connecting the syringe tips to the nozzles, and a computer running the TwinPrint GUI. Figure 3 displays the four GUI tabs, with Figure 3A and B showing the pre-printing settings and Figure 3C and D displaying the settings for the initiation, control, and monitoring of the 3D bioprinting process.

First, the "Device Settings" tab, as shown in Figure 3A, allows the user to connect/disconnect devices and set generic printing parameters, including desired z-height, pump syringe type, and desired flow rate. The GUI displays a list of communication (COM) ports that are open for connection, to avoid interference with occupied ports. Figure 4A and B are zoomed-in images of the Dobot settings and Pump settings, respectively, showing examples of how the system operates when devices are connected to TwinPrint. Upon successful connection of the devices, the corresponding settings are activated across all tabs to allow for communication with the connected devices exclusively.

Instantaneous updates are provided for the robotic arm's location, which is used to determine the arm corresponding to each box of Dobot settings (Figure 4A). It is crucial to identify which arm is R1 to avoid false layer splitting, as R1 is always the first to start printing. The user-defined home coordinates are used as a starting point

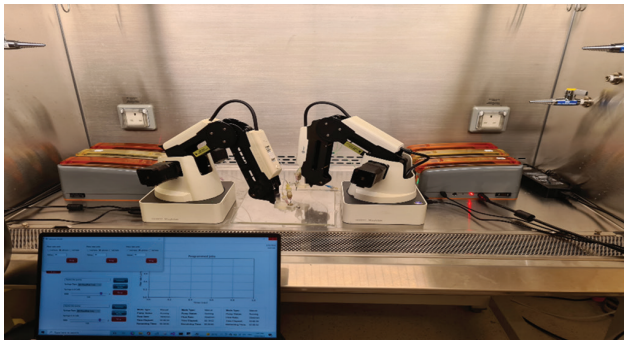

Figure 2. The TwinPrint system with an older version of the user interface

Figure 3. User interface. (A) Device settings tab; (B) Pump program mode tab; (C) Job settings tab; (D) Printing status monitoring tab.

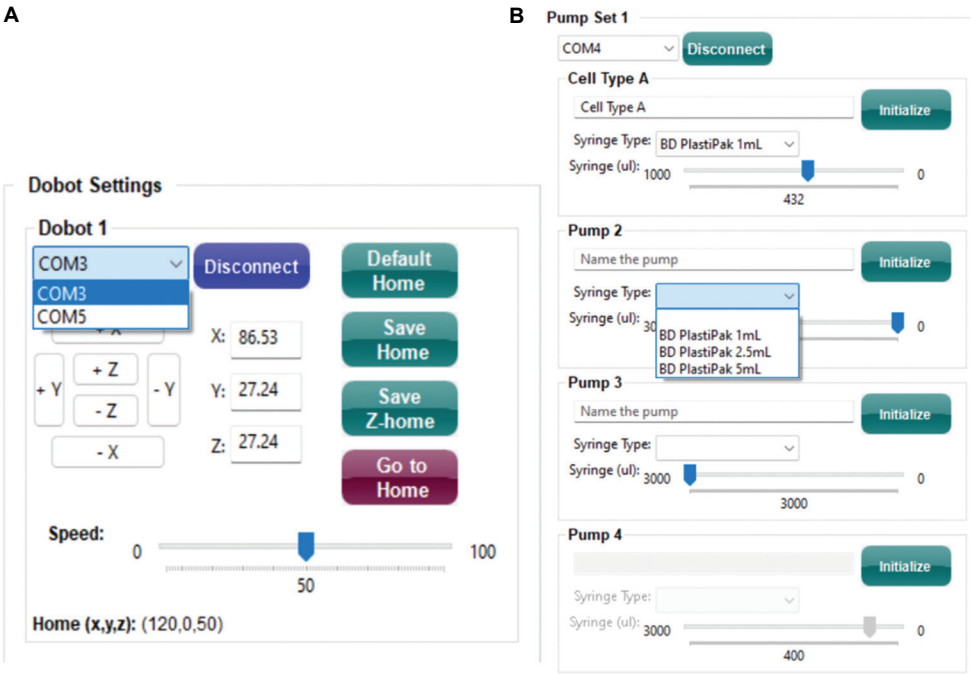

Figure 4. Zoomed-in images of the device settings tab. (A) Dobot settings; (B) pump settings.

for printing, referred to as the arm's local point. In a dual-arm setting where both arms are expected to print from the same point, the local points of the arms are expected to be the same point in 3D space, which creates a shared global point. This point is sent back to arms when starting the print. TwinPrint also offers flexibility in updating the

saved z-height separately without readjusting the XY home values. The arm travel speed can be adjusted using the axes buttons, but this does not affect the 3D bioprinting velocity previously specified in the parsed G-code.

Analogs to the arms, to determine which Pump settings box corresponds to its respective pump set, only one pump from each of the two sets can be initialized via the "Initialize" button. As shown in Figure 4B, Pump 1 is the master pump while Pumps 2–4 are arranged according to their position from the master. Since a total of eight pumps can be connected to the TwinPrint GUI, a labeling feature is incorporated for easy reference to each pump and its corresponding material type. This new name is then published across all tabs. Figure 4B shows the label of Pump 1 changed to "Cell Type A." In addition, TwinPrint supports the use of three gauge sizes for BD PlastiPak syringes (1, 3, and 5 mL), which are often needed in our 3D bioprinting experiments. For effortless monitoring of the volume of material dispensed from a pump, the GUI syringe slider values are updated according to the syringe gauge selected.

The "Pump Program Mode" tab, as shown in Figure 3B, is used to set an automated program for a pump, which creates a series of timed jobs to be run sequentially. The system supports three flow types (constant, ramp, and pulse) in three units (mL, µL, or nL). The buttons are to manage and facilitate the process of adding/deleting jobs. To keep track of the added/deleted jobs, a pump's programmed jobs are visualized on a flow rate (µL/min) versus time (min) graph. The added jobs are queued in the system, and this queue is passed to the pump when the "Program" button is clicked. If a job has a flow rate that exceeds the pump's accepted range of flow rates for the given syringe volume, the job will be rejected by the pump.

During the 3D bioprinting process, the "Job Settings" tab, as shown in Figure 3C, is used to load desired print files, adjust the z-height (during pauses), and specify the layer splitting parameter. The uploaded G-code filename is printed on the screen for user assurance. In addition, a G-code visualizer allows the user to preview the loaded 3D object and its individual 2D layers. More information on the development of the visualizer can be found in a previous publication.[10] The layers of a loaded 3D object are divided according to user inputs in the allocated fields. For example, if R1 layers are entered as "1" and R2 layers are entered as "2," a seven-layered 3D construct would be split alternately. In other words, R1 would print the odd-numbered layers, and R2 would print the even-numbered layers.

In the case that automated program mode is not selected for the pumps, manual control of each pump's flow rate is also achieved in the "Job Settings" tab. Noteworthy, a predictive machine learning model was developed as a software add-on to suggest optimal flow rates to the user for the 3D bioprinting materials selected. This is detailed in another study.[38] Moreover, to enhance user experience and ease the printing process involving several components, the side buttons offer device control both collectively and individually.

Finally, the "Printing Status monitoring" tab, as shown in Figure 3D, allows users to monitor the different printing and pumping activities occurring across all devices collectively in a single tab, making it easier to quickly discern any failure.

3.2. Print accuracy test

To validate the printing accuracy of the TwinPrint parsing process for the robotic arms, a 2D circle was drawn with pen ink and compared with standard Repetier printing software, TwinPrint single arm mode, and TwinPrint dual arm mode. To ensure fair comparison, the robotic arm speed was determined based on the feed rate (F value) specified in the G-code file. In our setup, the feed rate was set to 72 mm/min, and this value was kept constant across all three printing modes. Figure 5 shows the results along with the G-code preview. It was observed that the circles drawn by Repetier software and TwinPrint single mode were closely similar. Slight differences can be noticed in the line thickness, which is dependent on the set layer height due to the delicate nature of a pen's tip. In terms of printing accuracy, however, both were found to closely replicate the desired G-code preview and maintained equal spacing without elliptical variations, indicating that the shape was drawn as expected.

For TwinPrint's dual arm mode, two different colored

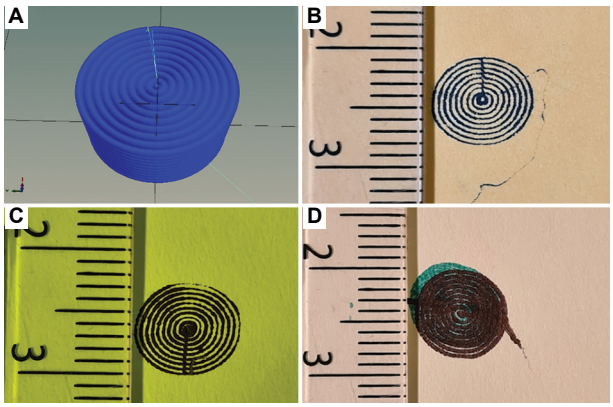

Figure 5. Printed circles with pens for accuracy evaluation. (A) A top view of a cylindrical construct from Repetier–Host Software; (B) A pen-printed circle using Repetier–Host software. (C) A circular shape printed using TwinPrint user interface in the single-arm mode. (D) Two color–printed circles in the dual-arm mode using TwinPrint System.

ballpoint pens were used to determine: (i) Parsing with respect to two arms, and (ii) setting of global points. While the parsing process was found to match the previous two modes, it was noted that there was a position inaccuracy when each arm would return to the set global position. Since the global point coordinates are received as feedback from the arm about its current location in the 3D space, it was noticed that when the arm was returned to the initial setpoint, it was slightly off from the specified point with a deviation <1 mm. This could be due to mechanical constraints of the arm. Several models of the Dobot® Magician were cross-tested, and similar results were found. However, it is worth noting that the line thickness of soft matter bioink is generally >1 mm, as compared to the 0.5 mm line thickness of a fine-tip ballpoint pen. Thus, it was deduced that the accuracy achieved was suitable for the 3D bioprinting requirements in our scope.

To validate layer allocation for each robot, several combinations of layer splitting were tested for objects of various layer heights. Some combinations required alternate layering, while others required sequential layering (where R1 prints X number of layers and R2 prints Y number of layers, one after the other). The tests were all found to pass successfully, with both robots able to print their allocated layers as specified by the user.

3.3. Pump accuracy test

A pump accuracy test was run with three pumps for a range of 4 flow rates (20, 50, 100, and 200 µL/min) to compare the accuracy of TwinPrint with its default SmartFlo® software and determine the error. Multiple pumps were used to minimize error readings from a single pump. Each pump was run for the range of selected flow rates, first by issuing a command from the SmartFlo® software, and second by TwinPrint. Each test was conducted thrice. Assuming the density of water is approximately 1, the mass of a weighing boat was recorded before and after collecting the desired volume of water for a period of 1 min. This roughly provided the mass of the accumulated volume of water in the boat. From this, an approximate comparison was deduced of each pump's performance when receiving a command from the two software programs. Figure 6 shows the results and the estimated error readings. Slight variances were noted between the two systems, but the difference was acceptable for the required application.

3.4. Acellular bioprinting and print resolution test

For a thorough demonstration of the TwinPrint system, an experiment was conducted to observe the synchronization of the arms while printing peptide-based 3D constructs. Shape fidelity and cell viability were assessed. An alternating

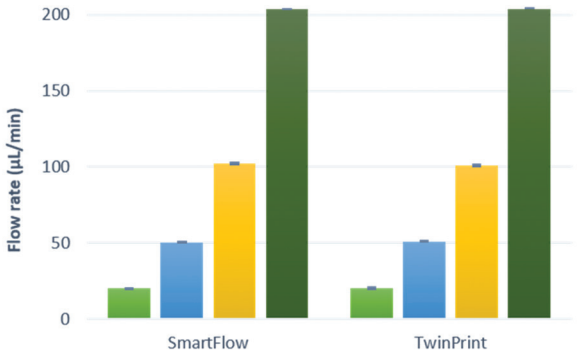

Figure 6. Estimated errors in flow rate by SmartFlo and TwinPrint software

layers approach was used to observe the interaction of both arms in processing commands sequentially, avoiding collision, and recalling start/stop positions.

Several trials were performed to resolve bugs in the code, which initially caused R2 to repeatedly "forget" its start position. Another issue faced was the timeout of the robots due to extended wait periods in between commands. This was resolved by adding a minimal movement command where R1 would move slightly while in wait position, as R2 completed its layer, and *vice versa*.

For system performance evaluation, the TwinPrint system was used for 3D bioprinting of an acellular 3D construct. A seven-layer cuboid of 10 × 10 × 1.4mm^3 was loaded and parsed by the software. Alternating layers were assigned to each robot by splitting them singularly. Pumps were set to 60 µL/min and 20 µL/min for IVZK peptide and 5× PBS, respectively, based on printing parameters optimized in previous reports.[23-25] R1 was manually moved to a desired start point with a z-height of 0.2 mm from the printbed, and the coordinates were saved using the GUI. The same was repeated for R2 at the same point. The system was prepared to print. A green dye was injected into S2 P6 (5× PBS) to facilitate observation of layers deposited by each arm.

Given the nature of soft matter ultrashort peptide-based bioinks, it was inevitable that accuracy would be reduced as compared to the pen test. However, printing resolution was assessed in terms of a standardized in-house printing rubric, which entails observing shape features, continuity of peptide gel, consistency of layer-buildup, and overall resolution compared to the desired G-code. Figure 7 shows a seven-layer cuboid (10 × 10 × 1.4 mm^3) printed with both arms depositing alternate layers of peptide-based bioink. R1 was set to extrude clear peptide ink while R2 was set to extrude green-stained peptide bioink, allowing differentiation between the two arms and simulating

a multi-material printing process (Video S1; video description is given in the "Supplemental information" section in this article).

During printing, layer allocation and start point accuracy were observed. R1 was expected to print the bottom layer and retreat to "home," avoiding collision with R2 as it printed the next layer. This process was repeated until layer 7. It was noted that R2 would shift slightly when returning to the desired start point in subsequent layers. This impacted the construct fidelity but was negligible for small constructs. It is presumed that the inaccuracy is due to mechanical constraints and the robot's cache memory. Overall, the resolution was good enough for the application, as bioinks are of low viscosity and tend to fill up gaps after deposition. Hence, the inaccuracy is less visible as compared to the pen ink test.

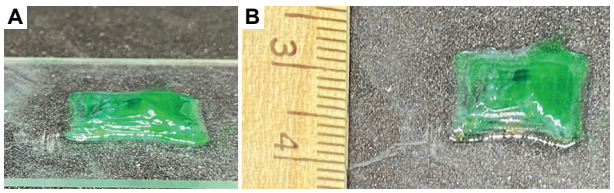

Figure 7. Acellular 3D construct of the peptide bioink IVZK with one bioink printing batch in green color (for one robotic arm) and another in clear color (for the second robotic arm) assembled in an alternating layer approach. (A) Side view; (B) top view.

3.5. Formation of 3D multi-cellular disease model

In the context of an intact organism, cells inhabit a complex 3D environment, wherein cell-cell interaction plays a pivotal role in tissue physiology and development.[39] Furthermore, the development of biomimicry disease models necessitates the precise replication of diverse cellular interactions, as this process is imperative in the formation of the diseased tissue microenvironment.[40,41] To test our system's potential for developing a multi-cellular disease model, we performed printing using two types of cells; AML cell line (HL60) and human BM-MSCs in a ratio of 3:1. Human BM-MSCs are well established as accessory cells that confer survival signals and chemoresistance advantage to acute leukemia cells.[42] Regarding bioink, we used IVZK peptide-based bioink.[19,20]

Our results demonstrated the potential of our dual-arm robotic system for the controlled deposition of

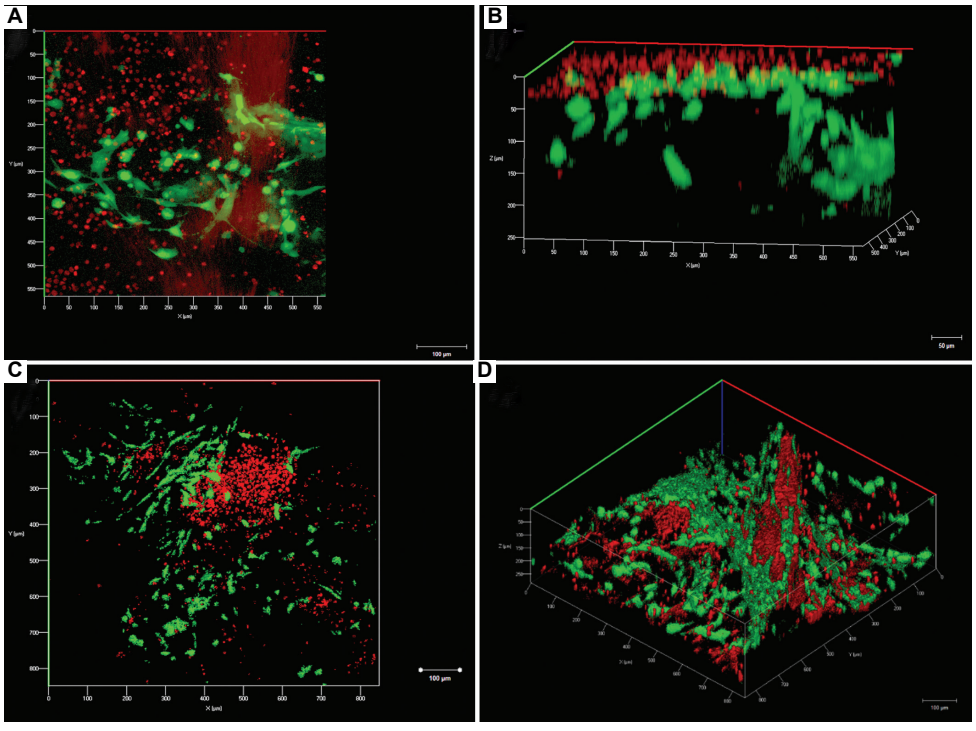

Figure 8. Formation of a multicellular 3D acute myeloid leukemia (AML) disease model through 3D bioprinting of AML cells (red, round) and human bone marrow mesenchymal stem (BM-MSCs) cells (green, fibroblast-like morphology) using the IVZK peptide-based bioink. (A) Front view of 3D constructed image; (B) Side view of a 3D constructed image showing the distribution of leukemia cells (red) and human BM-MSCs (green) on two different projection planes, as deposited by the dual-arm 3D bioprinter; (C) Front view of 3D constructed image; (D) Side view of a 3D constructed image. Cells were co-printed using a dual-arm 3D bioprinter at a ratio of 3:1 (leukemia cells: human BM-MSCs) and imaged in complete peptide hydrogel construct by means of confocal microscopy. Cells stained with CMFDA are shown in green, while cells stained with 5-chloromethyl tetraphenyl-p-xylylene (CMPTX) are shown in red.

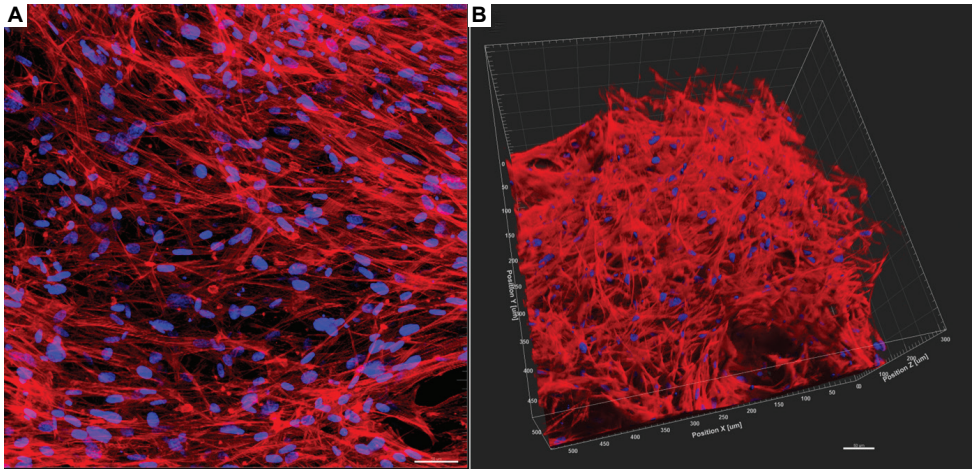

Figure 9. Cytoskeleton staining of human bone marrow mesenchymal stem after 30 days of bioprinting. (A) Front view of 3D rendered (constructed) image, demonstrating the distribution and matrix interaction between cells and peptide biomaterial; (B) Side view of the 3D constructed image covering a thickness of 500 µm in the direction of the Z axis, showing the distribution of cells within the IVZK peptide scaffold over a 500 µm length. Scale bar = 100 µm. Actin cytoskeleton is stained with phalloidin (red), and nuclei are stained with DAPI (blue).

different cell types while preserving cell viability and functionality. This is indicated by the retained fibroblast-like morphology of human BM-MSCs upon printing and the filopodia formation (Figure 8A and B). In addition, cell-cell interactions between BM-MSCs, and between BM-MSCs and leukemic cells, indicate cellular health status and the feasibility of our system for multi-cellular bioprinting (Figure 8C and D).

Moreover, at 30 days post-printing, the staining of the cytoskeleton of the BM-MSCs revealed the activity and the 3D distribution of cells within the printed constructs (Figure 9A and B). The cells maintained their fibroblast-like morphology with clearly defined actin fibers, demonstrating the binding between the cells and the peptide hydrogel. These findings further highlight the potential of our printing system.

4. Conclusion

The proposed research aimed to develop an upgraded, easy-to-use system, which is also efficient and resource-saving, to enable biofabrication of complex soft matter 3D constructs from a single software platform with a more automated approach. The TwinPrint system, developed in Python, was tested and evaluated for performance, printability, cell viability, and proliferation. It was found to considerably streamline the printing process, support multi-cellular and multi-material printing, and exhibit high compatibility with peptide-based bioinks. The synchronization of two robotic arms accelerates the printing process and enables several multi-tasking protocols. The results demonstrated that the TwinPrint system meets biofabrication needs by saving time, enhancing automation, and increasing freedom of motion. Further potential exists to standardize its use among researchers, develop software add-ons, and advance printing complexity. The success of TwinPrint underscores the importance of robots in 3D bioprinting for bridging the gap from research development to clinical applications.

Supplemental information

Description for Video S1. Demonstration of the dual-arm bioprinting process with different colored inks to simulate a multi-material print process. The TwinPrint system conducts an acellular print test using the peptide bioink IVZK, with one robotic arm printing green-colored bioink and the other robotic arm printing clear bioink in an alternating layer arrangement. This is done to simulate multi-material experiments and observe layer-by-layer deposition using different color dyes as well as assess print resolution of the fabricated construct.

Acknowledgments

The authors would like to thank Panayiotis Bilalis for support with the chemical synthesis of peptide compound IVZK, Eter Othman for initial support with text editing and Aris Konstantinidis for his technical insights.

Funding

This work was financially supported by King Abdullah University of Science and Technology under the base funding for Charlotte A. E. Hauser, under the KAUST-Smart Health Initiative project number: REI/1/4938. Additional funding was provided by Graz University of Technology (TU Graz).

Conflict of interest

Charlotte A. E. Hauser is an Editorial Board Member of this journal, but was not in any way involved in the editorial and peer-review process conducted for this paper, directly or indirectly. Separately, other authors declared that they have no known competing financial interests or personal relationships that could have influenced the work reported in this paper.

Author contributions

Conceptualization: Zainab N. Khan, Kowther Kahin
Investigation: Zainab N. Khan, Kowther Kahin, Noofa Hammad, Hibatallah Alwazani, Dana M. Alhattab
Methodology: Zainab N. Khan, Dana M. Alhattab
Project administration: Zainab N. Khan
Resources: Charlotte A. E. Hauser, Christian Baumgartner
Software: Noofa Hammad, Hibatallah Alwazani
Supervision: Charlotte A. E. Hauser
Validation: Zainab N. Khan, Noofa Hammad, Kowther Kahin, Hibatallah Alwazani, Dana M. Alhattab
Visualization: Noofa Hammad, Zainab N. Khan, Dana M. Alhattab
Writing–original draft: Noofa Hammad, Zainab N. Khan, Hibatallah Alwazani, Dana M. Alhattab, Charlotte A. E. Hauser
Writing–review & editing: Zainab N. Khan, Noofa Hammad, Dana M. Alhattab, Kowther Kahin, Christian Baumgartner, Charlotte A. E. Hauser

Ethics approval and consent to participate

Not applicable.

Consent for publication

Not applicable.

Availability of data

Data are available from the corresponding author upon reasonable request.

References

1. Pavek A, Nartker C, Saleh M, *et al*. Tissue engineering through 3D bioprinting to recreate and study bone disease. *Biomedicines*. 2021;9(5):551.

   doi: 10.3390/biomedicines9050551

2. Gao T, Gillispie GJ, Copus JS, *et al*. Optimization of gelatin-alginate composite bioink printability using rheological parameters: A systematic approach. *Biofabrication*. 2018;10(3):034106.

   doi: 10.1088/1758-5090/aacdc7

3. Xiongfa J, Hao Z, Liming Z, Jun X. Recent advances in 3D bioprinting for the regeneration of functional cartilage. *Regen Med*. 2018;13(1):73-87.

   doi: 10.2217/rme-2017-0106

4. Cubo N, Garcia M, Del Cañizo JF, Velasco D, Jorcano JL. 3D bioprinting of functional human skin: Production and *in vivo* analysis. *Biofabrication*. 2016;9(1):015006.

   doi: 10.1088/1758-5090/9/1/015006

5. Vijayavenkataraman S, Lu WF, Fuh JYH. 3D bioprinting of skin: A state-of-the-art review on modelling, materials, and processes. *Biofabrication*. 2016;8(3):032001.

   doi: 10.1088/1758-5090/8/3/032001

6. Izadifar M, Chapman D, Babyn P, Chen X, Kelly ME. UV-assisted 3D bioprinting of nanoreinforced hybrid cardiac patch for myocardial tissue engineering. *Tissue Eng Part C Methods*. 2018;24(2):74-88.

   doi: 10.1089/ten.tec.2017.0346

7. Hoch E, Tovar GEM, Borchers K. Bioprinting of artificial blood vessels: Current approaches towards a demanding goal. *Eur J Cardiothorac Surg*. 2014;46(5):767-778.

   doi: 10.1093/ejcts/ezu242

8. Wang X, Ao Q, Tian X, *et al*. 3D bioprinting technologies for hard tissue and organ engineering. *Materials (Basel)*. 2016;9(10):802.

   doi: 10.3390/ma9100802

9. Richard C, Neild A, Cadarso VJ. The emerging role of microfluidics in multi-material 3D bioprinting. *Lab Chip*. 2020;20(12):2044-2056.

   doi: 10.1039/c9lc01184f

10. AlZaid S, Hammad N, Albalawi HI, Khan ZN, Othman E, Hauser CAE. Advanced software development of 2D and 3D model visualization for twinprint, a dual-arm 3D bioprinting system for multi-material printing. *Mater Sci Add Manuf*. 2022;1(3):19.

    doi: 10.18063/msam.v1i3.19

11. Sodupe-Ortega E, Sanz-Garcia A, Pernia-Espinoza A, Escobedo-Lucea C. Accurate calibration in multi-material 3D bioprinting for tissue engineering. *Materials (Basel)*. 2018;11(8):1402.

    doi: 10.3390/ma11081402

12. Maresca JA, DeMel DC, Wagner GA, Haase C, Geibel JP. Three-dimensional bioprinting applications for bone tissue engineering. *Cells*. 2023;12(9):1230.

    doi: 10.3390/cells12091230

13. Cameron T, Naseri E, MacCallum B, Ahmadi A. Development of a disposable single-nozzle printhead for 3D bioprinting of continuous multi-material constructs. *Micromachines (Basel)*. 2020;11(5):459.

    doi: 10.3390/mi11050459

14. Liu W, Zhang YS, Heinrich MA, *et al*. Rapid continuous multimaterial extrusion bioprinting. *Adv Mater*. 2017;29(3):1604630.

doi: 10.1002/adma.201604630

15. Miri AK, Nieto D, Iglesias L, *et al*. Bioprinting: Microfluidics-enabled multimaterial maskless stereolithographic bioprinting (Adv. Mater. 27/2018). *Adv Mater*. 2018;30(27):1870201.

doi: 10.1002/adma.201870201

16. Pagan E, Stefanek E, Seyfoori A, *et al*. A handheld bioprinter for multi-material printing of complex constructs. *Biofabrication*. 2023;15(3):035012.

doi: 10.1088/1758-5090/acc42c

17. Hauser CAE, Deng R, Mishra A, *et al*. Natural tri- to hexapeptides self-assemble in water to amyloid beta-type fiber aggregates by unexpected alpha -helical intermediate structures. *Proc Natl Acad Sci U S A*. 2011;108(4):1361-1366.

doi: 10.1073/pnas.1014796108

18. Mishra A, Loo Y, Deng R, *et al*. Ultrasmall natural peptides self-assemble to strong temperature-resistant helical fibers in scaffolds suitable for tissue engineering. *Nano Today*. 2011;6(3):232-239.

doi: 10.1016/j.nantod.2011.05.001

19. Rauf S, Susapto HH, Kahin K, *et al*. Self-assembling tetrameric peptides allow *in situ* 3D bioprinting under physiological conditions. *J Mater Chem B*. 2021;9(4):1069-1081.

doi: 10.1039/d0tb02424d

20. Susapto HH, Alhattab D, Abdelrahman S, *et al*. Ultrashort peptide bioinks support automated printing of large-scale constructs assuring long-term survival of printed tissue constructs. *Nano Lett*. 2021;21(7):2719-2729.

doi: 10.1021/acs.nanolett.0c04426

21. Ravanbakhsh H, Karamzadeh V, Bao G, Mongeau L, Juncker D, Zhang YS. Emerging technologies in multi-material bioprinting. *Adv Mater*. 2021;33(49):2104730.

doi: 10.1002/adma.202104730

22. Loo Y, Lakshmanan A, Ni M, Toh LL, Wang S, Hauser CAE. Peptide bioink: Self-assembling nanofibrous scaffolds for three-dimensional organotypic cultures. *Nano Lett*. 2015;15(10):6919-6925.

doi: 10.1021/acs.nanolett.5b02859

23. Kahin K, Khan Z, Albagami M, *et al*. Development of a robotic 3D bioprinting and microfluidic pumping system for tissue and organ engineering. In: Gray BL, Becker H, editors. *Microfluidics, BioMEMS, and Medical Microsystems XVII*. Washington, DC: SPIE; 2019. p. 25.

doi: 10.1117/12.2507237

24. Khan Z, Kahin K, Rauf S, *et al*. Optimization of a 3D bioprinting process using ultrashort peptide bioinks. *Int J Bioprint*. 2018;5(1):173.

doi: 10.18063/ijb.v5i1.173

25. Khan Z, Kahin K, Hauser C. Time-dependent pulsing of microfluidic pumps to enhance 3D bioprinting of peptide bioinks. In: Gray BL, Becker H, editors. *Microfluidics, BioMEMS, and Medical Microsystems XIX*. Washington, DC: SPIE; 2021. p. 5.

doi: 10.1117/12.2578830

26. Li K, Huang W, Guo H, *et al*. Advancements in robotic arm-based 3D bioprinting for biomedical applications. *Life Med*. 2023;2(6):lnad046.

doi: 10.1093/lifemedi/lnad046

27. Xie N, Shi G, Shen Y, *et al*. Research progress of robot technology in *in situ* 3D bioprinting. *Int J Bioprint*. 2022;8(4):614.

doi: 10.18063/ijb.v8i4.614

28. Prendergast ME, Burdick JA. Recent advances in enabling technologies in 3D printing for precision medicine. *Adv Mater*. 2020;32(13):1902516.

doi: 10.1002/adma.201902516

29. Dong H, Hu B, Zhang W, *et al*. Robotic-assisted automated *in situ* bioprinting. *Int J Bioprint*. 2022;9(1):629.

doi: 10.18063/ijb.v9i1.629

30. Albert BJ, Wang C, Williams C, Butcher JT. Non-planar embedded 3D printing for complex hydrogel manufacturing. *Bioprinting*. 2022;28:e00242.

doi: 10.1016/j.bprint.2022.e00242

31. Wulle F, Gorke O, Schmidt S, *et al*. Multi-axis 3D printing of gelatin methacryloyl hydrogels on a non-planar surface obtained from magnetic resonance imaging. *Addit Manuf*. 2022;50:102566.

doi: 10.1016/j.addma.2021.102566

32. Fortunato GM, Batoni E, Bonatti AF, Vozzi G, De Maria C. Surface reconstruction and tissue recognition for robotic-based *in situ* bioprinting. *Bioprinting*. 2022;26:e00195.

doi: 10.1016/j.bprint.2022.e00195

33. Ozbolat IT, Moncal KK, Gudapati H. Evaluation of bioprinter technologies. *Addit Manuf*. 2017;13:179-200.

doi: 10.1016/j.addma.2016.10.003

34. Ozbolat IT, Hospodiuk M. Current advances and future perspectives in extrusion-based bioprinting. *Biomaterials*. 2016;76:321-343.

doi: 10.1016/j.biomaterials.2015.10.076

35. Wong KV, Hernandez A. A review of additive manufacturing. *ISRN Mech Eng*. 2012;2012:208760.

doi: 10.5402/2012/208760

36. Montalti A, Ferretti P, Santi GM. From CAD to G-code: Strategies to minimizing errors in 3D printing process. *CIRP J Manuf Sci Technol*. 2024;55:62-70.

doi: 10.1016/j.cirpj.2024.09.005

37. Bikas H, Stavropoulos P, Chryssolouris G. Additive manufacturing methods and modelling approaches: A critical review. *Int J Adv Manuf Technol*. 2016;83(1-4):389-405.

doi: 10.1007/s00170-015-7576-2

38. Hammad NS, Khan ZN, Valle-Pérez AU, Hauser C. A predictive machine learning model to optimize flow rates on an integrated microfluidic pumping system for peptide-based 3D bioprinting. In: Gray BL, Rapp BE, editors. *Microfluidics, BioMEMS, and Medical Microsystems XXI*. Washington, DC: SPIE; 2023. p. 3.

doi: 10.1117/12.2650440

39. Lv D, Hu Z, Lu L, Lu H, Xu X. Three-dimensional cell culture: A powerful tool in tumor research and drug discovery. *Oncol Lett*. 2017;14(6):6999-7010.

doi: 10.3892/ol.2017.7134

40. Heinrich MA, Bansal R, Lammers T, Zhang YS, Michel Schiffelers R, Prakash J. 3D-bioprinted mini-brain: A glioblastoma model to study cellular interactions and therapeutics. *Adv Mater*. 2019;31(14):e1806590.

doi: 10.1002/adma.201806590

41. Kokkaliaris KD, Scadden DT. Cell interactions in the bone marrow microenvironment affecting myeloid malignancies. *Blood Adv*. 2020;4(15):3795-3803.

doi: 10.1182/bloodadvances.2020002127

42. Ladikou EE, Sivaloganathan H, Pepper A, Chevassut T. Acute myeloid leukaemia in its niche: The bone marrow microenvironment in acute myeloid leukaemia. *Curr Oncol Rep*. 2020;22(3):27.

doi: 10.1007/s11912-020-0885-0

ACCSCIENCE PUBLISHING

OUR JOURNALS

Materials Science in Additive Manufacturing (MSAM) aims to bridge the cutting-edge research between additive manufacturing and the entire spectrum of materials science. The journal covers all applied and fundamentals of processing, synthesis, structure, composition, properties and performance of materials designed or manipulated for additive manufacturing. The journal covers a wide scope of innovative techniques, processes, methods, and applications. Topics of particular interest include, but are not limited to:

- Theory and modelling
- Artificial intelligence
- Polymers
- Metals and alloys
- Ceramics
- Composites
- Magnetic materials
- Smart materials
- Nano-materials
- Materials for electronics
- Characterization techniques

International Journal of AI for Materials and Design is an international, peer-reviewed open-access journal that aims to bridge the cutting-edge research between AI and materials, AI and design. In recent years, the tremendous progress in AI is leading a radical shift of AI research from a mainly academic endeavor to a much broader field with increasing industrial and governmental investments. The maturation of AI technology brings about a step change in the scientific research of various domains, especially in the world of materials and design. Machine learning (ML) algorithms enable researchers to analyze extensive datasets on material properties and accurately predict their behavior in different conditions. This subsequently impact the industry to leverage on big data and advanced analytics to build scientific strategies, scale operational performance of processes and drive innovation.

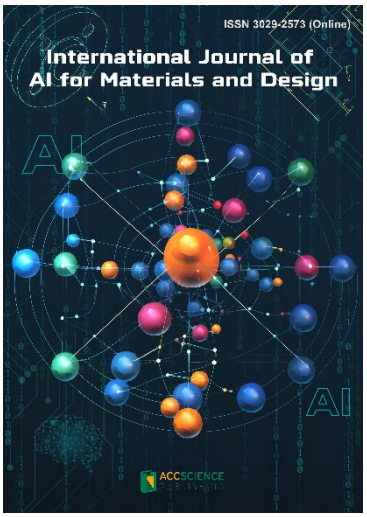

International Journal of AI for Materials and Design covers the following topics: AI or machine learning for material discovery, AI for process optimization, AI and data-driven approaches for product or systems design, application of AI in advanced manufacturing processes such as additive manufacturing, IoT, sensors, robotics, cloud-based manufacturing, intelligent manufacturing for various applications, autonomous experiments, material intelligence, energy intelligence, and AI-linked decarbonization technologies.

Start a new journal

Write to us via email if you are interested to start a new journal with AccScience Publishing. Please attach your CV, professional profile page and a brief pitch proposal in your email. We shall inform you of our decision whether we are interested to collaborate in starting a new journal.

Contact: info@accscience.com

https://accscience.com/journal/ESAM

Contact
www.accscience.com
9 Raffles Place, Republic Plaza 1 #06-00 Singapore 048619
Email: editorial@accscience.com
Phone: +65 8182 1586